UNIVERSITY OF CALIFORNIA

RIVERSIDE

Search for WZ Production in the Tri-lepton Channel at the Tevatron and Limits on the WWZ Vertex Anomalous Couplings

A Dissertation submitted in partial satisfaction

of the requirements for the degree of

Doctor of Philosophy

in

Physics

by

Patrick Elmo Gartung

December, 1998

Dissertation Committee:

Dr. John Ellison, Chairperson

Dr. Benjamin Shen

Dr. Stephen Wimpenny

The Dissertation of Patrick Elmo Gartung is approved:

Committee Chairperson

University of California, Riverside

Acknowledgements

It is traditional at this point to acknowledge those who have helped in the process of obtaining a Ph.D. There are a great many people who have helped me over the years and if I have left anyone out my sincerest apologies.

Firstly I would like to thank the DØ collaboration. I came in late on the experiment after the detector had been built and the software written. If it were not for the effort of hundreds of physicists over many years I would not have had any data to perform my analysis on. I would also like to thank the Fermilab Accelerator and Computing Divisions whose help was essential in performing the experiment.

I would like to thank my advisor John Ellison for introducing me to the world of particle physics and giving me an interesting problem to research. Without his support and lots and lots of patience I would never have finished.

I would like to thank the members of the U.C. Riverside DØ group who have helped me: Jim Cochran, Chris Boswell, Krish Gounder, Steve Wimpenny and Ann Heinson. Yvonne Ayers deserves a mention for her help in taking care of the administrative details for the group.

I would like to thank the people at Fermilab who have helped me. Tom Diehl, Taka Yasuda, Greg Landsberg, Steve Glenn, Paul Bloom and other members of the

diboson research group helped me understand the business of diboson physics and limit setting. Dave Buchholz and the members of Editorial Board 110 were crucial in "fact checking" my final numbers. Paul Russo, Scott Snyder and Paul Rubinov were there for me when I needed someone to talk to.

I would like to thank my friends who made life in graduate school more bearable: fellow Riverside students Martin Mason, Happy Singh, Christian Minor and Mike Crivello, and the Friday night crew Jim, Eric, Hayley and Caryn.

I would like to thank my parents for their support and encouragement in pursuing my education.

Last but not least, I owe a deep debt of gratitude to my wife Julie. Her love and encouragement were essential in the completion of my research.

To

Julie and Baby M

And

My Parents

Abstract of Dissertation

Search for WZ Production in the Tri-lepton Channel at the Tevatron and Limits on the WWZ Vertex Anomalous Couplings

by

Patrick Elmo Gartung

Doctor of Philosophy, Graduate Program in Physics

University of California, Riverside, December, 1998

Professor John Ellison, Chairperson

A search for WZ production through the study of the reaction $p\bar{p} \to l\bar{\nu}ee + X$ ($l = e, \mu$) at $\sqrt{s} = 1.8$ TeV using the DØ detector at Fermilab is presented. In a data sample corresponding to an integrated luminosity of 92.3 ± 5.0 pb^{-1}, 1 candidate event was identified. The Standard Model prediction is 0.245 ± 0.002 (stat) $\pm$ 0.015 (syst) events, with an estimated background of 0.498 ± 0.072 (stat) ± 0.125 (syst) events. The 95% confidence level limit on the WZ production cross section is 48.3 pb. Limits on the WWZ anomalous coupling paramters are obtained from a likelihood fit to the number of observed events. Assuming a form factor scale of 1.0 TeV, the 95% confidence level limits on the WWZ couplings are $|\lambda_Z| < 1.42$ and $|\Delta g_Z^1| < 1.63$ when the other coupling parameters are constrained to their Standard Model values.

Contents

List of Tables

List of Figures

Chapter 1

The Standard Model and the Physics of WZ Production

1.1 The Standard Model and Particle Physics

Over the last 100 years the field of particle physics has developed through the efforts of experimentalists and theorists. The goal of particle physics is to develop and test models of the fundamental constituents of matter and the forces that act between them. One such model has emerged which has been very successful at explaining experimental data and making predictions for the existence of new particles. This model has been dubbed the "Standard Model" of particle physics because of this success.

In the Standard Model, all matter is made up of point-like particles called

quarks and leptons. For each particle there is an anti-particle with the same mass but opposite electric charge. The forces between particles are mediated by the exchange of bosons. Three of the four fundamental forces of nature are described by the model: electromagnetism, the "weak" force and the "strong" force. The fourth force, gravity, is many orders of magnitude weaker than the others at the distance and energy scales available in the laboratory and can be safely ignored.

Leptons include the familiar electron and its heavier, unstable analogs the muon and tau, all of which carry charge -1. For each lepton there exists a corresponding neutral particle called a neutrino which has negligible or zero mass.

There are six types of quarks: "up", "down", "strange", "charm", "bottom" and "top"[1]. Quarks have the curious property of having fractional electric charge, $+2/3$ for up, strange and top, and $-1/3$ for down, charm, and bottom. Quarks only exists in pairs or triplets, giving the composite particles a ± 1 or 0 electric charge. Quarks also carry color charge, which is associated with the strong force. This is analogous to the association of the electric charge with the electromagnetic force.

Quarks are the constituents of hadrons. Hadrons include the familiar proton and neutron and other heavier, unstable particles such as the pion. The proton is composed of two up quarks and a down quark which are bound together by the strong force. Through the process of hadronization, a bare quark will bind with other quarks to form a hadron. A quark would therefore appear as a "jet" of hadrons.

[1] Conclusive evidence of the existence of the top quark was only recently discovered [1, 2].

Leptons and quarks are collectively called fermions. They are so named because they carry odd half-integer intrinsic angular momentum (spin) and obey the Pauli exclusion principle of Fermi-Dirac statistics.

Gauge bosons are spin-1 particles which are the carriers of the electromagnetic, weak and strong forces. They mediate the interactions between quarks and leptons. The massless photon carries the electromagnetic force over infinite distances. The gluons transmit the strong force over a range of order 1 fm, and the massive $W^{\pm}$ and Z bosons transmit the weak force over much shorter distances.

In the Standard Model the electromagnetic and weak interactions are unified into the electroweak force. The focus of this thesis is a test of the predictions of the electroweak interaction. The electroweak sector of the Standard Model is discussed in the next section as a basis for further discussion.

1.2 Electroweak Interactions

The $SU(2)_L \times U(1)_Y$ symmetry group is the basis of the Standard Model of electroweak interactions [3, 4]. In constructing the theory, four gauge fields are introduced: $W_\mu^i \quad (i = 1, 2, 3)$ for $SU(2)_L$ and B_μ for $U(1)_Y$. The fermions are written as left- and right-handed fields, which interact with these gauge fields. The

left-handed fermion fields are written as isospin doublets

$$\begin{pmatrix} \nu_L \\ l_L \end{pmatrix}$$

which transform under the $j = 1/2$ representation of $SU(2)$. The right-handed fields are isospin singlets, l_R, which transform under the $j = 0$ (trivial) representation of $SU(2)$.

The non-Abelian $SU(2)$ group is associated with weak-isospin (I). The Abelian group $U(1)_Y$ is associated with the weak hypercharge, Y. The weak hypercharge is related to the electric charge (Q) and the weak-isospin by the Gell-Mann-Nishijima relation: $Q = I_3 + Y/2$ (I_3 is the 3-projection of I).

To give the gauge bosons mass, an isospin doublet of complex scalar Higgs fields ϕ is introduced, with a potential function which results in a non-zero vacuum expectation value for ϕ. This results in the spontaneous breaking of the local $SU(2)$ gauge symmetry generating masses for the gauge bosons. Of the four fields only one corresponds to a physical particle, the Higgs boson [5]. The mass of the Higgs boson is a free parameter that has not been experimentally measured to date. Indeed, searching for the Higgs boson and experimental elucidation of the mechanism of electroweak symmetry breaking is one of the main goals in particle physics.

The electroweak bosons are combinations the the W and B fields. Linear combinations of the W_1 and W_2 fields are identified as the $W^{\pm}$ fields, and linear combinations of the W_3 and B fields is identified as the Z field and the photon

field, A.

A direct consequence of the Standard Model is the occurrence of gauge boson self-couplings. This arises due to the non-Abelian character of the $SU(2)$ group. There are two types of interactions, the trilinear gauge couplings ($WW\gamma$, WWZ) and the quadralinear gauge couplings ($WWWW$, $WWZZ$, $WWZ\gamma$, $WW\gamma\gamma$) as illustrated in Figures 1.1–1.2.

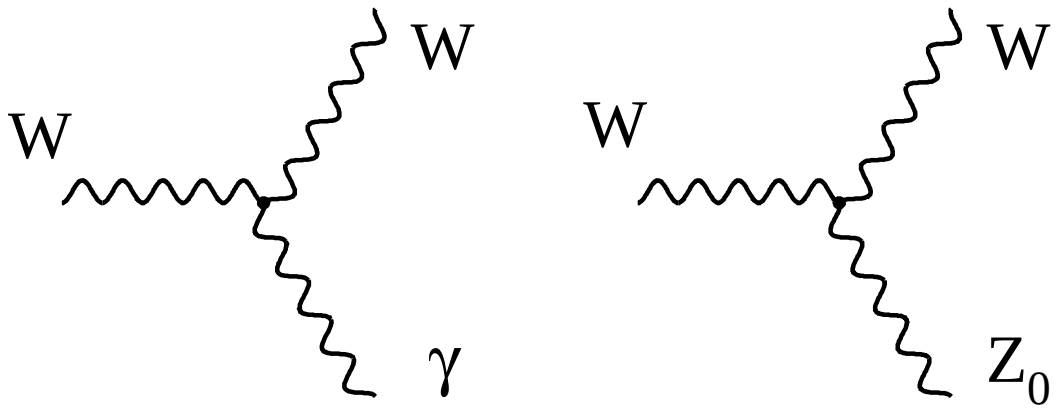

Figure 1.1: Feynman diagrams of the trilinear gauge boson couplings allowed by the Standard Model.

1.3 WZ Production in the Standard Model

At the focus of this study are the interactions between the gauge bosons, the most accessible of which are the trilinear gauge couplings. The Lagrangian $\mathcal{L}$

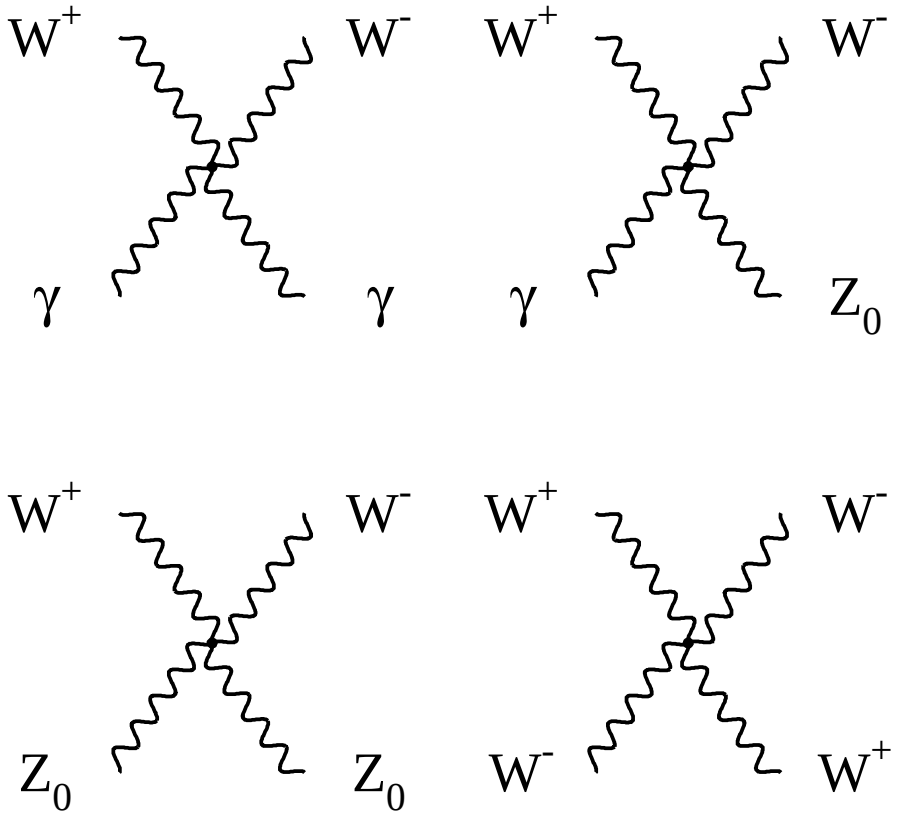

Figure 1.2: Feynman diagrams of the quadralinear gauge boson couplings allowed by the Standard Model.

describing this portion of the electroweak sector is given by

$$\begin{aligned}\mathcal{L} &= -ie(W_\mu^- W_\nu^+ A^{\mu\nu} + W_\mu^+ W^{-\mu\nu} A_\nu - W^{+\mu\nu} W_\mu^- A_\nu) \\ &\quad -ie\cot\theta_W (W_\mu^- W_\nu^+ Z^{\mu\nu} + W_\mu^+ W^{-\mu\nu} Z_\nu - W^{+\mu\nu} W_\mu^- Z_\nu). \qquad (1.1)\end{aligned}$$

where θ_W is the weak mixing angle, $W^{\pm\mu}$ is the $W^{\pm}$ field, Z^{μ} is the Z field, and A^{μ} is the photon field. These terms, which specify the $WW\gamma$ and WWZ vertices respectively, arise due to the non-Abelian gauge structure of the electroweak theory. When combined with the terms describing the fermion couplings to the bosons, these terms completely describe WZ production at tree level in the Standard Model.

1.3.1 WZ Production Mechanisms

There are three Feynman diagrams which describe tree level WZ production at a hadron collider in the Standard Model, as shown in Figure 1.3. The first two diagrams represent t- and u-channel WZ production and are fully described by the couplings of the fermions to the W and Z bosons. These couplings have been measured with high precision in the production of single W and Z bosons [6, 7]. The third diagram shows s-channel WZ production which involves the coupling of the W and Z bosons, *i.e.* the WWZ coupling. Therefore an experimental study of WZ production enables the measurement of the WWZ coupling.

1.3.2 Standard Model Predictions for WZ Production

Once the tree level Feynman diagrams for WZ production are known, it is possible to predict observables such as the cross section. The calculation of the WZ production cross section leads to an insight into the structure of the Standard Model. If only the t- and u-channel diagrams were used to calculate the total cross

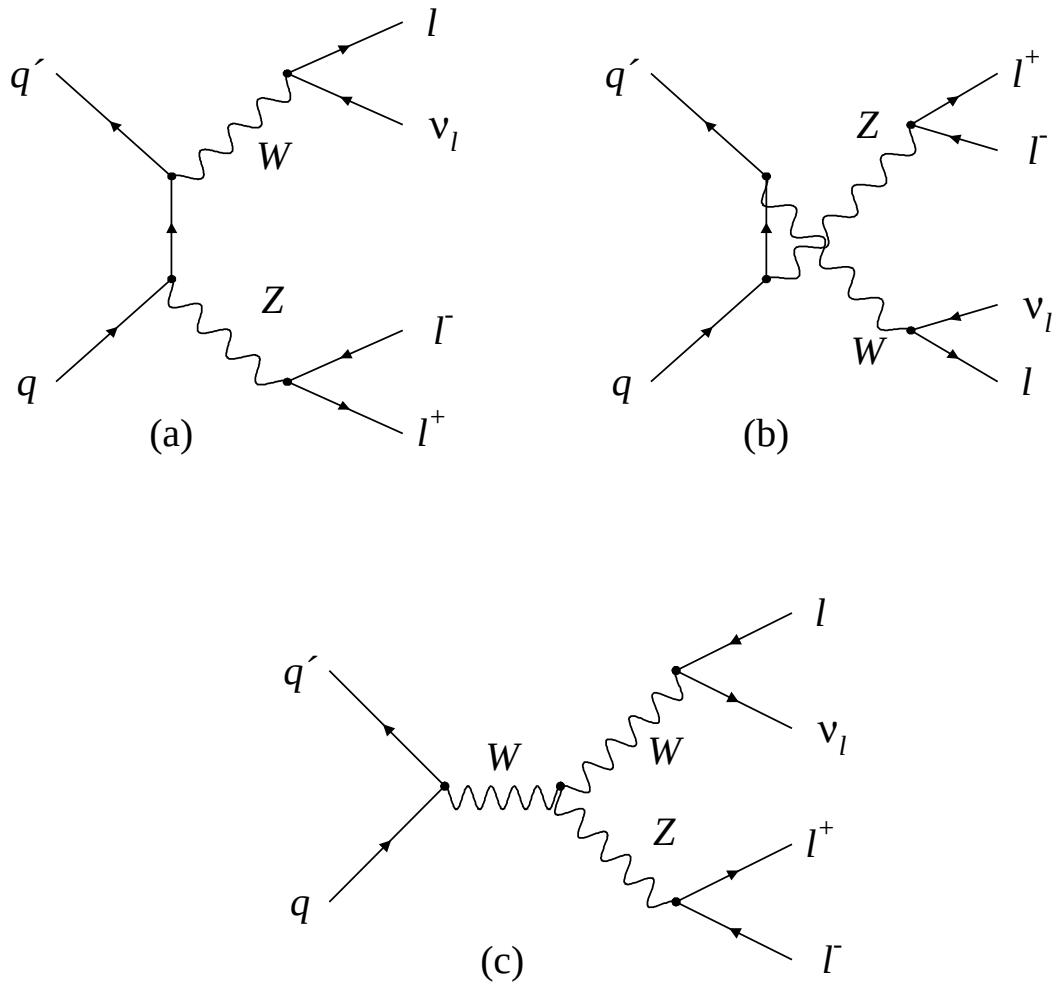

Figure 1.3: Standard Model Feynman Diagrams for tree level WZ production with subsequent decay into leptons: (a) t-channel; (b) u-channel; (c) s-channel.

section, the result would be a linear rise of the cross section with increasing $\sqrt{\hat{s}}$ (the parton center of mass energy). This implies that for sufficiently large energies partial wave unitarity will be violated, i.e. the sum of the probabilities of the partial waves

will be greater than one. By including the s-channel diagram, which involves the boson-boson couplings, the cross terms which result from squaring all the summed amplitudes provide the "delicate" gauge cancellations which are required to restore unitarity. By construction, the Standard Model provides the gauge boson self-interaction terms which restore the physical consistency of the model, although these terms are unnecessary to describe many weak current interactions, such as β decay. As will be shown later, this cancellation will have important consequences in the search for deviations from the Standard Model-predicted values for the boson-boson couplings.

A numerical result for the WZ production cross section cannot be produced analytically because of the composite nature of the proton and antiproton. The parton subprocess cross section can be computed analytically, but this must be summed over all possible pairs of participating partons in the proton and anti-proton, and additionally integrated over the parton momentum distributions. A Monte Carlo approach can be used to solve this problem. Event generators such as PYTHIA [8] can be used to fully model Standard Model WZ production and can be used to produce a numerical result for the cross section. Another Monte Carlo provided by the authors of reference [9] uses a fast Monte Carlo approach to model WZ production. Using the MRSD$-'$ parton distribution function set [10], the fast Monte Carlo predicts a Standard Model cross section of 2.6 pb after multiplying the tree level cross section by a "k-factor" to account for initial and final state radiation.

Monte Carlo programs can also be used to model the kinematic characteristics of WZ events.

1.3.3 Experimental Signature of WZ production

WZ production can occur in three distinct channels: those in which both bosons decay hadronically, those in which one decays hadronically and the other leptonically, and those in which both decay leptonically.

The purely hadronic final state has one advantage. It has as a significantly larger branching fraction than all leptonic decays. However the disadvantages far outweigh this advantage. First, it is nearly impossible to reconstruct which hadronic jet came from which boson. This is due to the finite energy resolution of hadronic calorimeters and to the difficulty of the charge sign determination of jets. Further, the limited energy resolution of hadronic calorimeters makes distinguishing W's from Z's difficult at best. WW and WZ production are therefore indistinguishable in this channel. Finally this channel suffers from a large background due to continuum multijet production as well as the production of single W or Z bosons in association with jets.

The semi-leptonic decay modes have the next largest branching fractions, 15% for the $l\nu jj$ final state and 4.5% for the $lljj$ final state, where l is an electron or muon and j is a hadron jet. This channel suffers from large QCD backgrounds from both multijet production and W production in association with jets, which is

indistinguishable from Standard Model WZ production. As in the fully hadronic channel, it is impossible to distinguish WZ production from WW production in the $l\nu jj$ channel. The $lljj$ final state has the advantage of being identified only with WZ production. However, this final state is dominated by backgrounds from Z production in association with jets. The main advantages of this channel are the relatively large branching fraction and the ability to unambiguously reconstruct the momentum of each boson. A cross section measurement in the semi-leptonic channel is insensitive due the inability to distinguish signal from background.

The purely leptonic final state has the smallest branching fraction of all, 1.5% when both electrons and muons are counted (tau's are excluded due to the difficulty in identifying them efficiently). The one drawback of this channel is the relatively small branching fraction. The main advantage of this channel is its unique signature, three charged leptons with high transverse momentum (p_T), and large missing transverse energy ($\not\!\!E_T$). This signature is unique amongst diboson final states and virtually background free. No physics processes produce a significant background. The only backgrounds are instrumental backgrounds, which arise from the misidentification of a jet as a lepton.

As a result of these factors, WZ production in the purely leptonic decay mode provides a sensitive measure of the cross section and a direct measure of the WWZ vertex. The search for WZ production in the purely leptonic final state is the subject of this thesis.

1.4 WZ Production Beyond the Standard Model

Despite its agreement with all observations to date, it is widely believed that the Standard Model represents only the low-energy limit of a more fundamental theory. There are features of the theory which remain unsatisfactory. The required fine tuning of quadratic divergences, the "mass hierarchy" issue [11], and the ansatz nature of the Higgs field motivate the search for a more comprehensive theory. At the energies accessible at today's experiments, deficiencies in the Standard Model may only become evident through precision measurements. Deviations in the WWZ coupling due to non-Standard Model physics will have an effect on WZ production. In this section, the possible mechanisms for non-Standard Model WZ production are discussed. Following this, a generalized formalism is introduced to cope with all such scenarios without regard to the details of the particular underlying theory. Finally, the experimental signature of "anomalous" WZ production is discussed.

1.4.1 Mechanisms for non-Standard Model WZ Production

Many scenarios for physics beyond the Standard Model, which give rise to non-Standard Model diboson production, have been considered [12, 13, 14, 15, 16, 17, 18, 19, 20, 21, 22]. Most deviations from the Standard Model involve radiative loop corrections to the trilinear gauge boson vertices. These deviations have been studied extensively for the $WW\gamma$ coupling. Loop corrections involving Standard

Model and Supersymmetric particles produce deviations in $\Delta\kappa_\gamma$ on the order of 10^{-3} [23]. Other models produce smaller deviations.

1.4.2 Formalism

With the supposition that there are non-Standard Model mechanisms which could modify the WWZ vertex, it is desirable to express these new interactions in a model independent manner. The approach used is to introduce a set of parameters which describe the most general form of the gauge boson vertices. The s-channel diagram in Figure 1.3c is replaced by a generalized coupling between the Z and the W as symbolized in Figure 1.4. An effective Lagrangian technique is used to describe the WWZ coupling and to define a set of coupling parameters.

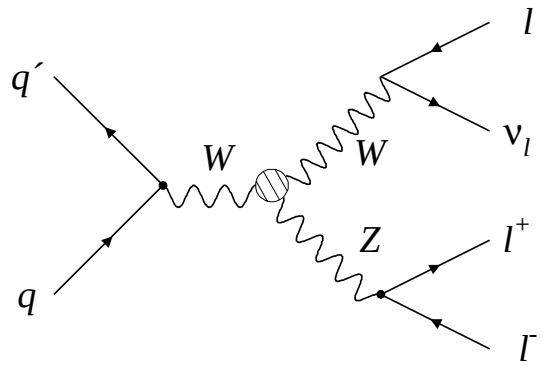

Figure 1.4: Feynman Diagrams for tree level non-Standard Model WZ production with subsequent decay into leptons.

The most general effective Lagrangian that can be written for the WWZ vertex is [24]

$$\begin{aligned}
\mathcal{L}_{WWZ}/g_{WWZ} &= ig_1^Z(W_{\mu\nu}^\dagger W^\mu Z^\nu - W_\mu^\dagger Z_\nu W^{\mu\nu}) \\
&+i\kappa_Z W_\mu^\dagger W_\nu Z^{\mu\nu} \\
&+\frac{i\lambda_Z}{M_W^2} W_{\rho\mu}^\dagger W_\nu^\mu Z^{\nu\rho} \\
&-g_4^Z W_\mu^\dagger W_\nu(\partial^\mu Z^\nu + \partial^\nu Z^\mu) \\
&+g_5^Z \epsilon^{\mu\nu\rho\sigma}(W_\mu^\dagger \partial_\rho W_\nu - W_\nu \partial_\rho W_\mu^\dagger) Z_\sigma \\
&+\tilde{\kappa}_Z W_\mu^\dagger W_\nu \tilde{Z}^{\mu\nu} \\
&+\frac{i\tilde{\lambda}_Z}{M_W^2} W_{\rho\mu}^\dagger W_\nu^\mu \tilde{Z}^{\nu\rho}
\end{aligned}$$

where $W_{\mu\nu} \equiv \partial_\mu W_\nu - \partial_\nu W_\mu$, $Z_{\mu\nu} \equiv \partial_\mu Z_\nu - \partial_\nu Z_\mu$ and $\tilde{Z}^{\mu\nu} \equiv \frac{1}{2}\epsilon_{\mu\nu\rho\sigma} Z^{\rho\sigma}$. The overall coupling is defined to be $g_{WWZ} \equiv -e\cot\theta_W$ where θ_W is the weak mixing angle and e the electron charge. In the Standard Model the couplings at tree level (before loop corrections) are $g_1^Z = \kappa_Z = 1$ and $\lambda_Z = g_4^Z = g_5^Z = \tilde{\kappa}_Z = \tilde{\lambda}_Z = 0$. These 7 general coupling parameters allow for C or P violation (g_5^Z) and CP violation (g_4^Z, $\tilde{\kappa}_Z$, $\tilde{\lambda}_Z$). In this and most studies these terms are neglected, leaving 3 couplings (g_1^Z,κ_Z,λ_Z) to be measured. Deviations from the Standard Model are given by the following coupling parameters:

$$\Delta g_1^Z \equiv g_1^Z - 1,\ \Delta\kappa_Z \equiv \kappa_Z - 1,\ \lambda_Z \tag{1.2}$$

Other studies, which are sensitive to both the WWZ and $WW\gamma$ couplings, have customarily made assumptions about the relations between the WWZ and $WW\gamma$ coupling parameters. Although a measurement of WZ production is a direct measure of the WWZ vertex coupling parameters it is useful to relate these parameters to the coupling parameters for the $WW\gamma$ vertex for comparison with other diboson studies. This is accomplished using two different schemes. In the "equal couplings" scheme the WWZ and $WW\gamma$ couplings are assumed to vary by the same amount. Because $\Delta g_1^\gamma \equiv 1$ by electromagnetic invariance, Δg_1^Z is fixed at 1, leaving two free parameters: $\lambda = \lambda_Z = \lambda_\gamma$ and $\Delta\kappa = \Delta\kappa_Z = \Delta\kappa_\gamma$. In the HISZ scheme [25], the couplings are formulated in a framework which explicitly respects $SU(2) \times U(1)$ gauge invariance. In this scheme the WWZ coupling parameters are related to the $WW\gamma$ parameters by:

$$\Delta g_1^Z = \frac{1}{2\cos^2\theta_W}\Delta\kappa_\gamma \tag{1.3}$$

$$\Delta\kappa_Z = \frac{1}{2}(1 - \tan^2\theta_W)\Delta\kappa_\gamma \tag{1.4}$$

$$\lambda_Z = \lambda_\gamma \tag{1.5}$$

For WZ production the scattering amplitude, $\mathcal{M}_{\lambda_Z\lambda_W}$, for a Z boson of helicity λ_Z and a W boson of helicity λ_W is enhanced for anomalous couplings. The $\mathcal{M}_{\pm,\pm}$ helicity amplitudes are enhanced by $\hat{s}/m_W^2$ for anomalous values of λ_Z and the $\mathcal{M}_{0,0}$ amplitude is similarly enhanced for Δg_1^Z. Non-Standard Model values of

$\Delta\kappa_Z$ effect $\mathcal{M}_{\pm,0}$ and $\mathcal{M}_{0,\pm}$, but only like $\sqrt{\hat{s}}/m_W$ [2]. Thus the non-Standard Model amplitudes rise without limits as $\hat{s}$ increases and violate partial wave unitarity.

Since the anomalous contribution appears only in the s-channel process, the $l = 0$ term in the partial wave expansion must be explicitly controlled. To control the high energy behavior of the scattering amplitudes, the coupling parameters are modified by form factors, i.e.

$$\lambda \to \lambda(\hat{s}) = \lambda/(1 + \frac{\hat{s}}{\Lambda^2})^n. \tag{1.6}$$

For WWZ couplings, the choice of $n = 2$ is sufficient to bring the high energy behavior under control. The parameter Λ is the form factor scale.

For a particular choice of scale Λ, the unitarity requirement places constraints on the allowed values of the couplings [26]. If only one coupling parameter at a time is allowed to vary, the couplings are bounded by

$$|\Delta g_1^Z| \leq \frac{3.36 \text{ TeV}^2}{\Lambda^2} \tag{1.7}$$

$$|\lambda_Z| \leq \frac{2.08 \text{ TeV}^2}{\Lambda^2} \tag{1.8}$$

$$|\Delta\kappa_Z| \leq \frac{3.32 \text{ TeV}^2}{\Lambda^2} \tag{1.9}$$

[2] In fact all diboson processes show a $\hat{s}/m_W^2$ enhancement for anomalous λ. For Δg_1^Z however, it is only WZ production which grows as $\hat{s}$. For $\Delta\kappa$ only WW production grows linearly with $\hat{s}$. Thus WZ production is most sensitive to Δg_1^Z while WW production is most sensitive to $\Delta\kappa$.

1.4.3 Experimental Signatures of non-Standard Model WZ Production

Anomalous couplings can be detected by their influence on observables. The first is a dramatic increase in cross section. Recall from Section 1.3.2 that the s-channel diagram is required at its Standard Model strength to produce the "delicate" gauge cancellation which controls WZ production. The presence of anomalous couplings changes those values and disrupts the cancellation. The larger the deviation from the Standard Model, the larger the disruption. The result is that for anomalous couplings the cross section is greatly increased (see Fig. 1.5).

In addition to the total cross section, the differential distributions are also sensitive to non-Standard Model couplings. For large values of WZ invariant mass, the anomalous contributions to the helicity amplitudes dominate the Standard Model contributions. Because the anomalous contributions come only in the s-channel, their affects tend to be concentrated in regions of small boson rapidity. Thus the transverse momentum of the bosons and their decay products is enhanced by the presence of anomalous couplings, particularly at large transverse momentum [27]. Figure 1.6 shows the distribution of p_T^Z for Standard Model and anomalous couplings and Figure 1.7 shows the p_T distribution of the electron from the W for Standard Model and anomalous couplings.

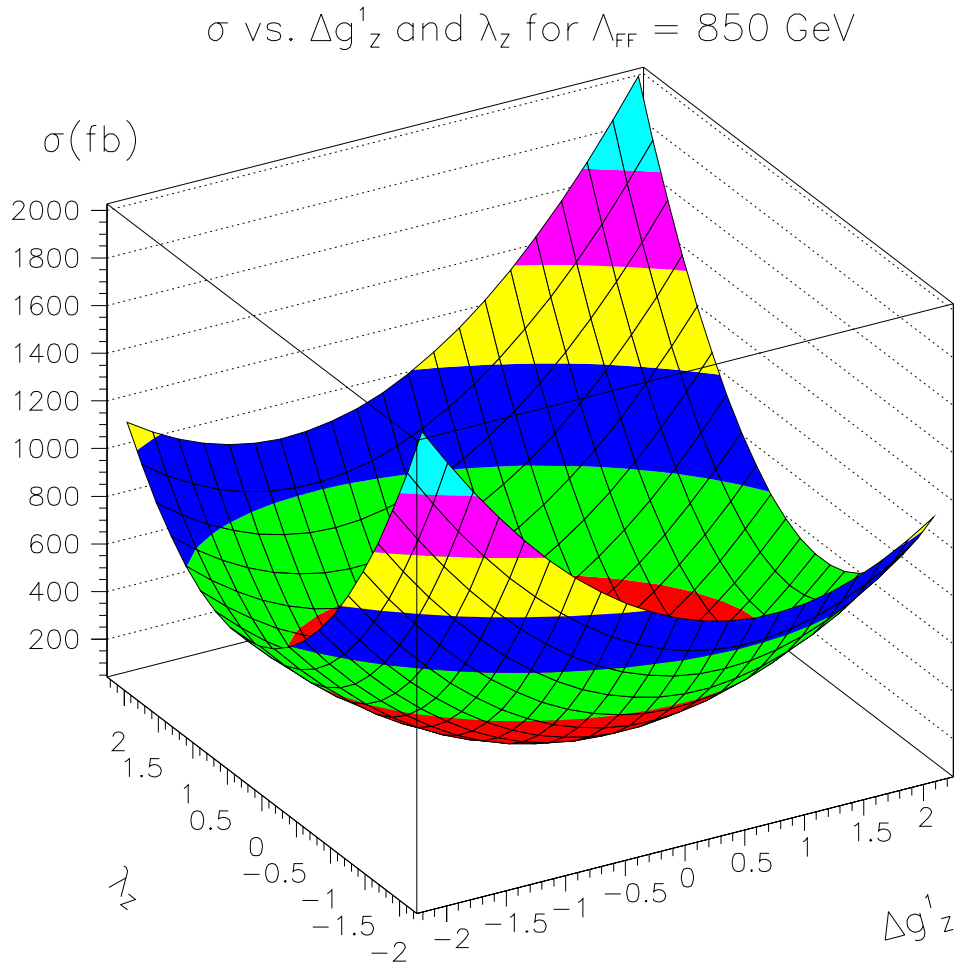

Figure 1.5: Cross section as a function of Δg_1^Z and λ_Z for WZ production with subsequent decay to electrons and/or muons for $\Lambda = 850$ GeV.

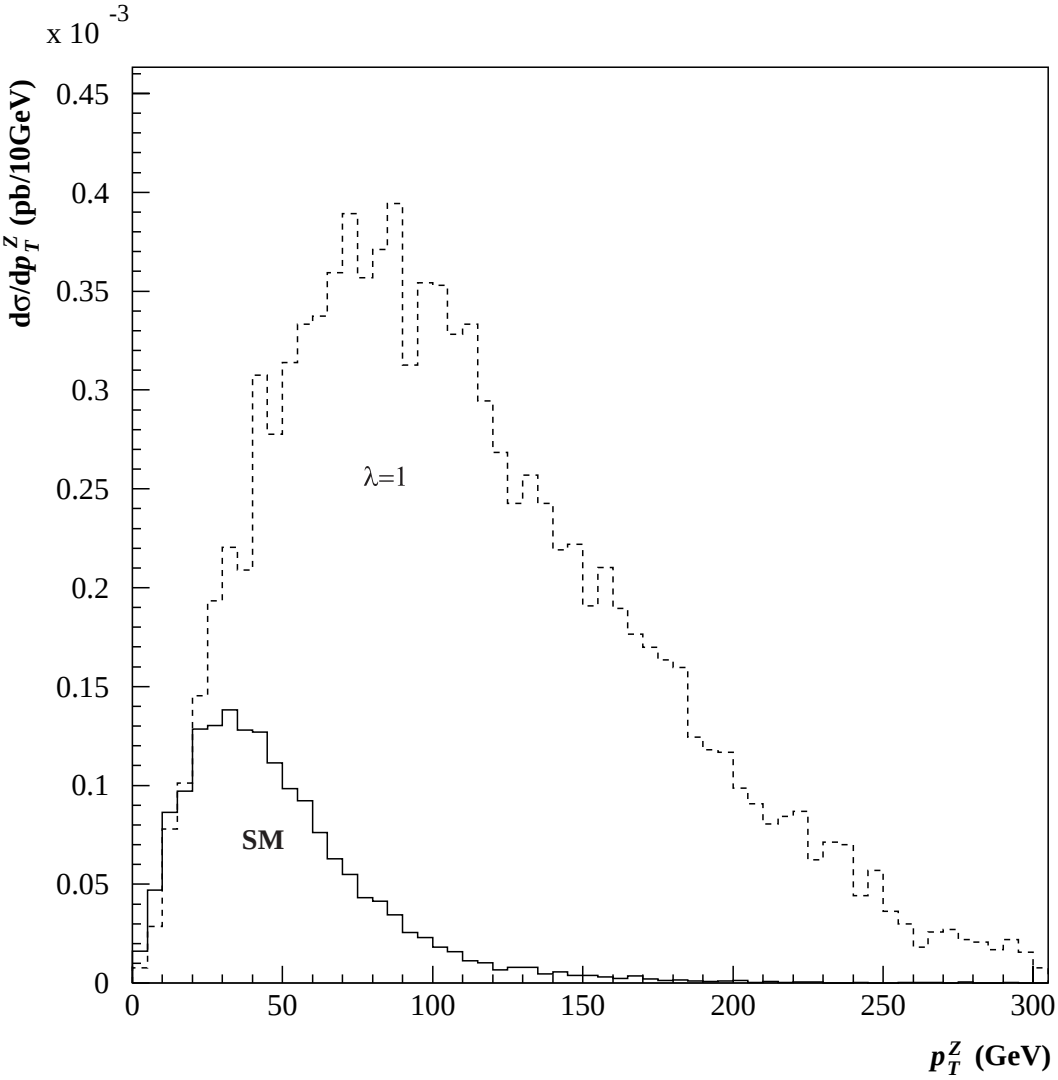

Figure 1.6: $d\sigma/dp_T^Z$ vs p_T^Z for Standard Model WZ production (solid histogram) and anomalous WZ production (dashed histogram).

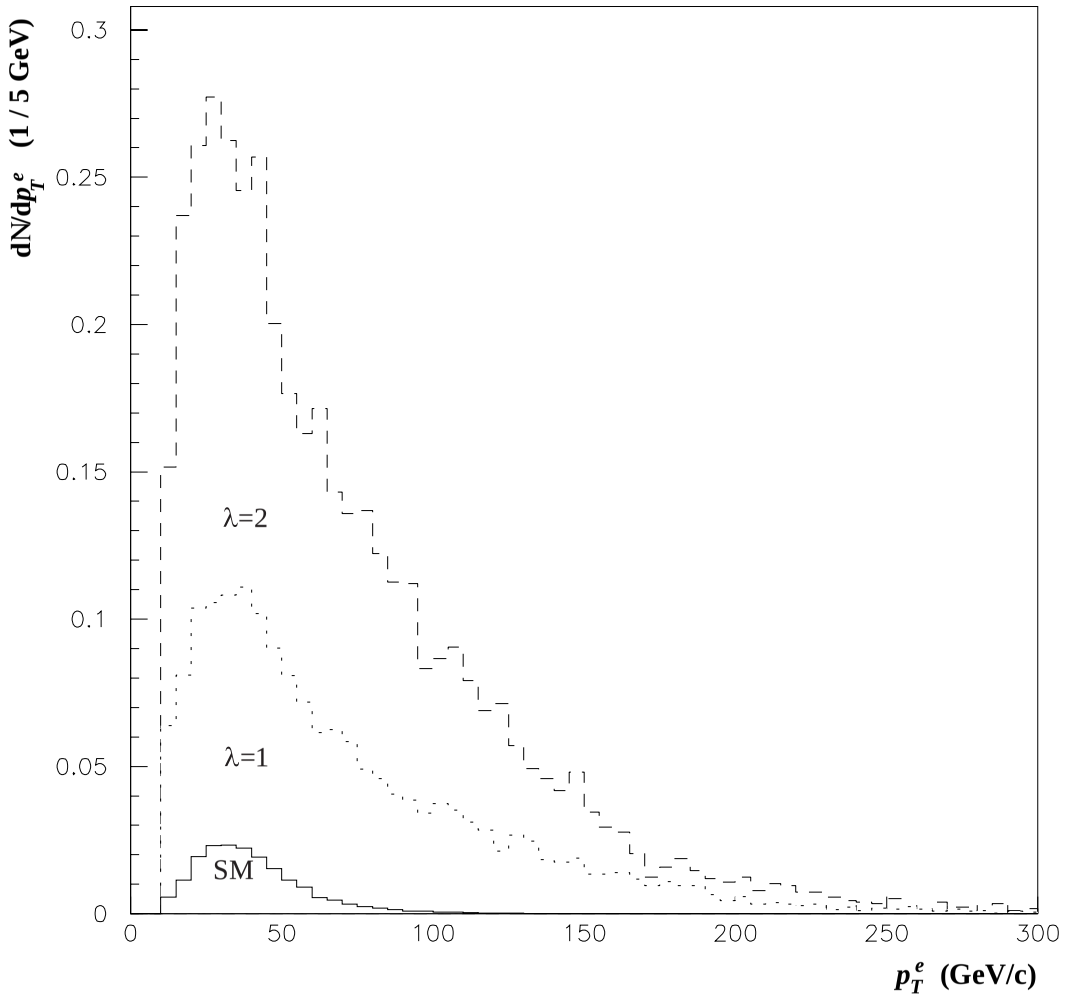

Figure 1.7: dN/dp_T^e vs p_T^e for Standard Model WZ production (solid histogram) and anomalous WZ production (dashed and dotted histograms).

1.5 Previous Experimental Results

Limits can be placed on the coupling parameters by performing a likelihood test on the measured cross section or kinematic distributions, such as the boson transverse momentum. To put the results of this analysis in context, the limits on anomalous couplings obtained from other diboson analyses are presented.

The $WW\gamma$ couplings were first measured at the UA2 experiment at CERN to be [28]

$$-4.5 < \Delta\kappa_\gamma < 4.9(\lambda_\gamma = 0) \ -3.6 < \lambda < 3.5(\Delta\kappa_\gamma = 0)$$

At the Tevatron, CDF reported limits obtained from 20 pb^{-1} of data of [29]

$$-2.3 < \Delta\kappa_\gamma < 2.2(\lambda_\gamma = 0) \ -0.7 < \lambda_\gamma < 0.7(\Delta\kappa_\gamma = 0)$$

while DØ derived limits of [30]

$$-0.93 < \Delta\kappa_\gamma < 0.94(\lambda_\gamma = 0) \ -0.31 < \lambda_\gamma < 0.29(\Delta\kappa_\gamma = 0)$$

from a full data set of approximately 93 pb^{-1}. The Tevatron limits are obtained assuming a form factor scale of 1.5 TeV.

Measurements of the $WW\gamma$ and WWZ couplings have been made through WW and WZ final states. The limits are quoted assuming the "equal couplings" scenario where the $WW\gamma$ and WWZ couplings are set equal ($\Delta\kappa_\gamma = \Delta\kappa_Z = \Delta\kappa,\ \lambda_\gamma = \lambda_Z = \lambda$).

CDF has measured WW and WZ production in the $l\nu jj$ and $l\bar{l}jj$ $(l = e, \mu)$ channels to obtain limits of [31]

$$-1.11 < \Delta\kappa < 1.27(\lambda = 0) \ -0.81 < \lambda < 0.84(\Delta\kappa = 0)$$

from 20 pb^{-1} of data using a form factor of 1.5 TeV. DØ has measured WW and WZ production in the $e\nu jj$ channel using 96 pb^{-1} of data to set limits of [32]

$$-0.43 < \Delta\kappa < 0.59(\lambda = 0) \ -0.33 < \lambda < 0.36(\Delta\kappa = 0)$$

assuming a form factor scale of 2.0 TeV. CDF has published coupling limits obtained from measuring WW production in the $l\nu l'\nu'$ $(l, l' = e, \mu)$ channel of [33]

$$-1.05 < \Delta\kappa < 1.30(\lambda = 0) \ -0.90 < \lambda < 0.90(\Delta\kappa = 0)$$

using 108 pb^{-1} of data and assuming a form factor scale of 1.0 TeV. WW production in the $(l\nu l'\nu' \ l, l' = e, \mu)$ channel was measured at DØ using 97 pb^{-1} of data to set limits of [34]

$$-0.62 < \Delta\kappa < 0.77(\lambda = 0) \ -0.52 < \lambda < 0.56(\Delta\kappa = 0)$$

for a form factor scale of 1.5 TeV.

DØ has recently performed a simultaneous fit to the photon p_T distribution in the $W\gamma$ data, the lepton p_T in the $WW \to l\nu l'\nu'$ data and the $p_T^{e\nu}$ distribution in the $WW/WZ \to e\nu jj$ data. The resulting limits on the coupling parameters obtained from this fit are [35]

$$-0.30 < \Delta\kappa < 0.43 \ -0.20 < \lambda < 0.20$$

for a form factor of 2 TeV.

The process $e^+e^- \to WW$ has been studied by the ALEPH, DELPH, L3, and OPAL experiments at LEP. With approximately 55 pb^{-1} of data per experiment at $\sqrt{s} = 183$ GeV the following coupling limits were obtained from a combination of limits from individual experiments [36]:

$$-0.21 < \lambda_Z < 0.27; -0.12 < \Delta\kappa_Z < 0.13.$$

Chapter 2

Experimental Apparatus

The electroweak bosons can be created by colliding protons and antiprotons with sufficient energy. The Tevatron [37] at Fermi National Accelerator Laboratory (Fermilab), located near Chicago, Illinois, is the highest energy proton-antiproton collider in operation. The Tevatron provides a center of mass collision energy of 1.8 TeV, which is more than sufficient to produce a pair of massive bosons. In the following section, a description is given of how proton and antiproton beams are obtained.

In order to detect the production of the electroweak boson and the subsequent decay products, it is necessary to build a detector around the collision point. The DØ detector is an all-purpose detector for identifying the decay products of proton antiproton collisions. The second part of the chapter is dedicated to a description of the subsystems of the DØ detector: the central tracking detector, the calorimeter,

and the muon spectrometer. Finally a system for triggering on inelastic proton antiproton collisions and recording the triggered data is needed. The final section of this chapter gives an overview of data collection.

2.1 The FNAL Collider Complex

The Fermilab accelerator complex consists of a series of accelerators, each of which is effective in a particular energy regime. They create protons and antiprotons and accelerate them to a center-of-mass collision energy of 1.8 TeV. The accelerator complex is shown in Figure 2.1. What follows is a non-technical description of the accelerator complex. The interested reader should consult [38] for a more detailed description.

The pre-accelerator consists of the plasma source and Cockcroft-Walton generator. In the plasma source hydrogen gas is ionized into a plasma and extracted with a typical energy of 18 keV. The plasma is passed through a bumper magnet which separates the negative ions from any free electrons. The ions are then passed into the Cockcroft-Walton generator. Inside the generator the ions are accelerated across a series of capacitors to an energy of 750 keV.

The ions are next passed through a 150 meter linear accelerator which accelerates the ions to 400 MeV. The ions are then passed through a carbon foil to strip off the electrons leaving bare protons.

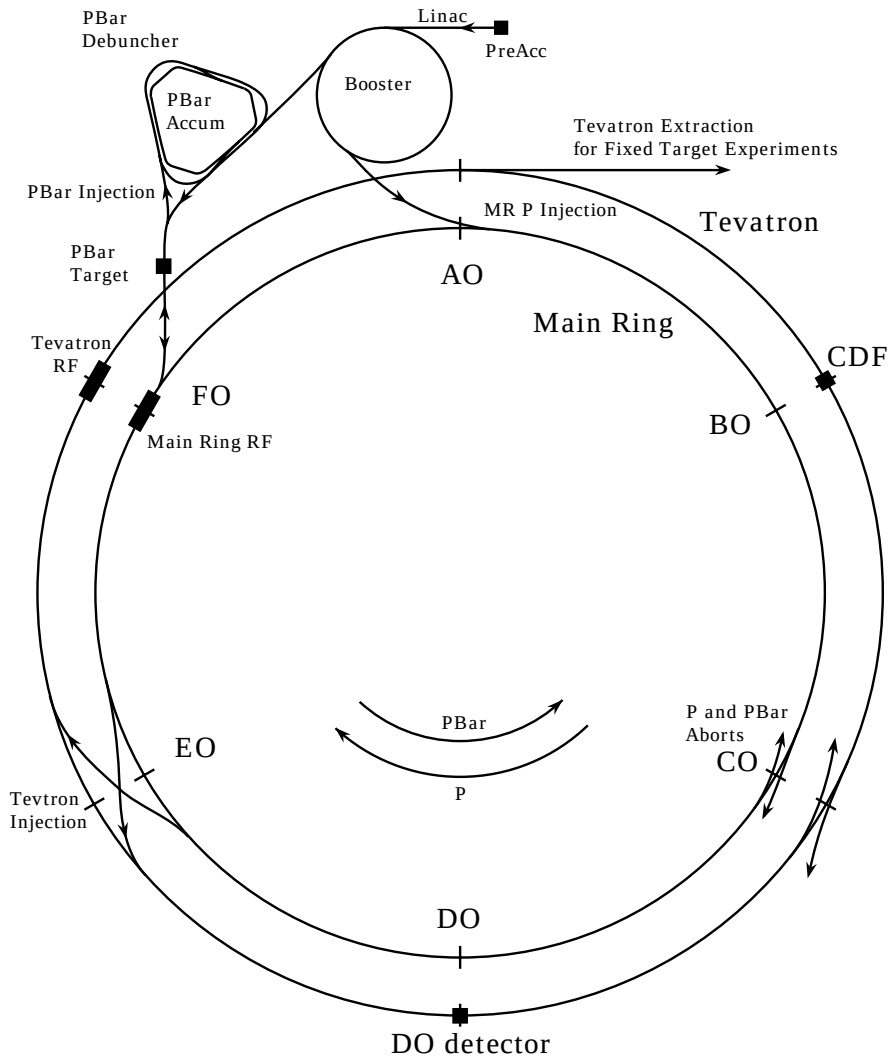

Figure 2.1: Schematic of the FNAL facility (not to scale).

The bare protons enter into the Booster, a synchrotron of radius 151 meters. A synchrotron is a ring of bending magnets which keep a beam of particles in a closed orbit. The beam is accelerated by passing it through a radio frequency cavity. As the beam energy increases the magnetic fields of the magnets are increased in a synchronous manner to maintain a closed orbit. In this fashion the protons are

accelerated from 400 MeV to 8 GeV. The "beam" of protons consists of discreet "bunches" of protons which are separated by regions with no protons. Bunches produced in the linear accelerator (linac) are merged together in the Booster with each bunch consisting of 6 linac bunches.

The Main Ring is a synchrotron of radius 1 kilometer which uses conventional magnets. The Main Ring can accelerate the beam to a maximum energy of 400 GeV, which was the highest beam energy at the time of its construction in the 1970's. The Main Ring serves two roles. It accelerates protons to 120 GeV and directs them to a target for the production of antiprotons and it accelerates protons to 150 GeV for injection into the Tevatron.

The process of antiproton production is slow, requiring contiguous antiproton generation even while the Tevatron collides proton and antiproton beams. To create antiprotons a beam of protons from the main ring is directed onto a nickel target. The nuclear debris from this collision, which will contain antiprotons, is passed through a lithium cylinder which carries a pulsed current of 0.5 MA. The induced magnetic field focuses negatively charged particles along the axis of the cylinder. A dipole magnet selects 8 GeV antiprotons and directs them into the Debuncher. The Debuncher is a storage ring which reduces the momentum spread of the antiprotons [39]. The antiprotons are then added to any antiprotons that are already stored in the Accumulator ring for later injection into the Tevatron via the Main Ring. The yield is 10^7 antiprotons for every 10^{12} protons collided with the

target.

In the Main Ring, proton or antiproton bunches are merged before injection into the Tevatron. The Main Ring and the Tevatron share the same accelerator tunnel, with the Tevatron suspended 2 feet below the Main Ring. Because the Main Ring must continue to operate during Tevatron running, the Main Ring is bent upward to arch over ring location BØ (the location of the CDF detector). At the time of the Tevatron construction a prototype "overpass" was built at location DØ in anticipation of a second collider detector. Because there was no second collider detector at that time the prototype had a separation of 89 inches to fit within the existing accelerator tunnel. In contrast, the BØ overpass achieved a separation of 19 feet after major tunnel reconstruction. As a result of the smaller separation at the DØ overpass, the Main Ring passes through the DØ calorimeter, making data taken during Main Ring activity more complicated.

The Tevatron uses superconducting magnets to accelerate the protons and antiprotons from injection beam energy of 150 GeV to a maximum beam energy of 900 GeV. The superconducting magnets require liquid helium cooling to achieve an operating temperature of 4.6 K. In contrast, the conventional magnets of the Main Ring only require water cooling. With equal mass and opposite charges, the protons and antiprotons can share the same accelerating fields and thus the same beampipe.

With few exceptions, the Tevatron was operated with 6 proton bunches counter rotating with 6 antiproton bunches. The beams are separated by a small

vertical displacement minimizing the number of collisions outside of the detector regions. At the detector sites, quadrapole magnets on either side of the collision hall focus the beam cross section to $\sigma_{x,y} \approx 40\mu$m. This focusing maximizes the luminosity ($\mathcal{L} = \frac{particle\ \ crossings}{cm^2 \cdot sec}$) at the center of the detectors. The magnets also defocus the beams after collision to maximize beam lifetime. The beams are allowed to collide uninterrupted for a time period of 12-18 hours, often referred to as a store, at which time they are directed into their dump sites and fresh bunches are injected.

2.2 Overview of the DØ Detector

The DØ detector was designed to measure the decay products of interest in $p\bar{p}$ collisions: electrons, photons, muons, parton jets, and missing transverse energy ($\not\!\!E_T$) which signals the presence of non-interacting particles such as neutrinos. The detector is composed of three subsystems: the tracking detectors, the calorimeter and the muon spectrometer (Figure 2.2). The design of the detector emphasized finely segmented, hermetic calorimetry for the sole measurement of particle energies. Because of this the tracking volume is compact and has no magnetic field for momentum measurement. The detector is described in detail in Reference [40] and this description is well complimented by Reference [41].

The detector is mounted on a movable platform for movement in and out of the collision hall. The first stage of detector readout electronics are mounted on

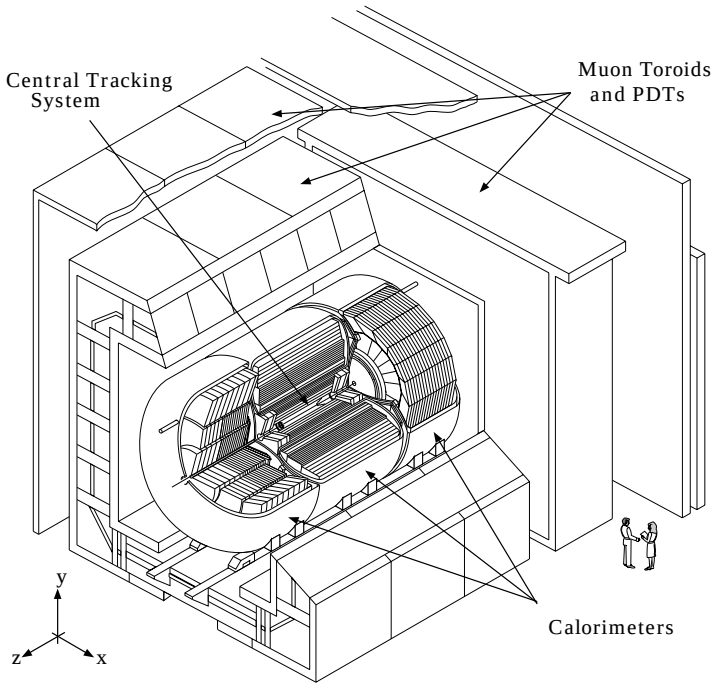

Figure 2.2: Isometric cutaway view of the DØ detector.

the platform as well as services for power, gas and cryogenics. The signals are read out through cables which pass though the shield wall to the moving counting house (MCH) for the next stage of signal processing. The moving counting house was made mobile so that it can be moved with the detector, thus shortening the length of cabling needed. From the MCH, data is passed over high speed connections to the control room (fixed counting house) for event monitoring.

A right-handed coordinate system is used in describing the detector, with the origin at the center of the detector and the beam pipe, the positive z-axis defined as the direction of the proton beam, and the positive y-axis pointing up. A cylindrical

coordinate system is also used, with ϕ measured with respect to the positive x-axis, and θ measured from the positive z-axis.

In describing the kinematics of detected particles several approximations are taken for convenience. For a particle not at rest in the lab frame with energy E and momentum p, the rapidity y is defined as

$$y = \frac{1}{2} \ln \frac{E + p_z}{E - p_z}. \tag{2.1}$$

In the limit $p >> m$, it is possible to approximate the rapidity as follows

$$y \approx -\ln \tan \frac{\theta}{2} \equiv \eta. \tag{2.2}$$

where η is called the pseudorapidity. The polar angle is often expressed in terms of "detector pseudorapidity", denoted η_{det}, which is referenced to $z = 0$. The interaction point does not always coincide with the center of the detector, making η and η_{det} slightly different.

In $p\bar{p}$ collisions, the momenta of the colliding partons along the beam cannot be reconstructed since many of the remnants of the collision are carried away down the beam pipe. It is convenient then to use the transverse momentum, which is the projection of the momentum vector in a plane perpendicular to the beam axis, $p_T = p \sin\theta$, instead of the momentum. If energy deposition in the calorimeter is treated as a vector, it is convenient to define the transverse energy, $E_T = E \sin\theta$. The direction of E_T can be taken as the direction of p_T. Also, only the transverse component of missing energy is measured.

In the following sections the detector subsystems are discussed in more detail, with an emphasis placed on the subsystems used in this analysis.

2.3 The Central Detector

The Central Detector (CD), shown in Figure 2.3, is composed of four subsystems. The Vertex Drift Chamber (VTX), the Transition Radiation Detector (TRD) and the Central Drift Chamber (CDC) are cylindrical devices which are arranged concentrically around the beam pipe and cover the region of large angles. The fourth subsystem consists of two Forward Drift Chambers (FDC) which are oriented perpendicularly to the beam pipe. The CD occupies a volume bounded by 3.7 cm $< r <$ 75 cm and $|z| <$ 135 cm.

In the absence of a central magnetic field, the momenta of particles are not measured by the tracking chambers. Instead the tracking chambers were designed for good two-track resolution, high efficiency and good ionization energy measurement. The TRD was added for additional rejection of isolated pions as a background for electrons.

The tracking detectors were designed to match the 3.5 μs interval between beam crossings. Flash analog-to-digital converters were used to digitize the signal in 10 ns intervals to obtain good two-track resolving power.

Three of the four tracking detectors are wire drift chambers: the VTX, the

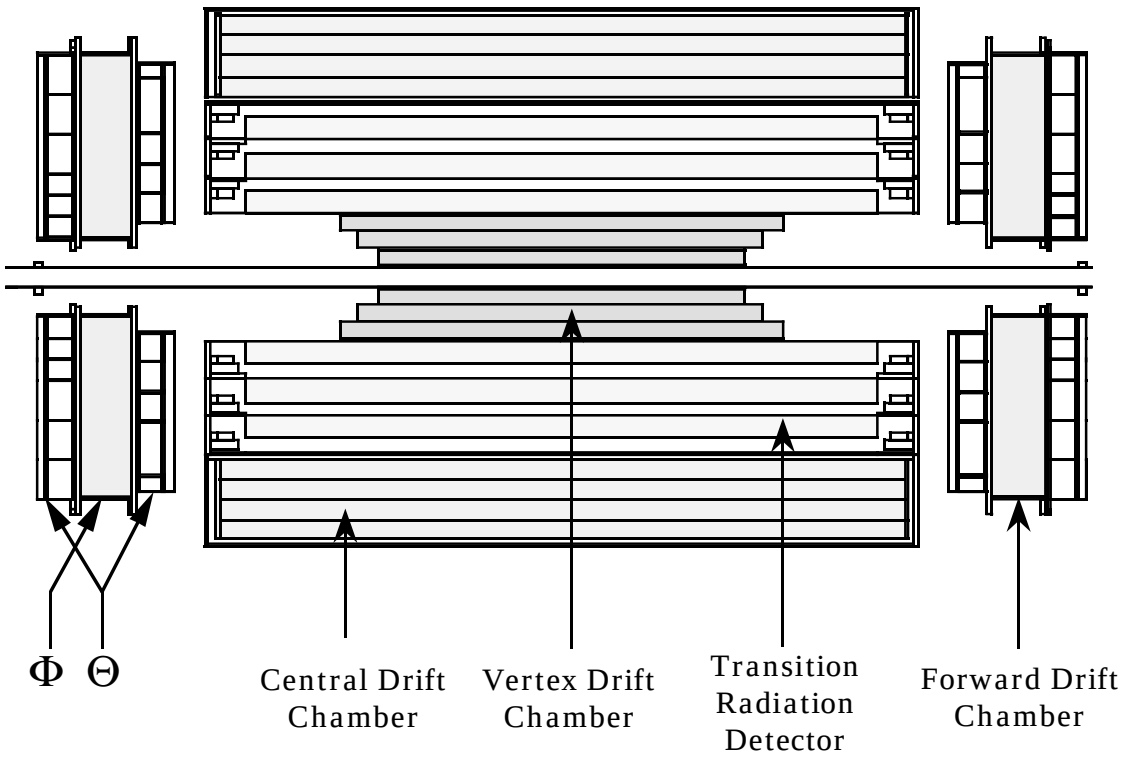

Figure 2.3: Side view of the DØ central tracking detectors.

CDC and the FDC. The reader is referred to [42] for a detailed discussion of the principles of drift chambers. An overview of the principles of wire drift chambers is presented below.

As a charged particle passes through a gas it interacts electromagnetically with nearby atomic electrons. This process produces ion-electron pairs along the trajectory of the particle. In the presence of an electric field the electrons will drift toward the positive electrode wire, called a *sense wire*. The ions drift in the opposite direction but their drift velocity is considerably slower than that of electrons making it safe to ignore their motion. In a multiwire drift chamber several such

drift wires are strung in parallel. The ionized electrons drift to the closest wire to the point of their creation. A small diameter sense wire produces a very strong electric field near it. This strong field accelerates drift electrons to energies high enough to produce further ionization. In this manner, the number of electrons increases exponentially producing an *avalanche* of electrons, thus giving rise to a large measurable electrical current whose size is proportional to the original number of ion-electron pairs created. The ratio of the number of electrons collected and the number of electrons produces initially is referred to as the *gas gain*, and it typically of the order of 10^4 to 10^6.

The drift velocity of the electrons is independent of the particle that produced the ionization, but it is dependent on the strength of the electric field and the gas composition, temperature and pressure. The drift time, the difference between the known collision time and the arrival time of the pulse in the sense wire, is combined with the drift velocity in order to infer the drift distance of the electrons. It is necessary to ensure a constant electric field over as large a volume as possible in order to obtain a linear relationship between distance and time. Additional field shaping cathodes are inserted in order to make the field more uniform. From the inferred drift distances, the trajectories of charged particles are reconstructed.

The reader is encouraged to read [42, 43, 44] for further discussion of drift chambers and their application in high energy physics.

2.3.1 Vertex Drift Chamber

The Vertex Drift Chamber (VTX) [45, 46, 47] is the innermost of DØ's tracking chambers. It was designed to provide precise determination of the location of interaction vertices. Occupying the region 3.7 cm $< r <$ 16.2 cm, it is composed of three concentric and cylindrical layers with the inner layer measuring 97 cm in length and each successive layer being about 10 cm longer. A cross section of one quadrant of the VTX chamber is shown in Figure 2.4.

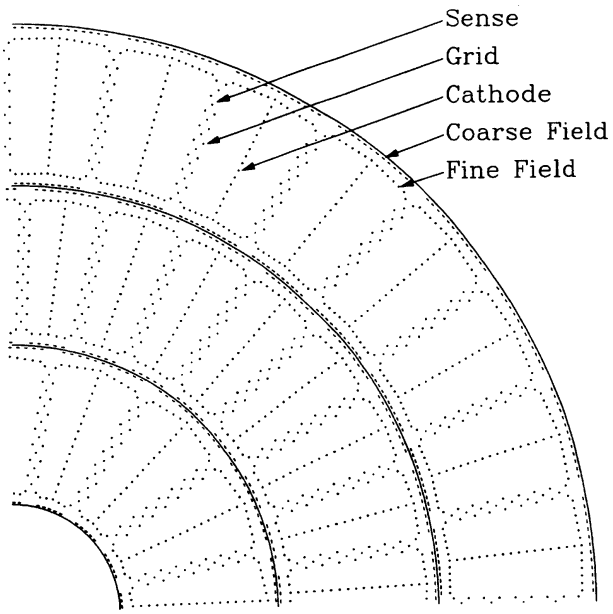

Figure 2.4: Cross sectional $r\phi$ view of one quadrant of the VTX chamber.

The innermost layer of the VTX chamber consists of 16 azimuthal cells and the outer two consist of 32 cells each. Each cell has eight 25 μm nickel-cobalt-tin (NiCoSn) sense wires, which are staggered by $\pm$ 100 μm azimuthally in order to

resolve left-right ambiguity. Cells are offset azimuthally in each successive layer to further enhance pattern recognition. The $r\phi$ coordinate of a hit is determined from drift time and wire position with a position resolution of approximately 60 μm. The z-coordinate is determined from charge division along the wire. However, the observed z-position resolution was poor in a high luminosity environment and the VTX was not used for determination of the primary vertex z position.

2.3.2 Transition Radiation Detector

The Transition Radiation Detector (TRD) [48, 49] occupies the space just beyond the radius of the VTX. The TRD is primarily used to distinguish electrons from charged pions. The TRD measures the emission of transition X-rays by highly relativistic charged particles ($\gamma > 10^3$) when they cross the boundary separating media with different dielectric constants. The TRD was not used in this analysis because of the need to retain high efficiency.

2.3.3 Central Drift Chamber

The outermost tracking detector, the Central Drift Chamber (CDC) [46, 50, 51, 52] consists of four cylindrical, concentric layers. The CDC provides trajectory and ionization information on isolated charged particles out to a detector pseudo-rapidity of $|\eta_{det}| < 1.2$. The CDC occupies the radial region between 49.5 cm and 74.5 cm and is 184 cm in length.

Each CDC layer is divided into 32 modular, azimuthal cells. A cross section of three such cells is shown in Figure 2.5. Each cell contains seven 30 μm gold-plated tungsten sense wires and two delay lines. The sense wires are staggered by $\pm$ 200 μm azimuthally to reduce left-right ambiguity and alternate cells are offset azimuthally by half a cell to enhance pattern recognition. The $r\phi$ coordinate of a hit is obtained from the drift time information and from the wire hit. The z position is inferred via the use of delay lines. Whenever an avalanche occurs near a delay line a pulse is induced in the delay line. The difference in the arrival times at both ends of the delay line gives an estimate of where along the delay line the hit occurred. The $r\phi$ and z resolutions are approximately 180 μm and 2.9 mm respectively.

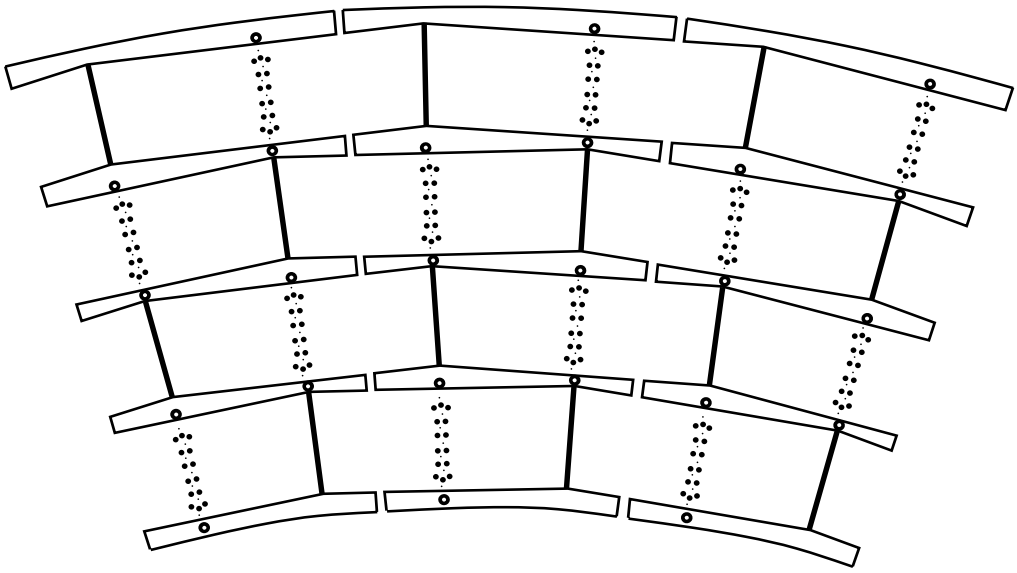

Figure 2.5: End view of three CDC modules. Sense wires are indicated by small dots, guard (field shape) wires by large dots, and delay lines by open circles.

2.3.4 Forward Drift Chambers

The Forward Drift Chambers [46, 50, 53, 54] are located at both ends of the CD system. They extend the outer tracking coverage down to an angle of $\theta \approx 5^{\circ}$ or a detector pseudorapidity of $|\eta_{det}| < 3.1$. These two chambers are each composed of three modules: a Φ module sandwiched between two Θ module. The Φ module has sense wires oriented axially to measure the ϕ coordinate of hits. Each Θ module is made of four quadrants, which have sense wires oriented perpendicular to the beamline to measure the θ coordinate of hits. The layout of the FDC is illustrated in Figure 2.6.

A Φ module is made up of 36 azimuthal cells, each containing 16 axial sense wires of length 50 cm that are arranged perpendicular to the beam pipe. Each of the four quadrants of a Θ module contains six rectangular cells, located at increasing radii. Each cell contains eight sense wires and one delay line. The sense wires in the Φ and Θ modules are staggered by $\pm$ 200 μm to help resolve left-right ambiguity. In addition, the two Θ chambers are rotated by 45° to aid pattern recognition. The spatial resolutions are 200 μm and 300 μm for the Φ and Θ modules respectively.

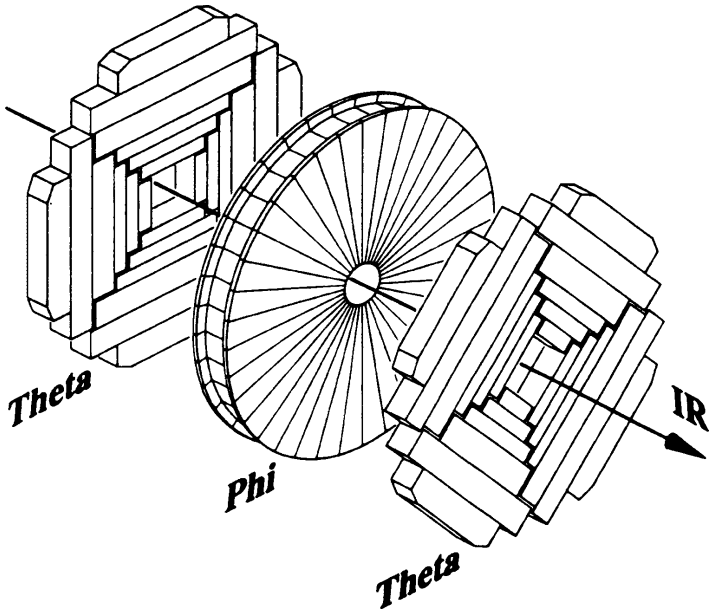

Figure 2.6: Exploded isometric view of one half of the FDC tracking system.

2.3.5 Central Detector Readout

Central Detectors devices are read out in three stages. The signals from the chamber wires are lead to preamplifiers mounted directly on the chambers themselves. These signals are then fed into analog pulse shaping cards located on the support platform underneath the detector. The signals are then sent to the MCH, where the signals are sampled and digitized by Flash Analog-To-Digital (FADC) converters at the rate of 106 MHz (starting with the beam crossing). If a Level 1 trigger is fired, the data is compressed by eliminating the flat portions of the signal between the pulses and sent on to the Level 2 trigger, otherwise the data is overwritten by data from the next crossing.

2.4 Calorimetry

The Calorimeter system at DØ is the most crucial part of the DØ detector since it provides the only means to measure the energy of electrons, photons, and jets. Furthermore, it plays a vital role in the identification of neutrinos through the transverse imbalance of energy.

A calorimeter is a block of material which is placed in the path of a particle and is of sufficient thickness to cause it to interact and deposit all of its energy in the medium. Some percentage of the energy deposited is detectable in the form of scintillation light or ionization charge which is proportional to the incident energy of the particle.

At energies above 1 GeV, photons and electrons dissipate their energy at an energy independent rate via electron-positron pair production and Bremsstrahlung respectively. An incident electron or photon will produce a shower of secondary particles by these loss mechanisms. For example an electron will produce a photon, which will in turn produce a electron-positron pair, which in turn will produce photons, *etc.* This process will continue until all secondary particles drop below the energy at which ionization of the medium becomes the primary energy loss mechanism.

The energy loss ΔE by radiation in a length Δx can be written as

$$(\Delta E)_{\text{raditation}} = -E(\Delta x / X_{\circ})$$

where $X_\circ$ is the "radiation length" of a material. The radiation length is approximated by

$$X_\circ[\mathrm{g/cm^2}] \approx 180\mathrm{A/Z^2}.$$

The energy loss by ionization in a medium is characterized by the "critical energy" ϵ below which ionization losses dominate. The energy loss by an electron/positron of energy ϵ in medium in radiation length $X_\circ$ is given by

$$(dE)_{\mathrm{collision}} = -\epsilon(dx/X_\circ)$$

where $\epsilon(\mathrm{MeV}) \approx 500/\mathrm{Z}$.

The total track length of secondaries in an electromagnetic shower is given by $T = (E/\epsilon)X_\circ$ with the peak multiplicity of the shower occurring at

$\approx$ (ln (E/ϵ) $-$ 2) $X_\circ$.

The transverse profile of a shower is characterized by the typical angle for bremsstrahlung emission and multiple scattering in the medium. About 90% of the total energy of a shower is contained within a cylinder of radius $2\rho_M$, where

$$\rho_M = 21X_\circ/\epsilon \approx 7\frac{\mathrm{A}}{\mathrm{Z}}\,[\mathrm{g\,cm^{-2}}]$$

is the "Moliere Radius", which is the average lateral deflection of electrons of energy ϵ after traveling one radiation length.

Two types of calorimeter can be used to measure the energy of particles. A homogeneous calorimeter is composed of one material such as sodium iodide (NaI)

or lead glass. A sampling calorimeter uses a dense passive absorber interspersed with an active medium which samples the energy of the shower at various points in its development. A homogeneous calorimeter can achieve a better energy resolution than a sampling calorimeter, but a sampling calorimeter is usually much more compact than a homogeneous calorimeter because of the dense absorber.

The energy resolution of a sampling calorimeter is limited by the statistical fluctuations of the amount of ionization in the sampling layers. The fractional error in the energy is proportional to one over the square root of the number of ionizing tracks or equivalently, $E^{-\frac{1}{2}}$.

The energy measurement of hadronic showers is conceptually analogous to electromagnetic showers. Hadrons interact by inelastic collisions with atomic nuclei in the medium, producing secondary hadrons which repeat the process, creating a shower of hadronic particles. The greater variety and complexity of the hadronic processes propagating the shower make an analytic description difficult. We can however give some general features.

The scale for hadronic interactions is the nuclear interaction length

$$\lambda_A \approx 35\mathrm{A}^{1/3}[\mathrm{g/cm}^2].$$

The average shower maximum occurs at $\approx (0.2 \ln E + 0.7)\lambda_A$ where E is measured in GeV. About 90% of the energy is contained within $2.5\lambda_A$ of the shower maximum. In the transverse direction, 95% of the energy is contained within a cylinder of radius

$R \leq 1\lambda_A$.

Fluctuations in the constituent particles of hadronic showers are the principal limitation to the energy resolution. The response of a calorimeter will differ for hadrons and electrons of the same energy. If the fraction of π^0's and η^0's produced in the first interaction is large, most of the energy will be measured as these particles quickly decay to two photons. If the interactions produce muons and neutrinos, most of the energy will be carried away. Thus the calorimeter response to hadrons is typically less than for electrons. This difference, the "e/h ratio", can be corrected for on average, but a ratio different from one will result in fluctuations on a shower by shower basis. An e/h ratio near unity can be achieved by decreasing the electron response or boosting the hadronic response. The latter can be achieved by using uranium-238, because secondary neutrons can cause fission in the uranium nuclei which produces some visible energy.

For further discussions on calorimeters, the reader is referred to [43, 44], as well as articles [55, 56].

2.4.1 Calorimeter Design

The DØ Calorimeter is a sampling calorimeter. Liquid argon (LAr) was chosen as the active medium because of its unit gain, simplicity of calibration, flexibility in the segmentation of readout cells and resistance to radiation damage. The use of LAr requires a containment vessel (cryostat), where the argon is kept cold

enough to remain in the liquid form. As shown in Figure 2.7, the Calorimeter was split into three modules, one Central Cryostat (CC) covering the region $|\eta| < 1.2$, two Endcap Cryostats (EC) extending the coverage to $|\eta| \approx 4$. This was done to retail access to the tracking detectors. The design left an uninstrumented region between the cryostats. The Inter-cryostat Detector (ICD) was built to cover this region.

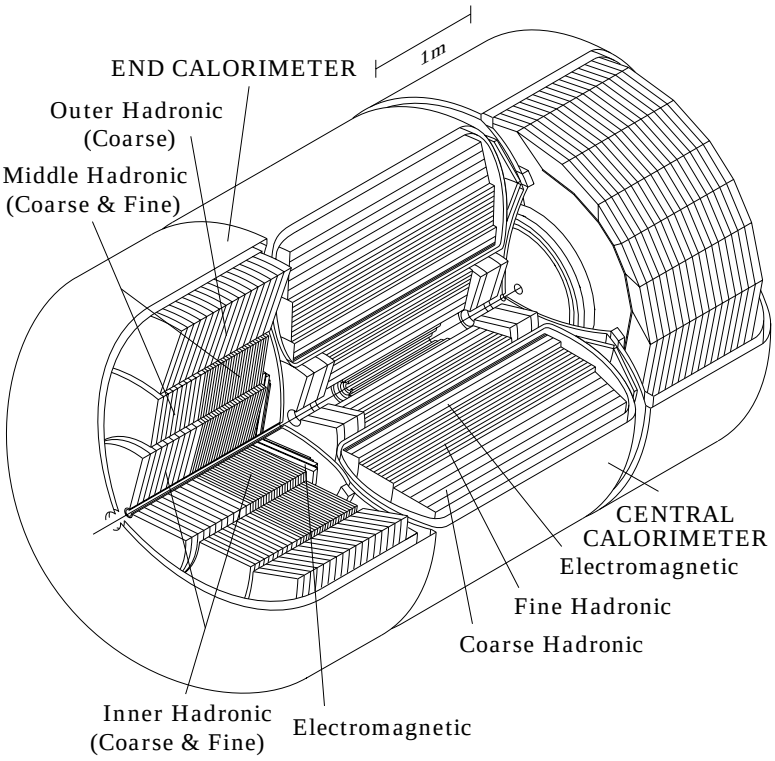

Figure 2.7: Isometric view of DØ calorimetry.

The DØ Calorimeter is highly modular, and finely segmented in the transverse and longitudinal shower directions. Three distinct types of modules are used

in the CC and EC: an electromagnetic section (EM) with thin uranium-238 absorber plates, a fine hadronic section (FH) with thicker uranium plates and a coarse hadronic section (CH) with thick copper or stainless steel plates.

Each module consists of a row of alternating absorber plates and signal readout boards, as shown in Figure 2.8. An electric field is established by grounding the absorber plate while applying a positive potential (typically 2.0-2.5 kV) to the resistive surfaces of the signal boards. The 2.3 mm gap was chosen to be large enough to observe a minimum ionizing particle in the LAr. The ionization electrons drift across the gap in ≈ 450 ns.

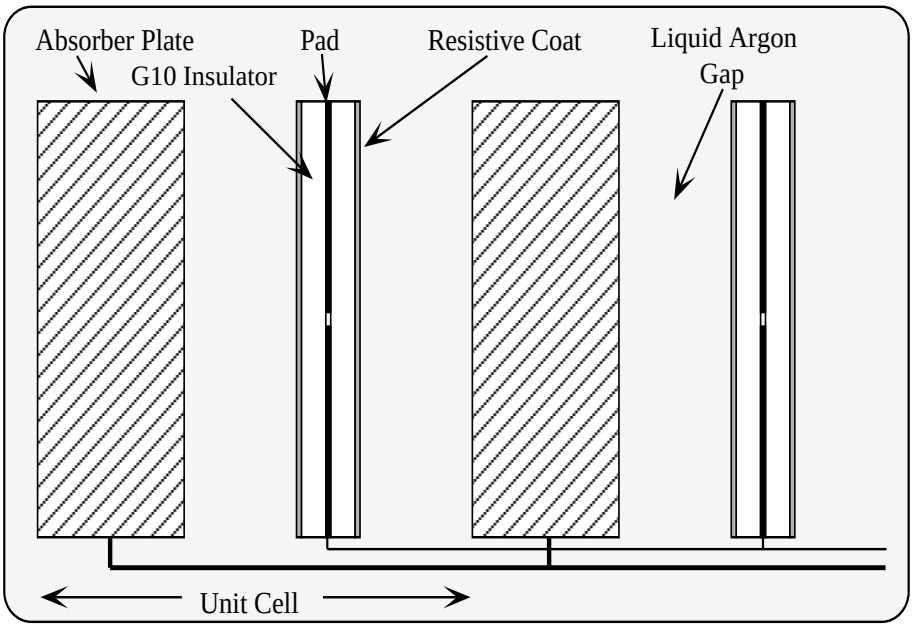

Figure 2.8: Schematic view of a DØ calorimeter cell.

The pattern and sizes of the readout cells were determined from considerations of shower sizes. The transverse dimensions of the readout cell were chosen to be similar to the transverse sizes of showers: $\sim$ 1–2 cm for EM showers and $\sim$ 10 cm for hadronic showers. Longitudinal segmentation within the EM, FH and CH layers helps in the distinction and separation of electrons from hadrons. The design was chosen to be "pseudo-projective": the centers of the cells lie on lines which project back to the center of the detector, but the cell boundaries are aligned perpendicular to the absorber plates. This is clearly illustrated in Figure 2.9.

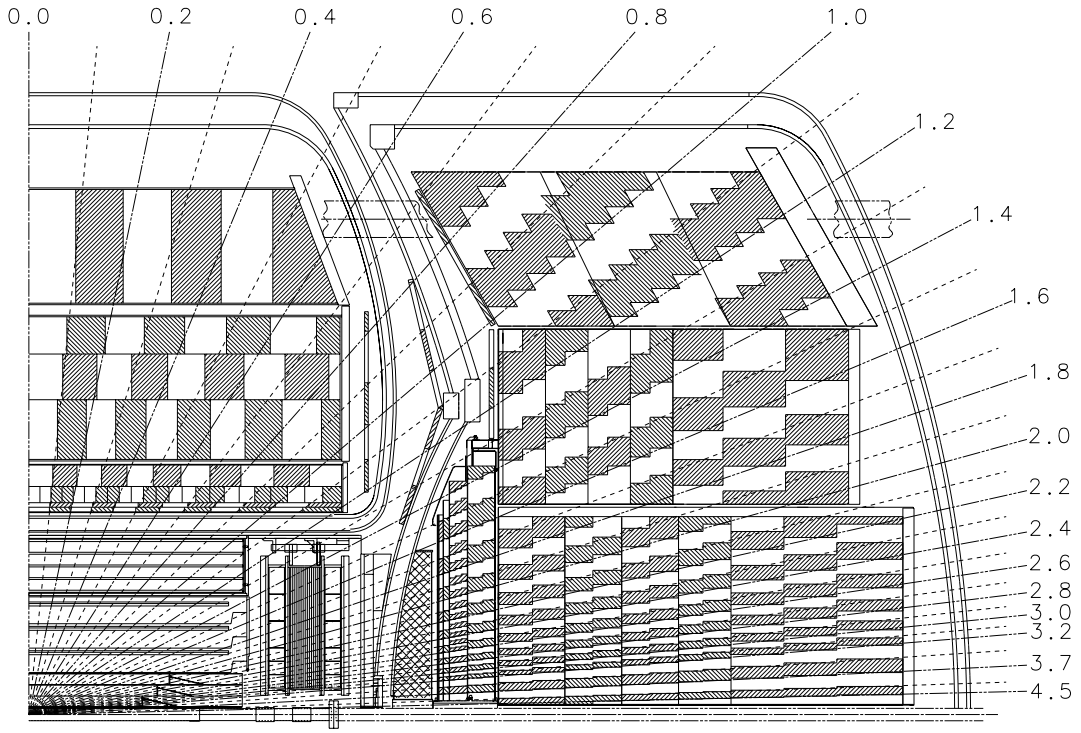

Figure 2.9: Side view of one quadrant of the calorimeter and central detector. The lines of constant pseudorapidity intervals are with respect to $z = 0$.

2.4.2 Central Calorimeter

The Central Calorimeter (CC) is composed of three cylindrical concentric shells . The inner shell consists of 32 electromagnetic (EM) modules, thick enough to contain most electromagnetic showers. The middle shell, made of 16 fine hadronic (FH) modules, measures showers of hadronic particles, while the outer layer, made of 16 coarse hadronic (CH) modules, measures any leakage out of the FH layer, thereby minimizing *punchthrough*, the energy flow out of the calorimeter and into the muon system.

Readout cells in the same η and ϕ are ganged together in depth to form a readout layer. The EM modules have four such layers which are 2, 2, 7, and 10 $X_\circ$ deep. The total depth of the EM layers is $20.5X_\circ$ or $0.76\lambda_A$. The FH modules are separated into three layers of depth 1.3, 1.0 and 0.9 λ_A. The CH layer is $3.2\lambda_A$ deep.

The transverse segmentation of the calorimeter is 0.1×0.1 in $\eta \times \phi$ space, except in the third EM layer (EM3). This layer, corresponding to the EM shower maximum, has its segmentation increased to 0.05×0.05 in $\eta \times \phi$ space in order to fully optimize the distinguishability between electron and hadronic showers. In addition, each concentric shell (EM, FH and CH) is rotated azimuthally, thus avoiding any continuous cracks.

The segmentation of the calorimeter is shown in Figure 2.10.

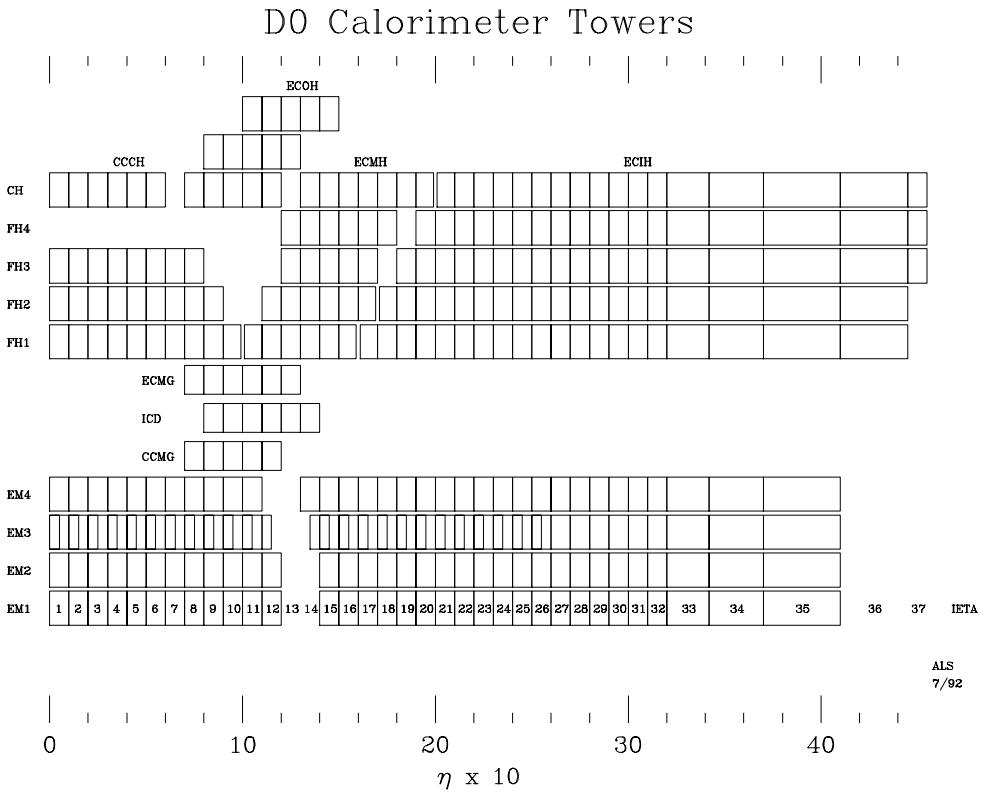

Figure 2.10: Longitudinal tower segmentation of the DØ calorimeter as a function of pseudorapidity.

2.4.3 Endcap Calorimeters

The two Endcap Calorimeters (EC) provide coverage on either side of the CC. Each endcap cryostat is divided into four sections: the electromagnetic (EM) module in front of the inner fine hadronic (IH), the middle hadronic (MH), and outer hadronic (OH) modules.

The EM module is a disk composed of four layers with an inner radius of 5.7 cm and an outer radius varying between 84 and 104 cm. The four layers are 0.3, 2.6, 7.9 and 9.3 $X_\circ$ in depth. The transverse segmentation is 0.1×0.1 in $\eta - \phi$ for

$|\eta_{det}| < 3.2$, after which it doubles. As in the CC, the segmentation in the third EM layer is finer. The segmentation in this layer is 0.05×0.05 for $|\eta_{det}| < 2.7$, 0.1×0.1 for $2.7 < |\eta_{det}| < 3.2$ and 0.2×0.2 for $|\eta_{det}| > 3.2$.

The inner hadronic modules are cylindrical with inner radius 3.93 cm and outer radius 86.4 cm. The fine hadronic portion has four layers, each $1.1\lambda_A$ thick. Alternate layers are rotated by 90° to avoid cracks. The coarse hadronic section has one layer with stainless steel plates of depth $4.1\lambda_A$.

The middle hadronic modules surround the inner hadronic modules. The fine hadronic portion consists of four layers with uranium plates of depth $0.9\lambda_A$ each and the coarse hadronic section consists of one layer with stainless steel plates $4.1\lambda_A$ deep.

The outer hadronic modules surround the middle hadronic layer. There are three coarse layers with stainless steel plates inclined at 60° to the beamline. The depth of each layer is $4.1\lambda_A$ deep.

The the transverse segmentation of the inner hadronic layers is 0.1×0.1 for $|\eta_{det}| < 3.2$ and 0.2×0.2 otherwise. Beyond the EM coverage ($|\eta_{det}| > 3.8$) the segmentation is 0.4×0.2. The segmentation for the middle and outer hadronic layers is 0.1×0.1.

The reader is referred to Figures 2.9 and 2.10 for a layout of the calorimeter modules.

2.4.4 Intercryostat Detectors and Massless Gaps

The region of crossover between the CC and EC ($0.8 \leq |\eta_{det}| \leq 1.4$) contains a large amount of uninstrumented material. To correct for energy deposited in this uninstrumented region, two scintillation arrays called intercryosts detectors (ICD) were mounted on the front surface of each EC. Each consists of 384 tiles of size $\Delta\phi = \Delta\eta = 0.2$. In addition, rings of readout boards, called massless gaps, were mounted on the endplates of the CC FH modules and the EC MH and OH modules to record any ionization caused by the cryostat walls acting as absorbers.

2.4.5 Calorimeter Readout

Signals from the calorimeter modules are readout in several stages. They are first brought to feedthrough boards in the cryostat walls to charge-sensitive preamplifiers and then via twisted pair cable to baseline subtracter (BLS) shaping and sampling circuits. The signals are integrated (430 ns) and differentiated (33 μs). The signals are sampled just before and 2.2 μs after a beam-crossing. The difference is proportional to the collected charge. The signals are then sent to the moving counting house where ADC's digitize each signal into 384 channels. Channels which fall below a threshold can be suppressed from further readout to reduce bandwidth. A portion of the signal is sampled at the BLS input and added into $\Delta\phi = \Delta\eta = 0.2$ trigger towers for use in event selection.

2.4.6 Calorimeter Performance

The energy resolution of electrons and pions with energies between 10 and 150 GeV were measured using Endcap Calorimeter electromagnetic and fine hadronic modules in test beam conditions. The measured resolutions can be approximated by:

$$\frac{\sigma(\mathrm{E})}{\mathrm{E}} \sim \frac{16\%}{\sqrt{\mathrm{E}}} \text{ for electrons}$$

$$\frac{\sigma(\mathrm{E})}{\mathrm{E}} \sim \frac{41\%}{\sqrt{\mathrm{E}}} \text{ for pions.}$$

These approximations show the expected $E^{-\frac{1}{2}}$ response due to the statistical fluctuations in the showers, but do not take into account noise and calibration uncertainties which must be measured *in situ*. The resolution for single pions is a lower limit on the resolution for jets which are composed of many hadrons.

The e/h ratio was measured to fall from 1.11 at 10 GeV to 1.04 at 150 GeV after accounting for out-of-time event pile-up, early showering and energy deposition outside the $\eta - \phi$ region used to sum energies.

The calorimeter position resolution is important in matching tracks with calorimeter clusters for the rejection of backgrounds to electrons. The position resolution was found using the energy weighted position of the shower as measured by EM layer 3 for 100 GeV electrons. The resolution varied between 0.8 and 1.2 mm depending on entry angle and varied with energy as $E^{\frac{1}{2}}$.

2.5 Muon Tracking

Muons do not interact via the strong force and are too massive to lose substantial energy via Bremsstrahlung. With a long lifetime ($\tau = 2.2\mu$s), they can traverse the entire thickness of the detector without decaying. In traversing the calorimeter they leave a minimum ionizing particle trace.

The muon tracking system uses proportional drift tubes (PDT) and five magnetized iron toroidal magnets to measure the momenta of passing muons [57]. The first layer of PDT's is placed inside the magnets and two layers are placed outside the magnets to measure the bend in a muon's trajectory and thus its momentum. The muon system is subdivided into two sections, the wide angle muon system (WAMUS) and the small angle muon system (SAMUS), which are described below.

2.5.1 WAMUS

The WAMUS contains rectangular PDT's which have one sense wire per drift cell. The WAMUS region extends to $|\eta_{det}| \leq 1.7$. The three layers, A, B, and C (shown in Figure 2.11), are composed of 4, 3, and 3 planes of drift tubes respectively. The readout electronics measure the arrival times of pulses as well as the difference of arrival times at the end of each cell. This time difference is used to give a rough determination of the position along the wire where a hit occurred. A more precise measurement of the hit position can be made using vernier cathode

pads in each tube. By measuring the division of charge between the inner and outer pad, a position measurement with resolution of about 3 mm can be made along the direction of the wire. The position measurement perpendicular to the sense wire has an accuracy of about 0.53 mm.

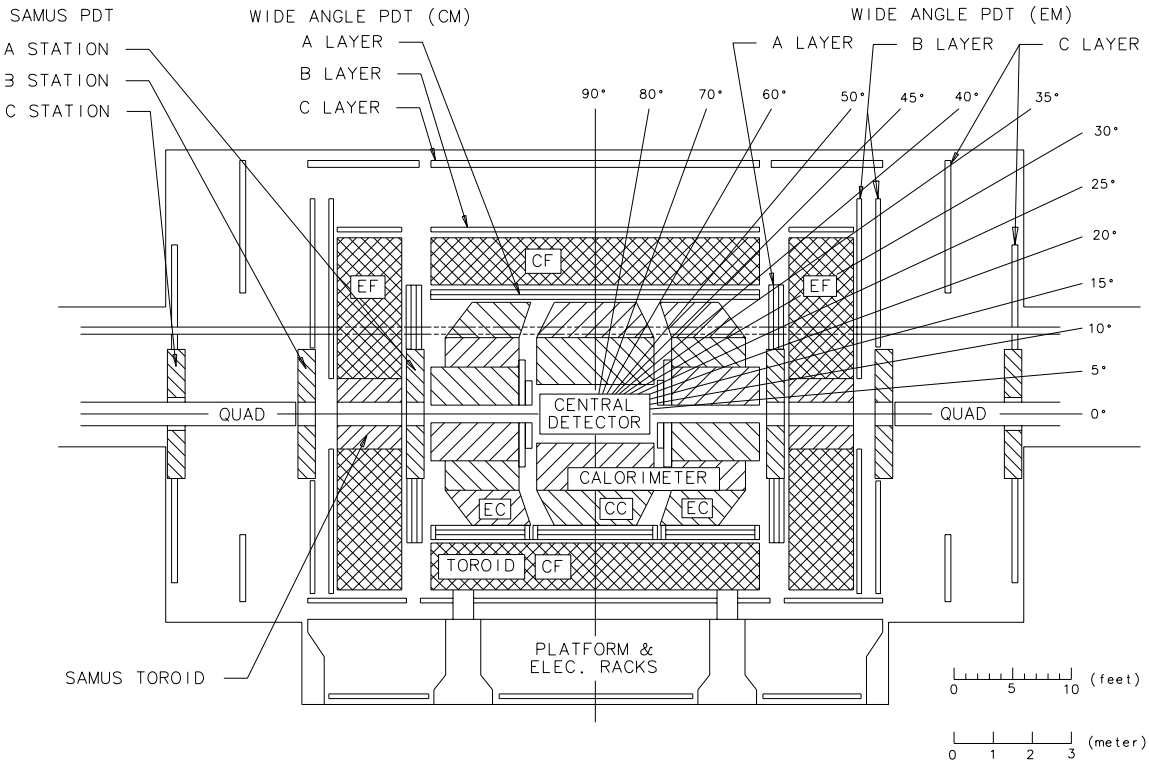

Figure 2.11: Side view of the DØ muon system.

The momentum of the muon is determined by reconstructing the trajectory from hits in the three layers. The momentum resolution is dependent on the accuracy of the trajectory measurement and multiple scattering in the magnets, which smears the direction of the muon as it exits the magnets.

2.5.2 SAMUS

The SAMUS covers a pseudorapidity range of $1.7 \leq |\eta_{det}| \leq 3.6$. Due to the higher flux of particles in the forward region the SAMUS uses smaller drift tubes. The system consists of three planes of drift tubes. Each plane is composed of two subplanes offset by half a tube diameter. The drift tubes are made of stainless steel tubes with a 3 cm diameter, each with a single sense wire.

2.6 Trigger and Data Acquisition

During the 92-96 data taking run, the Tevatron was operated with a 3.5 μs interval between bunch crossings. At the luminosities obtained, this resulted in one or more interactions per crossing. It would be impossible to record every event at this rate ($\sim$ 286 Hz). The solution is to record only events of interest by "triggering" on event characteristics of interest.

A schematic overview of the DØ trigger system is shown in Figure 2.12. It consists of three different levels, each with increasingly sophisticated event characterization. The Level 0 trigger uses a set of scintillation counters to indicate the presence of an inelastic collision. It reduces the rate to about 150–200 kHz. The Level 1 trigger is a collection of hardware triggers which is software programmable. Most trigger decisions are made within the 3.5 μs interval between beam crossings. However, some triggers, called Level 1.5 , may require additional time. The event

rate out of Level 1 (and Level 1.5) is roughly 100 Hz. Events that pass the Level 1 trigger are fully digitized, and the data is sent to a farm of microprocessors, which make up the Level 2 trigger. The Level 2 trigger is software based and uses a simplified and fast version of the reconstruction program to reduce the rate of events to 2 Hz – the rate dictated by the speed of magnetic recording media.

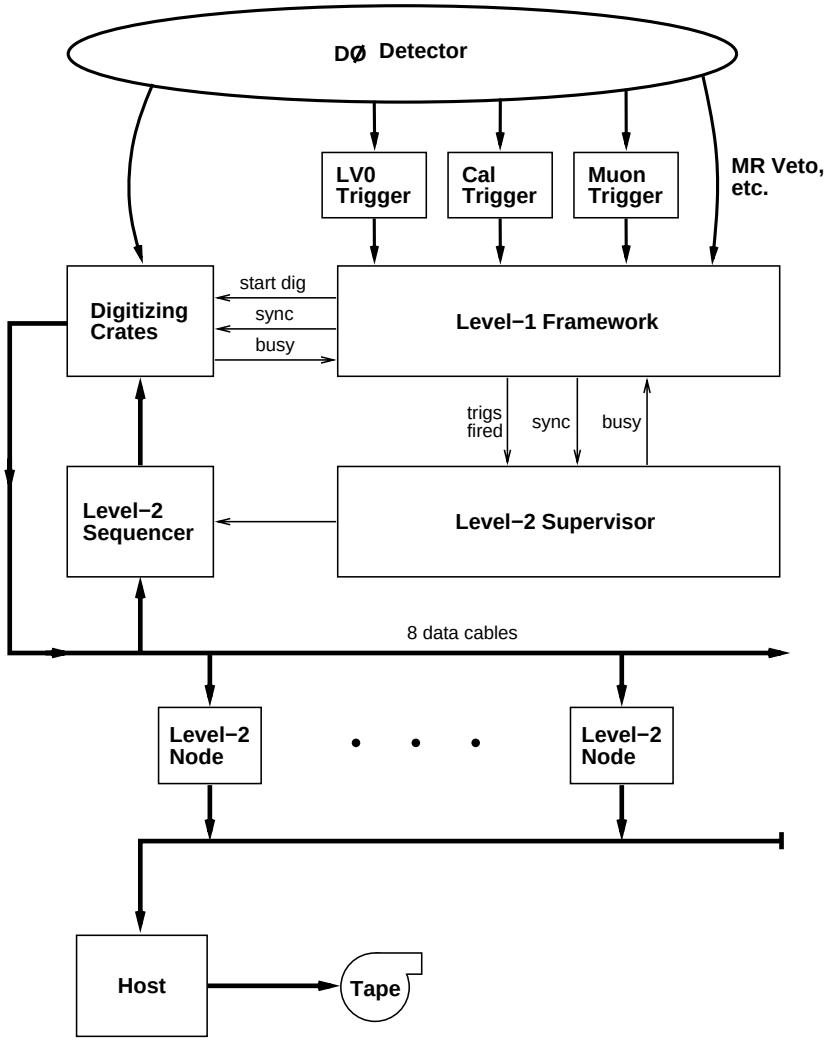

Figure 2.12: Schematic of data acquisition at DØ.

2.6.1 Level 0

The Level 0 trigger registers the presence of inelastic collisions and serves as the luminosity monitor for the experiment. It consists of two hodoscopes of scintillation counters mounted on the front surfaces of the endcap calorimeters. Coincident signals in both hodoscopes signals the presence of an inelastic collision. The Level 0 trigger also provides information of the z-coordinate of the interaction from timing information. The luminosity is obtained from measuring the rate of inelastic collisions with $|z_{vtx}| < 100$ cm. This number is corrected for the acceptance of the Level 0 system modeled in Monte Carlo studies and then multiplied by the world average for the total inelastic cross section [58]. The total error on the luminosity using this method is 5.4%.

2.6.2 Beam Vetoes

As mentioned earlier, the Main Ring beam pipe passes through the upper hadronic section of the Calorimeter. While collisions are occurring in the Tevatron, the Main Ring is still in operation for $\bar{p}$ production. During injection of protons into the Main Ring and the transition to 150 GeV, losses are seen in the DØ detector. Losses are also seen during the passage of the proton beam during a Tevatron beam crossing. This causes spurious hits in the coarse hadronic calorimeter (affecting the $\not\!\!E_T$ measurement) and in the muon system.

To account for these conditions, two trigger terms for the Level 1 framework were developed to veto events occurring during Main Ring losses [59]. Specifically, events are rejected which occur within a 400 ms window after Main Ring proton injection (MRBS_LOSS) and within a 1.6 μs gate which occurs every 21μs and is consistent with the passage of Main Ring protons through the DØ detector (MICROBLANK). The beam veto which imposes both conditions is known as "GOOD_BEAM" since good beam conditions are required. The total dead time incurred by the GOOD_BEAM veto is about 25%.

2.6.3 Level 1

The Level 1 trigger [60] was designed to minimize the decision time as much as possible so that no dead time was incurred for trigger decisions. The Level 1 framework gathers digital information from each Level 1 trigger device as well as various vetoes. The trigger decision is made by a two-dimensional AND-OR network. The network consists of 256 inputs and has 32 outputs which correspond to the Level 1 triggers. These triggers are programmable, allowing the thresholds and the pattern of input terms which fire the trigger to be modified. Additionally, a "prescale" can be specified for triggers with high rates.

The Level 1 calorimeter trigger uses separate EM and fine hadronic trigger towers (both with $\Delta\eta\times\Delta\phi = 0.2\times0.2$ wide) as inputs to the AND-OR network. The energy in the trigger towers is weighted by the trigger tower polar angle with respect

to $z = 0$ to give the transverse energy. The transverse energy is then corrected using a z-vertex determined from the initial timing information from Level-0, if available. The transverse energy of each tower is split into x- and y- components and the components are summed over the entire calorimeter to determine $\not\!\!E_T$. The energies of each tower as well as the total tower energy (EM+FH) and global sums are used as inputs into the AND-OR network, where they are compared to the programmed thresholds.

For this study, the trigger used required two EM towers with $E_T > 7$ GeV (the so-called EM_2_MED trigger). No events under this trigger were discarded for the purposes of bandwidth management, i.e. this trigger was not prescaled during data collection.

2.6.4 Level 1.5

The Level 1.5 trigger uses digital signal processors to refine and confirm the Level 1 trigger decision [61]. The Level 1.5 calorimeter trigger improves energy resolution by examining the energy in towers neighboring the Level 1 EM towers. Additionally, energy sums are computed from adjacent hadronic towers, and the ratio $E_{\rm EM}/E$ is used for further background rejection. For this analysis, events passing the EM_2_MED Level 1 trigger were required to have at least one Level 1.5 electron candidate with $E_T > 12$ GeV and $E_{\rm EM}/E > 0.85$.

2.6.5 Level 2

The Level 2 system functions as the next layer of event filtering and the data acquisition system with the goal of reducing the rate of events recorded to tape to 2 Hz. The Level 2 system consists of a cluster of 48 dedicated CPU nodes connected to 8 high speed data cables for reading out the event information from the digitization crates. If an event passes a Level 1(1.5) trigger, the Level 2 supervisor node finds a free Level 2 node and tells it to start reading out the event information from over the eight data cables, each corresponding to one of the eight detector sections: VTX, TRD, CDC, FDC, the north and south halves of the calorimeter, muon chambers, and Level 0 and Level 1 triggers. If an event passes a Level 2 filter it is passed to the host computer for recording on magnetic media.

The Level 2 nodes run an event-filtering program which is built around a series of filter tools. Among the tools are those for jets, calorimeter EM clusters, track association with calorimeter clusters, $\sum E_T$ and $\not\!\!E_T$. Specific combinations and orders of these tools are combined into "scripts". Each script is associated with one of the 32 Level 1 triggers. The script can generate several Level 2 filters for a given Level 1 trigger based on different E_T thresholds or other features of the event like energy isolation or $\not\!\!E_T$. There are 128 Level 2 filters available.

All events in this analysis are required to satisfy the EM2_EIS2_HI Level 2 software filter. This filter required two Level 2 electron candidates with $E_T >$

20 GeV which satisfied electron shower shape and isolation cuts.

2.7 Online Cluster

The DØ online cluster [41] is composed of three VAX minicomputers. They are dedicated to recording events on disk and spooling them to 8mm tape and to hardware monitoring. The cluster also serves as the human interface to the detector systems. In this role it is responsible for control of data taking, downloading programmable parameters, and displaying of data from the detector which includes calibrations, monitoring information and alarms.

2.8 Offline Data Processing

The data is stored on high density 8mm magnetic tapes. The events are reconstructed by the full event reconstruction program (described in the next chapter) by a farm of Silicon Graphics and IBM computers at the Fermilab Central Computing Facility. Two types of files are produced by the reconstruction program. STA files contain the raw data plus the results of the reconstruction and contain approximately 600 kilobytes per event. DST files contain only the results of the reconstruction such as calorimeter clusters and reconstructed tracks as well as parameters for electrons, jets, $\not\!\!E_T$ *etc.* The DST event size is typically 30 kilobytes per event. The size of the 93-95 data set brought about the need for an even smaller

event format called μDST which contained only the most essential information for analysis. The STA files are kept on tape, and the DST files are kept on disk on a file server cluster. From here the data are filtered into separate streams, depending on high level event characteristics, and are stored in μDST format for further analysis.

Chapter 3

Event Reconstruction and Particle Identification

The information recorded by the DØ detector is in the form of digital signals: pulse heights, widths and times. These signals are converted into numbers useful to an analysis by a standard reconstruction program called DØRECO, which converts the signals into tracks and calorimeter clusters which are then interpreted as jets, electrons, photons, muons and neutrinos ($\not\!\!E_T$). A brief description of the steps taken in event reconstruction are described below. Following that is a description of the variables used for identifying electrons.

3.1 Track Reconstruction

Tracks in the Central Detector are reconstructed in four stages: hit finding, segment finding, segment matching, and global track fitting. The arrival time and drift time of a pulse are used to fix the location of a hit, and the integral of a pulse is used to determine charge deposition. All pulses are converted to hits, and track finding proceeds. Within each layer hits are grouped together into a segment using roads in the r–ϕ plane. If enough hits are found within the road which fit to a line with small enough variation, a segment is formed. If three of four segments fit a straight line, a track is formed.

The direction of a track is specified by a reference point, called the track centroid, and two angles. The track centroid is corrected for biases in z-coordinate using cosmic muons and collider muons [64, 65]. Tracks in the forward region are only reconstructed in a wide road defined by a calorimeter cluster and the event vertex. In the central regions, all hits are considered for track reconstruction. Further details regarding central detector hit finding and tracking can be found in References [51, 52, 53, 54].

3.2 Vertex Finding

The next step in the event reconstruction process is to determine the number and z-position of event vertices. This is done by creating a histogram of CDC

track z-intercepts (see Figure 3.1). The primary vertex is identified as the peak with the largest number of associated tracks. All high-E_T objects are assumed to arise from the primary vertex. Any other peaks are identified as secondary vertices resulting from minimum bias interactions. The z-resolution attained is 1–2 cm, with multiple vertices resolvable down to 7 cm. In a high-luminosity environment where multiple interactions occur, the high-E_T interaction of interest may have a lower number of charged tracks than the other minimum bias interactions in the event. For luminosities typical during the 93-96 data taking runs ($\sim 7 \cdot 10^{30}$ cm^{-2}s^{-1}), 70% of all events contained more than one interaction. A method of vertex determination which relies on the information from high-E_T objects is preferred. A discussion of one such method which uses electrons will be discussed in Section 3.10.2.

The (x,y) coordinate of the vertex was not recorded. Instead the (x,y) coordinate of the beam spot was recorded for each store. A slight offset in the beam had no noticeable effect on high-E_T object events.

3.3 Calorimeter Hit Finding

Only cells in the calorimeter with energy above the noise threshold are examined. Pulse heights are converted into energy deposited using calibration constants determined in test beam studies.

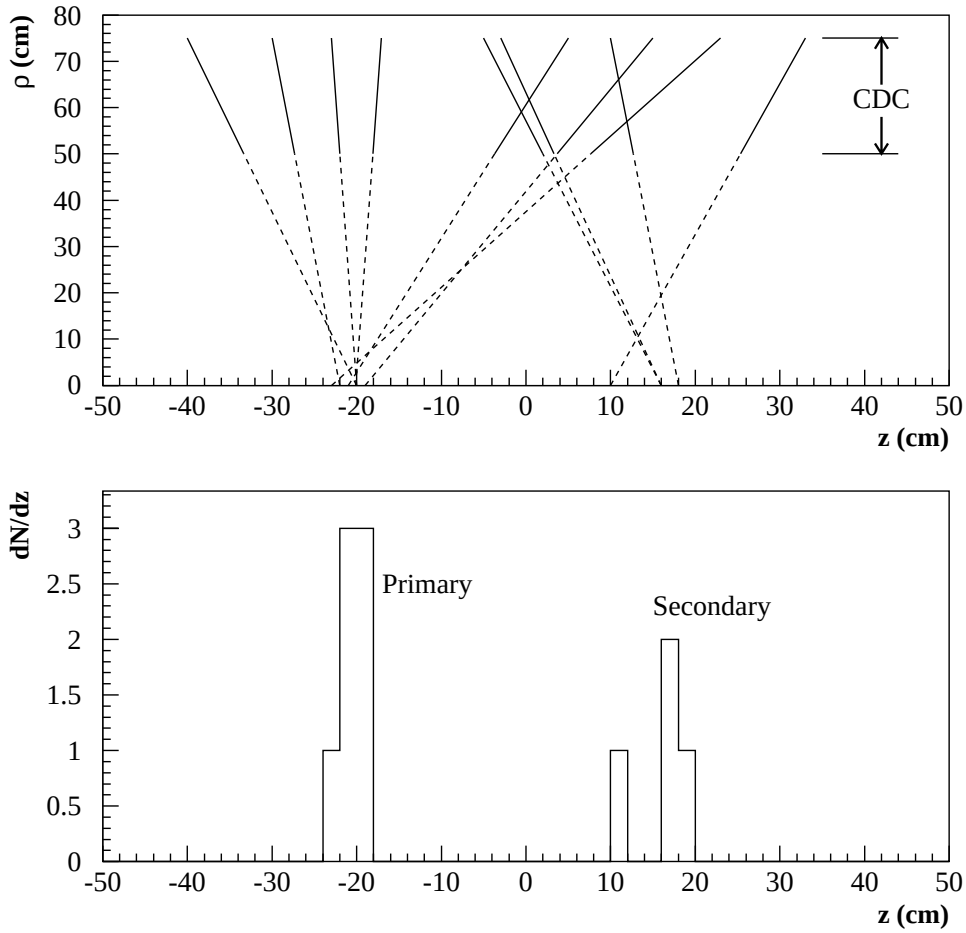

Figure 3.1: Vertex determination by histogram method. Top: projections of tracks to the beamline. (View is integrated over all azimuthal angles ϕ.) Bottom: Resulting distribution of z-intercepts from which vertices are determined.

Hit cells are grouped into towers in $\eta - \phi$ and summed to calculate tower energies. The total energy and the electromagnetic energy for each tower is calculated. The electromagnetic energy is the sum of the energy in electromagnetic layers EM1, EM2, EM4, the 2×2 cells in EM3, plus the first layer of the fine hadronic section

FH1. These towers form the basis for jet and electron/photon clustering.

3.4 Missing Energy

The presence of a neutrino or any other minimally interacting particle is inferred by an imbalance of energy in the event. Because the energy of the spectator quarks, which escape down the beam pipe, is not recorded by the detector, only the transverse component of this energy imbalance can be fully reconstructed.

To determine this transverse energy imbalance all calorimeter cell energies are treated as vectors using the primary event vertex and the cell center to determine vector direction and cell energy to determine vector magnitude. Then the transverse components of vectors are summed. The missing transverse energy vector exactly balances this vector sum. Three versions of missing energy are calculated. The first version is calculated from calorimeter cells only. The second version corrects for energy deposited in the ICD cells. The third version subtracts out the momentum of any muons in the event.

3.5 Jet Reconstruction

Hadrons produce a shower of secondary hadrons, called a jet, in the calorimeter. The most common definition of a jet at DØ uses a cone to define which cells will be summed to give the original hadron energy. For this analysis a cone size of

$R = \sqrt{\Delta\eta^2 + \Delta\phi^2} = 0.5$ was used.

The cone algorithm begins by picking towers with the highest E_T as cluster seeds. The cells within $\eta \times \phi = 0.3 \times 0.3$ of the seed tower are summed to form pre-clusters. All seed towers within the precluster are dropped from the seed tower list. The next highest E_T seed tower is used to define a new precluster. This process is continued until all towers are used. The energies of cells within the cone centered on each precluster are summed using E_T weighting to determine a shower centroid. The jet is reclustered using the newly calculated centroid to define the cone until the direction of the shower centroid stabilizes. A cone must contain at least 8 GeV of energy to be identified as a jet. If two jets overlap, they are merged if the energy of the overlapping cells is more than 50% of the energy of the lower E_T jet. Otherwise the energy of the overlapping cells are assigned to the jet with the closer shower centroid. This merging/splitting process is continued until all preclusters are assigned to a jet. The kinematic properties of the jet are calculated by summing tower energies.

3.6 Electron–Photon Reconstruction

Electrons and photons produce very similar showers which deposit most of their energy in the electromagnetic layers of the calorimeter. These electromagnetic showers are reconstructed using the same algorithm. The reconstruction of electrons

and photons uses the "nearest neighbor" (NN) algorithm [67, 68] which is based on total (not transverse) tower energy.

Starting with a seed tower with the highest energy, the NN algorithm forms a cluster by summing all towers which have an energy greater than 50 MeV within a 3×3 grid centered on the seed tower. Cells are not shared between clusters.

A cluster is identified as an electron/photon if the cluster passes the following criteria [63]:

- The total cluster energy $E_{total} > 1.5$ GeV;
- The total cluster transverse energy $E_T > 1.5$ GeV;
- The total electromagnetic fraction E_{EM}/E_{total} >90% ;
- The tower with the highest energy of the cluster must contain > 40% of the energy.

The kinematic properties of the cluster are calculated by summing individual cell energies. The shower centroid is calculated using the log of the energies in the cells in EM3 [69, 70, 71].

Electrons are distinguished from photons by requiring a CDC track in a $\eta \times \phi = 0.1 \times 0.1$ road defined by the shower centroid and the primary vertex. In a high luminosity environment, the primary vertex can be misidentified making this distinction problematic. A more robust method is described later.

3.7 Electron Identification

The particle identification performed by the reconstruction program is rudimentary and serves as a starting point for further refinement of particle identification. Additional identification parameters are needed for distinguishing the signal from the background in an efficient manner. The particle identification parameters were developed using Monte Carlo, test beam and real data. The identification parameters used to identify electrons in this analysis are described below.

3.7.1 Electromagnetic Shower Shape Analysis

The shower profile of an electron can be quantified in terms of the energy deposited in each layer of the calorimeter. These quantities will be correlated, *i.e.* a shower which deposits more of its energy in the first layer will deposit less of its energy in the last layer and vice versa.

To simultaneously quantify the energy deposited in each layer and the correlations with energy deposited in other layers a covariance matrix (M) based on 41 observables was used [72, 73, 74]. The matrix elements were computed from reference samples of Monte Carlo electrons with energies between 10 GeV and 150 GeV. The matrix elements are defined as:

$$M_{i,j} = \frac{1}{N}\sum_{n=1}^{N}(x_i^n - \bar{x}_i)(x_j^n - \bar{x}_j),$$

where x_i^n is the value of the i^{th} observable for the n^{th} electron, $\bar{x}_i$ is the mean of the

i^{th} observable and N is the number of electrons. The observables are the fractional energies in layers 1, 2 and 4 of the EM calorimeter, and the fractional energy in each cell of a 6×6 grid of cells in EM layer 3 centered on the most energetic tower in the EM cluster. The log of the cluster energy as well as the entry angle are the last two observables.

For a shower, with the observables x_i', the covariance parameter is given by:

$$\chi^2 = \sum_{i,j=1}^{41} (x_i' - \bar{x}_i) H_{i,j} (x_j' - \bar{x}_j)$$

where $H = M^{-1}$. This gives a measure of how consistent a shower's profile is with that expected from an electromagnetic shower.

3.7.2 Shower Isolation

Electrons originating from the decays of W and Z bosons tend to be isolated since they are not produced in association with other nearby particles. In contrast, the production of π^0 and η particles (which can decay to two photons and produce an electromagnetic shower) or the production of electrons from heavy quark decays is usually in association with the production of nearby hadronic particles. A cut on the isolation of an electromagnetic cluster would select out electrons of interest while reducing backgrounds.

Electromagnetic showers are usually contained in a cone of radius $R = \sqrt{\Delta\eta^2 + \Delta\phi^2} < 0.2$ with axis along the shower centroid. The isolation fraction

is defined by

$$I = \frac{E_{tot}(0.4) - E_{EM}(0.2)}{E_{EM}(0.2)}$$

where $E_{tot}(0.4)$ is the total energy within a cone of radius $R = 0.4$ and $E_{EM}(0.2)$ is the energy in the EM layers within a cone of radius $R = 0.2$.

3.7.3 Track–Cluster Matching

The tracking roads which define an electron are quite loose. This allows π^0 and η particles which are produced with a nearby low E_T charged hadron to mimic the signature of an electron. The tracks produced by genuine electrons will be closely aligned with the shower centroid.

The track match significance variable quantifies how well the projection of a track into the EM layer 3 matches the shower center in EM layer 3.

Track match significance is defined as:

$$S_{\text{track}} = \sqrt{\frac{(\Delta\phi)^2}{\sigma^2_{\Delta\phi}} + \frac{(\Delta z)^2}{\sigma^2_{\Delta z}}}$$

where $\Delta\phi$ is the azimuthal mismatch and Δz is the mismatch along the beam direction of the cluster-track projection, respectively, and $\sigma_{\Delta\phi}$ and $\sigma_{\Delta z}$ are the resolutions. These quantities are plotted in Figure 3.2 along with a Gaussian fit showing the resolution for tracks from $Z \to ee$ events.

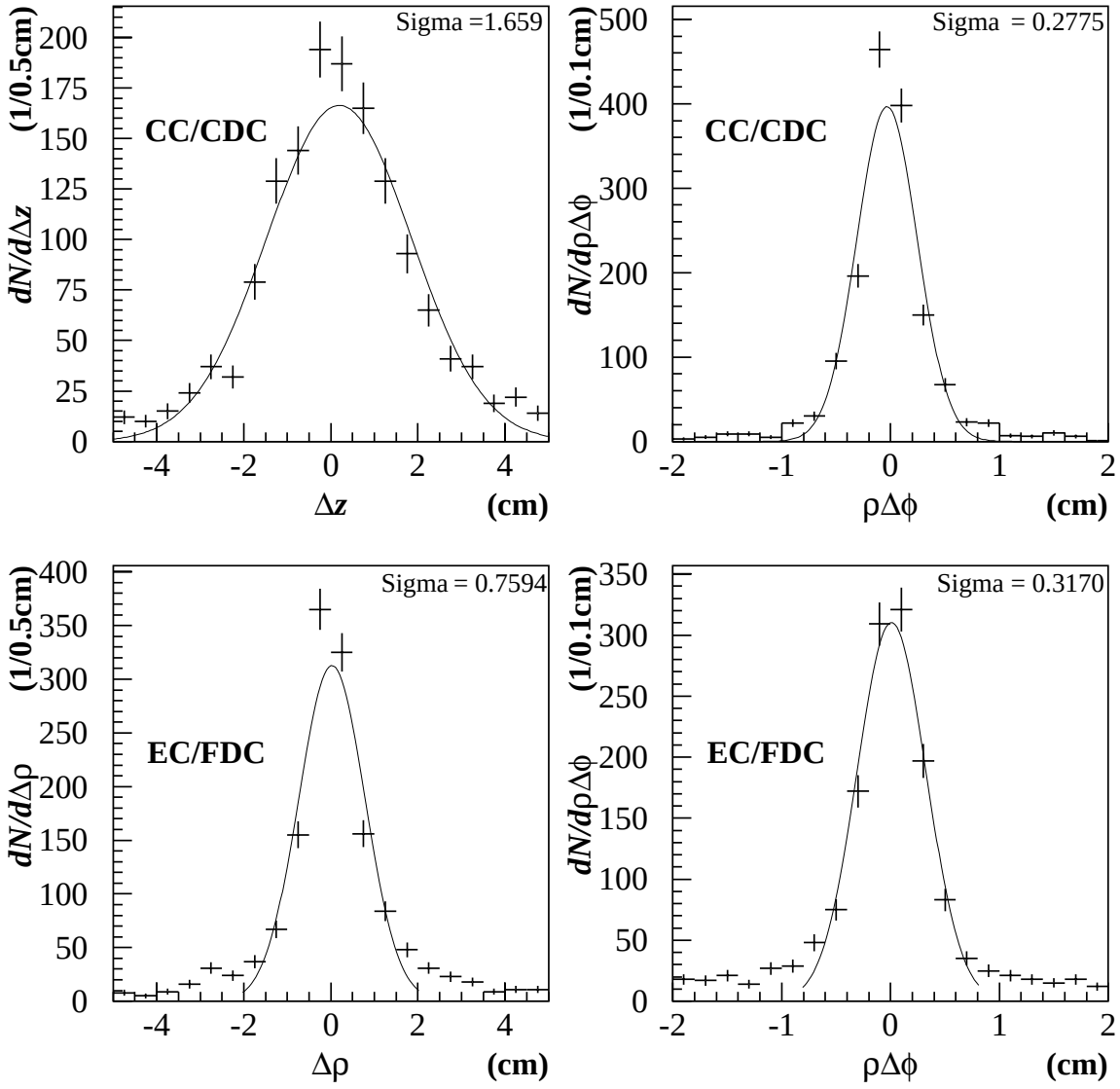

Figure 3.2: Differences in cluster centroid and EM3 projected track positions for electrons from $Z \rightarrow ee$ candidates with $S_{track} < 30$ [66].

3.7.4 Hit Counting Techniques

To increase the overall detection efficiency for $WZ \rightarrow l\nu ee$ events, it is necessary to relax the tracking requirement on one or two of the electrons, i.e., accept

events with electrons and "photons". However, this leads to increased backgrounds from events containing photons. The situation can be improved if a more efficient method were available for distinguishing electrons from photons, and it is for this reason that a "hit counting" technique is used in this analysis.

The hit counting technique employed here uses roads defined by $\Delta\phi = \pm 7.5$ milliradians in the central region and $\Delta\phi = \pm 15$ milliradians in the forward region.[1] Within the road, the number of sense wire hits with drift times compatible with ionization originating from within the road were counted. Figure 3.3 shows the number of hits $N_{\rm hit}$ within the electron road for $Z \rightarrow ee$ candidates. For central electrons, the distribution peaks near 28 hits, corresponding to the situation in which each of the 28 available sense wires has recorded a signal. The dashed line indicates the response expected from (non-converting) photons. This distribution was obtained by performing the hit counting analysis in roads offset in ϕ from each of the two electron candidates in $Z \rightarrow ee$ data. Since no activity is expected in this part of the central detector, the environment should be similar to that produced by a non-converting photon. As expected, the number of hits for such "emulated photons" peaks at zero. The long tail is due to unassociated tracks and hits ("random overlaps") which are not necessarily coincident with the shower in the polar (rz view) direction. A cut at $N_{\rm hit} = 20$ distinguishes the two populations well. Similarly, a cut at $N_{\rm hit} = 36$ is used to discriminate between photons and electrons in the forward

[1] Only xy view (ϕ) CDC hit information was available for this analysis; no delay line (z) information was available in the μDST sample.

region. The high multiplicity environment at forward angles makes this distinction less pronounced than in the forward region.

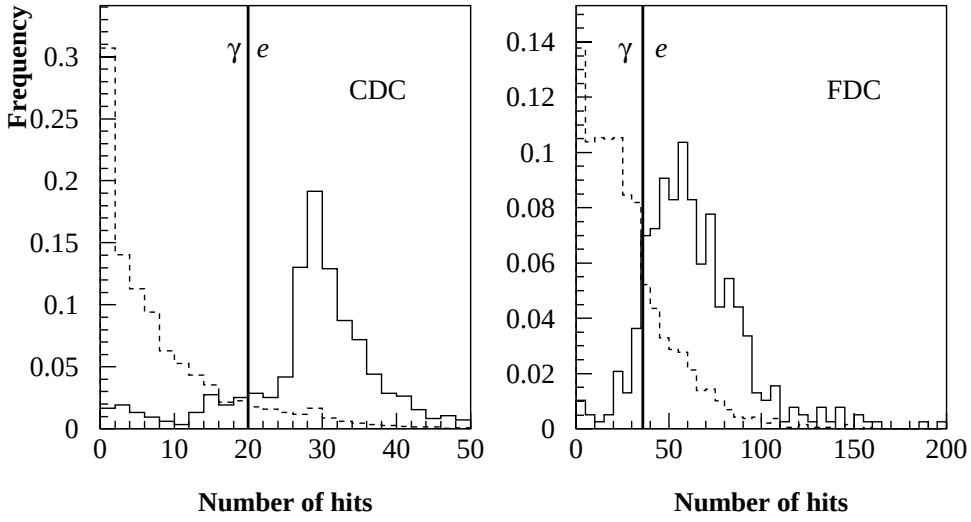

Figure 3.3: Number of drift chamber hits for both $Z \rightarrow ee$ candidates (solid) for both the central and forward regions. The dashed line indicates the number of random hits in emulated photon roads.

3.8 Muon Reconstruction

The reconstruction of muon tracks begins by turning the timing information of a hit into a hit location. Tracks are formed from hits in B and C layer outside the toroid and hits in the A layer inside the toroid. A trajectory is formed by matching a BC layer track with an A layer track that matches it closely in the mid toroid

plane.

The momentum is determined by the angle between the A layer and BC layer track, the field strength (2 T) and corrections for energy losses in the calorimeter. A global fit for the best measured momentum is performed using the muon system tracks, the primary interaction vertex, energy deposition in the calorimeter and a track from the CDC(FDC) if on is present. Addition corrections are made for the effects of multiple scattering in the calorimeter and the magnets.

3.9 Muon Identification

Offline identification criteria must be made to select real muons from WZ events and to reject combinatoric and cosmic ray backgrounds. The following properties of reconstructed muon candidates are used for this purpose:

- Muon Fit Quality (IFW4):

  The muon reconstruction makes a number of cuts on the number of PDT modules hit, the hit residuals, and the track impact parameters. IFW4 is the number of cuts failed by the candidate muon. Therefore a perfect track would have IFW4=0.

- Hadronic Fraction (HFRAC):

A moun will deposit energy as it passes through the calorimeter forming a track. HFRAC is the fraction of calorimeter cells along this track in the hadronic layers which have energy consistent with a minimum ionizing particle.

- xy Impact Parameter:

  A cosmic ray muon is not likely to pass near the beam position. The xy impact parameter is found by projecting a track into the xy plane, extrapolating the track to the center of the detector and measuring the distance from the primary vertex. Muons arising from the primary vertex will have a small impact parameter.

- Floating time offset (t_0^{float}):

  The time of the hits in the track are allowed to float in the fit. The difference between the best-fit time and the beam crossing is calculated. Muons arising from the primary vertex will have a small difference while out-of-time cosmic ray muons will have a large difference.

- Path length in the magnet ($\int \vec{B} \cdot \vec{dl}$):

  $\int \vec{B} \cdot \vec{dl}$ measures the integrated magnetic field a muon traverses as it passes through the iron toroid magnet. In order to measure the muon momentum accurately, the muon must pass though a minimum field integral.

- Muon isolation ($\Delta R(\mu, jet)$):

The muons of interest in this analysis result from W decays and are typically well isolated from nearby particles. Muons from the semileptonic decay of bottom and charm quarks are produced in association with hadronic particles and are a background for this analysis. A cut in the separation of a muon from nearby energetic jets ($E_T > 10$ GeV) ensures that only isolated muon are selected.

3.10 Post-RECO Corrections

3.10.1 Jet Corrections

Several corrections are made to jets after event reconstruction so that the jet energy more closely approaches that of the originating hadron. These include corrections for out-of-cone energy, underlying event, and low energy particles.

The energy of secondary particles may fall outside the cone used for reconstructing the jet. The energy lost depends on the cone size used as well as the region of the detector where the shower develops.

Low energy particles with energy of order 2 GeV produce a non-linear response in the calorimeter cells and simple summing of cells does not account for all energy.

Energy from the spectator quarks (those which did not interact) may be deposited in the calorimeter and must be subtracted from the measured energy.

To approximate the energy of the parent particle a correction factor is needed. This effect was taken into account by performing a study to determine the correction factor for jet energy as a function of jet energy and detector region [75]. This was studied by examining the E_T balance of events containing an isolated electromagnetic cluster (due to a photon or a jet which fragmented mostly into neutral hadrons) and one jet, but no other objects. Any $\not\!\!E_T$ in the event could be attributed to the mismeasurement of the hadronic jet because there is no neutrino present. This correction was coded into a standard package called CAFIX, short for calorimeter fix.

Once these corrections have been made to the jet energies the missing energy must be corrected to reflect these changes. Two additional versions of the missing energy are calculated, one which is based one calorimeter energy only and another which includes additional corrections for muons which pass quality cuts. These two $\not\!\!E_T$ calculations form the basis of the $\not\!\!E_T$ calculated in this analysis (see Section 3.8.3).

3.10.2 Revertexing by Cluster-Track Projection

As mentioned earlier, the standard distinction between photons and electrons is based on whether or not a track is found in the road defined by the calorimeter cluster and the primary vertex. If the vertex position is not measured accurately, the road definition is incorrect, which leads to possible misidentification of electrons

as photons. Any kinematic quantities (E_T, invariant masses, etc.) which depend on the vertex position will be affected as well. The cluster-track projection method was developed to correct this problem and is documented in Reference [76].

Cluster-track projection begins by redefining an electron. Instead of relying on tracking roads to define an electron, an electron is defined by track-cluster association, which is based solely on the track match significance of a given track-cluster pair. The track which is best matched to a cluster is not required to fall within the tracking road described previously; it need only satisfy the track match significance criteria.

This best matched track is then used to unambiguously determine where the electron originated by extrapolating the line connecting the calorimeter cluster centroid and the drift chamber hits center of gravity to the beamline. Thus the vertex z position, denoted z_v, is given by

$$z_v = z_0^{\rm trk} - \left(\frac{z_0^{\rm cal} - z_0^{\rm trk}}{\rho_0^{\rm cal} - \rho_0^{\rm trk}} \right) \rho_0^{\rm trk} \tag{3.1}$$

where $(z_0^{\rm trk}, \rho_0^{\rm trk})$ and $(z_0^{\rm cal}, \rho_0^{\rm cal})$ are the centroid positions of the drift chamber and calorimeter hits, respectively. This extrapolation is shown schematically in Figure 3.4 for clarity. The track hit centroids are used since corrections to CDC delay line biases are parameterized in terms of the centroid positions [77]. The best matched track must satisfy the significance criteria described earlier: $S_{\rm track} < 5$ in the central region and $S_{\rm track} < 10$ in the forward region.

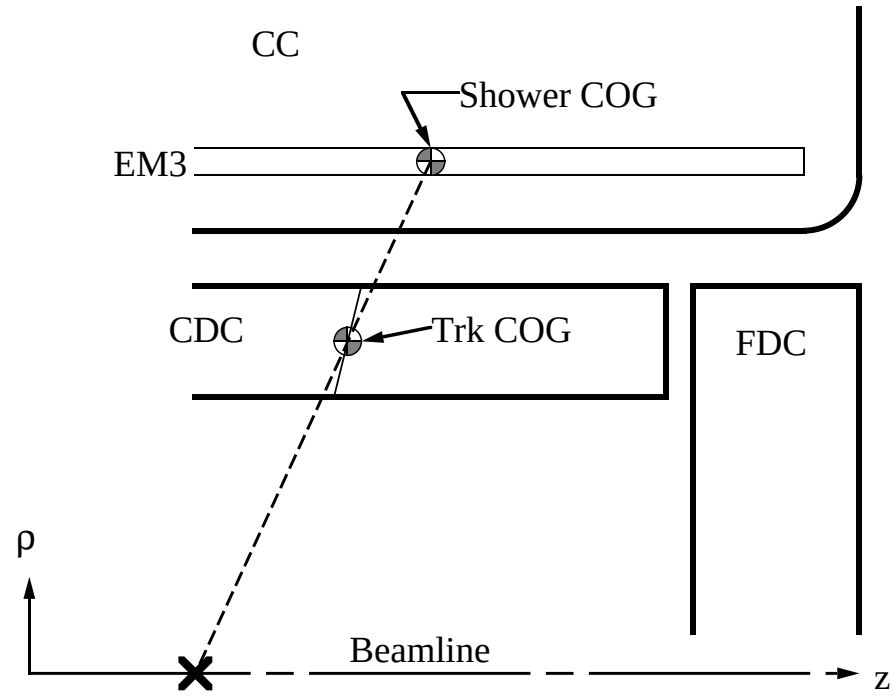

Figure 3.4: Vertex determination by cluster-track projection method.

The vertex resolution achieved by this technique, measured from the differences in the z-intercepts (z_{v1}, z_{v2}) from the two electrons in $Z \rightarrow ee$ candidate events, was found to be $\sigma_z \approx 2.0$ cm (or better) for either central or forward electrons.

It is possible to quantify the frequency at which DØRECO mismeasures the primary vertex position. A vertex is considered mismeasured if it is at least 10 cm ($\sim 5\sigma_z$) distant from the electron vertex. The rate at which this occurs in $Z \rightarrow ee$ candidate events grows as the instantaneous luminosity increases. The rate at which $(z_{v1} - z_{v2}) > 10$ cm is relatively insensitive to the instantaneous luminosity, which indicates that the electron-vertexing technique is robust [76].

3.10.3 Missing Energy Corrections

The $\not\!\!E_T$ calculation for this analysis begins with the missing energy which includes jet corrections calculated by CAFIX. The EM objects in the event are corrected to the electron vertex determined by the cluster-track projection technique described in the previous section using the electron closest to $\eta_{det} = 0$ with a matched track. The vector sum of the corrections to the electrons are subtracted from $\not\!\!E_T$. Any jets in the event with transverse energy E_T greater than 10 GeV are corrected to the electron vertex by treating them as point-like (i.e. reclustering of the jet with respect to the new vertex z-position is *not* done). The corrections to the jets are also subtracted from $\not\!\!E_T$. The algorithm for revertexing the jets uses the average radius of the hadronic part of the central calorimeter and the average z position of the hadronic part of the endcap calorimeter when recalculating the jet E_T. This is done to ensure that the $\not\!\!E_T$ is corrected by all calorimeter objects in the event, not just EM objects. Correcting the $\not\!\!E_T$ only for EM objects might create false $\not\!\!E_T$ due to the imbalance from not correcting the jet E_T's.

Chapter 4

Event Selection

4.1 Data Samples

The data samples used in this analysis was the Electroweak group's μDST sample. The data was streamed into two samples, the $W \rightarrow e\nu$ sample and the $Z \rightarrow ee$ sample. The Z sample was made from the 93-95 and 95-96 data samples. The W sample was made from 93-95 data sample only. The $W \rightarrow e\nu$ stream required at least one EM object with $E_T > 15$ GeV and $\not\!\!E_T > 10$ GeV; the $Z \rightarrow ee$ stream required at least 2 EM clusters with $E_T > 10$ GeV.

A third diagnostic sample was created from events which fired the single electron triggers in the 93-95 and 95-95 data samples. Data taken under this trigger were highly prescaled because of the loose requirements of one low E_T EM cluster.

In selecting $l\nu ee$ $(l = \mu, e)$ candidates, bad runs were excluded. These bad

runs had known calorimeter or tracking problems. Runs where the luminosity was unknown were also rejected.

In the final analysis the data sample used to select $WZ \to l\nu ee$ events was the Z sample because of the higher available luminosity. The W sample was used only as a cross check.

4.2 Luminosity

The GET_FILT_LUM utility was used to obtain the integrated luminosity of the streamed data sets for the Level-2 filters used in this analysis. The GET_FILT_LUM utility takes into account any any active veto scheme that was present in the trigger, as well as any prescales that were applied. After applying the GOODBEAM requirement offline, the integrated luminosity was found to be 92.3 pb^{-1} . The efficiency of the offline GOODBEAM cut was estimated by counting the number of events before and after the GOODBEAM cut. The error in the integrated luminosity introduced by this estimate is 0.7%. A 5.4% systematic uncertainty is assigned to the integrated luminosity as determined from the luminosity database. The two errors added in quadrature gives an error of 5.4% on the luminosity. The final integrated luminosity for the $l\nu ee$ analysis is therefore $\mathcal{L} = (92.3 \pm 5.0)\text{pb}^{-1}$.

4.3 Trigger

The Level-2 trigger used in this analysis, EM2_EIS2_HI, is described below:

- Level-0 trigger (hardware)
  - The universal Level-0 minimum bias requirement was imposed throughout the data taking period: this consisted of the detection of an inelastic collision with simultaneous hits in the north and south Level-0 counters, as well as a fast z determination with $|z| < 100$ cm.
- Level-1 trigger (hardware)
  - 2 EM objects with $E_T^{EM} > 7.0$ GeV;
  - events occurring in the MRBS_LOSS *and* MICROBLANK periods simultaneously were rejected.
- Level-1.5 trigger (hardware)
  - 2 EM objects with $E_T^{EM} > 12.0$ GeV
  - and with EM fraction > 0.85.
- Level-2 filter (software)
  - 2 EM objects with $E_T > 20.0$ GeV;
  - Loose shower shape and isolation cuts on both objects.

4.4 Offline Electron Selection

For this analysis electrons are classified as "loose" or "tight" electrons with the tight electrons being a subset of the loose electrons. A loose or tight electron must fall within a fiducial volume where electrons can be well measured. This excludes the regions between the CC and EC cyrostats, $1.1 < |\eta_{det}| < 1.5$, where the electron identification efficiency is poor, the very forward regions of the detector where the segmentation of the EM calorimeter decreases, $|\eta_{det}| > 2.5$, the edge of the CDC where the tracking efficiency drops, $1.0 < |\eta_{det}| < 1.1$, and the gaps between the 32 modules of the first layer of the central electromagnetic calorimeter (CCEM).

The fiducial region for loose and tight electrons is then defined as:

- Central Calorimeter (CC): $|\eta_{det}| < 1.0$ and $|\Delta\phi(\text{cluster,crack})| > 0.01$

  $\Delta\phi$(cluster,crack) is the separation between the shower centroid and the boundaries of the first layer of EM modules which occur at $\phi = \frac{2n\pi}{32}$, n=0 to 31.

- Endcap Calorimeter (EC): $1.5 < |\eta_{det}| < 2.5$

Loose and tight electrons are required to pass shower shape and isolation cuts. A tight electron is required to have a matching track and a loose electron is required to have either a matching track or hits in the drift chamber along a ϕ road between the EM cluster centroid and the z axis.

The criteria for loose and tight electrons are:

- Tight Electron
  - Isolation $I < 0.10$
  - Shower shape covariance parameter

    $\chi^2 < 100$ in the CC

    $\chi^2 < 200$ in the EC
  - A matching track with significance

    $S_{track} < 5$ in the CDC

    $S_{track} < 10$ in the FDC
- Loose Electron
  - Isolation, $I < 0.10$
  - H-matrix $\chi^2 < 100, 200$ (CC, EC)
  - Number of hits on drift chamber wires $NH_{xy} > 20$, 36 (CDC, FDC)

    or a matching track with significance $S_{track} < 5, 10$ (CDC, FDC)

The choice of the tracking cuts for the electrons was motivated by the need to maintain high efficiency. In this analysis we used relatively loose electron identification cuts since the backgrounds are small. Two variables used in electron identification, the dE/dx and TRD information, were not used in this analysis to maintain high efficiency. The explicit track requirement was dropped for loose electrons because some tracks are not reconstructed in a high luminosity environment.

4.5 Offline Muon Selection

The following quality cuts were used to select the muon:

- $|\eta| < 1.0$
- Muon fit quality IFW4$\leq$1
- Hadronic fraction HFRAC$\geq$0.70
- $|xy$ impact parameter$| \leq 25$ cm
- Floating time offset $(|t_0^{float}|) \leq 200$ ns
- Field Integral $\int \vec{B} \cdot \vec{dl} \geq 0.6$ GeV
- Isolation $\Delta R(\mu, jet) \geq 0.5$ for $E_T^{jet} > 10$ GeV

The first cut allows only muons in the CF region, eliminating punch-through and combinatoric backgrounds. The second cut is on the quality of the muon track fit. The third cut is used to ensure that the muon deposits energy in its passage through the calorimeter, thus rejecting fake muon tracks due to noise hits. The fourth and fifth cuts are used to reject cosmic muons, which do not necessarily pass near the beam line and which arrive out of time with the beam crossing.

4.6 $WZ \rightarrow e\nu ee$ event selection.

$WZ \rightarrow e\nu ee$ events are characterized by three high-E_T electrons and large $\not\!\!E_T$. The following cuts are used to select events:

- Events occurring in the MRBS_LOSS *or* MICROBLANK periods are rejected
- Events must pass the EM2_EIS2_HI trigger;
- One tight electron with $E_T > 25$, one loose electron with $E_T > 25$ GeV and one loose electron with $E_T > 10$ GeV ;

  The cut on the first two electrons is chosen so that the trigger efficiency is greater than 98%. The cut on the third electron, which is assumed not to be one of the trigger electrons, is allowed to be as loose as practical. The tight electron is used to define the vertex using the cluster-track projection technique. If two or more tight electrons are found, the central most (smallest $|\eta_{det}|$) electron is used to define the vertex.
- $\not\!\!E_T > 15$ GeV

  This is the $\not\!\!E_T$ corrected for the changes in electron and jet E_T due to revertexing.
- Events with invariant and transverse mass consistent with the Z and W are selected.

The transverse mass of electron k and the $\not\!\!E_T$ must be greater than 30 GeV/c^2 and the invariant mass of electron i and j is between 81 and 101 GeV/c^2, i.e.

$$m_T(k, \not\!\!E_T) > 30\,\mathrm{GeV/c^2}$$

where

$$m_T^2 = 2E_T^e \not\!\!E_T (1 - \cos(\phi^e - \phi^\nu))$$

and

$$81\,\mathrm{GeV/c^2} < m_{i,j} < 101\,\mathrm{GeV/c^2}$$

These cuts are checked for all three combinations of electrons i, j, and k. If more than one combination passes the cut, the combination with the Z mass closest to 91 GeV is used. This cut along with the $\not\!\!E_T$ cut is used to reject background from two electron plus one jet events where the jet fakes an electron.

After applying all the event selection cuts one event is selected. The properties of the event are summarized in Appendix A. This event has two reconstructed vertices at $z = -23$ and $+25$ cm. One high E_T electron and two high E_T photons are identified by the reconstruction program using the vertex at -23 cm as shown in Figure 4.1. The end view of the calorimeter and tracking is shown in Figure 4.2. Upon revertexing, a track pointing towards the vertex at $+25$ cm is matched to one of the photons identifying it as a tight electron. The electron also has a track pointing towards the vertex at $+25$ cm. The second "photon" has hits in a road pointing

towards the vertex at +25 cm. Revertexing the event using the two tight electrons yields a vertex z position of +25.5 cm. The two tight electrons form an invariant mass of 93.6 GeV/c^2 and have a di-electron transverse momentum of 58.8 GeV/c. The loose electron and the corrected missing transverse energy form a transverse mass of 74.7 GeV/c^2 with a transverse momentum of 63.0 GeV/c.

4.7 $WZ \to \mu\nu ee$ event selection

$WZ \to \mu\nu ee$ events are characterized by two high-E_T electrons, a high p_T muon, and large $\not\!\!E_T$. The following cuts were used to select events:

- Events within the MRBS_LOSS and MICRO_BLANK gate are rejected;
- Events must pass the EM2_EIS2_HI trigger;
- Events must have one tight electron with $E_T > 25$, one loose electron with $E_T > 25$ GeV and one muon with $p_T > 15$ GeV ;
- Events must have muon-corrected and calorimeter missing transverse energy $\not\!\!E_T > 15$ GeV.

The calorimeter missing energy cut ensures that the missing energy is real and not just an artifact of a mismeasured muon. No events are observed with this minimal set of cuts.

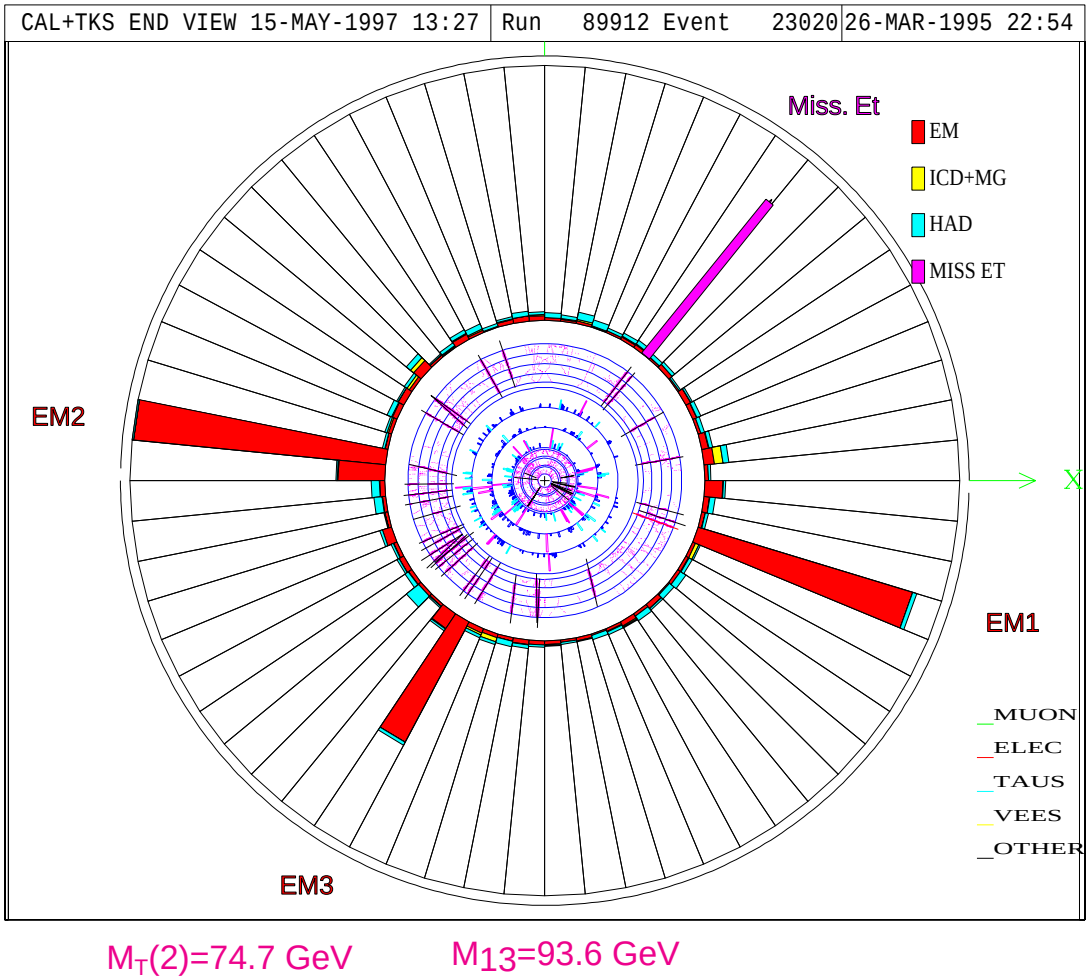

Figure 4.1: Candidate event display showing end view of calorimeter and tracking.

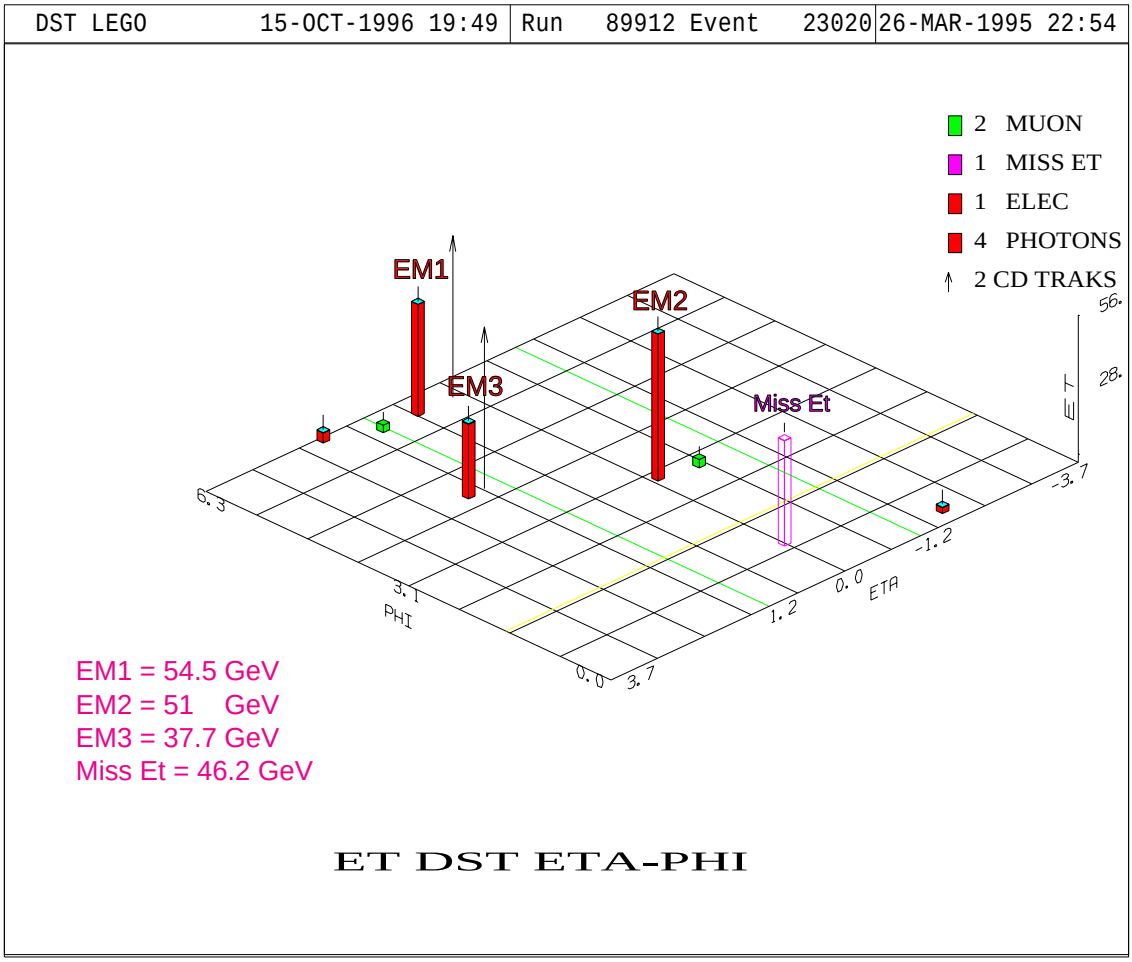

Figure 4.2: Candidate event display showing the E_T of objects in $\eta - \phi$ space.

Chapter 5

Detection Efficiencies

Not all events produced in a collision will be recorded by the detector. Events might not fire a hardware or software trigger and the event might not pass the particle identification criteria. In order to estimate this loss, the efficiencies of the trigger and the offline particle identification criterion must be determined.

5.1 Trigger Efficiency

To estimate the loss of events that do not fire a trigger, a trigger efficiency needs to be determined. Ideally the trigger efficiency would be obtained from the ratio of the number of events passing the EM2_EIS2_HI trigger to events selected with no trigger requirement. A more practical method is to evaluate the trigger efficiency for an electron to pass the Level 2 trigger requirements using data selected with a

trigger with looser requirements than the EM2_EIS2_HI trigger. Data taken with the EM2_ELE_ESC trigger had the same Level-1 requirement as the EM2_EIS2_HI trigger, but a looser E_T requirement (16 GeV) and no isolation or shape requirements, and are therefore unbiased with respect to the EM2_EIS2_HI trigger. The Level-2 efficiency for $E_T > 20$ GeV can be measured using coincidences of the two filters in $Z \rightarrow ee$ data. The fraction of events in each E_T bin which satisfied the level-2 $E_T > 20$ GeV is a measure of the E_T dependence of the efficiency of the Level-2 requirement. The resulting efficiency turn on curve is shown in Figure 5.1. A cut of 25 GeV yields a trigger efficiency of greater than 98% per electron for CC or EC electrons.

5.2 Electron Identification Efficiencies

To estimate the loss of events that do not pass the offline particle identification criteria described in Chapter 4, an ID efficiency needs to be determined. The efficiency of ID cuts are determined using $Z \rightarrow ee$ events as described in Reference [76] for the 93-95 and 95-96 data samples. The change in the number of events in the Z mass window for different cuts allows a relative efficiency to be determined. Backgrounds are subtracted from the Z-mass windows using two methods and two mass windows. The first method uses sideband averaging to determine the background in the Z mass window. The second method fits the di-electron mass

distribution to a Breit-Weigner distribution convoluted with a Gaussian distribution plus a linear background and subtracts the linear background from the Z mass peak. The mass windows used were of width 10 GeV and 20 GeV centered on the Z mass of 91 GeV.

The relative efficiency of cut "a" relative to some looser cut "b" is given by

$$\epsilon_{ab} = S_{ab}/S_b$$

where S_{ab} and S_b denote the number of background-subtracted events in the mass peak after background subtraction for cuts "a" and "b" together and cut b alone, respectively. Using the two methods with the two mass windows, four estimates of the efficiency are obtained. The efficiency is taken to be the average of the four methods. Errors are calculated using the binomial error on the ratios added in quadrature with the largest difference between the average and the four efficiencies. Table 5.1 lists the efficiencies obtained in this manner for both the forward and central regions. The quantities ϵ_t and ϵ_l in Table 5.1 are the identification efficiencies for tight and loose electrons, respectively. The efficiency for the calorimeter-based cuts (I, χ^2) is denoted $\epsilon_{\rm cal}$, the efficiency for track reconstruction is denoted $\epsilon_{\rm trk}$, and the efficiency for a track or hit requirement is denoted $\epsilon_{\rm hit}$. With these definitions, $\epsilon_t \simeq \epsilon_{\rm cal}\epsilon_{\rm trk}$ and $\epsilon_l \simeq \epsilon_{\rm cal}\epsilon_{\rm hit}$.

The efficiencies for the isolation and shower shape requirements are valid for high E_T electrons and photons. However, corrections must be made at low E_T.

Quantity	CC Value (%)	EC Value (%)
$\epsilon_{\rm cal}$	91.5 ± 0.2	92.2 ± 0.2
$\epsilon_{\rm trk}$	80.2 ± 0.3	73.8 ± 0.4
$\epsilon_{\rm hit}$	96.8 ± 0.4	95.8 ± 0.5
ϵ_l	88.6 ± 0.3	88.4 ± 0.5
ϵ_t	73.4 ± 0.5	67.2 ± 0.3

Table 5.1: Measured efficiencies for electron identification. See text for definitions.

The calorimeter showers of photons and electrons are expected to be very similar, therefore the effect of calorimeter ID cuts on electrons and photons at low E_T should be similar. The effects of calorimeter ID cuts on low E_T photons have been studied [76]. A summary of the method is given.

To measure the low E_T dependence of the calorimeter-based quality cuts, the calorimeter response to a sample of photons was simulated using a full Monte Carlo simulation of the DØ detector, DØGEANT [79]. These events were then superimposed on non-zero-suppressed minimum bias collider events to simulate underlying event effects for various instantaneous luminosities. The events were weighted to reflect the instantaneous luminosity distribution of the $Z \rightarrow ee$ sample. Figure 5.2 shows the shape of the resulting efficiency of the calorimeter-based quality cuts. Before using these curves for efficiency calculations, they were shifted upward so that their plateau values matched the values obtained from data. A similar study [80] was done for low E_T electrons and a similar low E_T behavior was seen.

To determine if there is an E_T dependence for the tracking variable efficiencies, events selected with the EM2_ELE_ESC trigger, which contained electrons with $E_T \geq 16$ GeV, were used. Within errors, the track match and hits cut efficiency relative to the calorimeter cuts are the same for high E_T and low E_T electrons. Therefore no E_T dependence is assigned to the tracking efficiencies. The efficiency of the track match cut relative to the calorimeter cuts in these events was found to be $80.4 \pm 0.2(\text{sys}) \pm 0.5(\text{stat})\%$ for the CDC and $72.6 \pm 0.4(\text{sys}) \pm 0.8(\text{stat})\%$ for the FDC. The efficiency of the hits cut relative to the calorimeter cuts was found to be $97.1 \pm 0.2(\text{sys}) \pm 0.2(\text{stat})\%$ for the CDC and $95.3 \pm 0.2(\text{sys}) \pm 0.4(\text{stat})\%$ for the FDC.

5.3 Muon Identification Efficiencies

Since the muon identification criteria used in this analysis are identical to those used in the DØ $WW \rightarrow l\nu l'\nu'$ analysis [81, 82] of the 93-95 data sample, we use the efficiencies calculated in that analysis, which are detailed in Reference [81]. The efficiencies for each cut were determined from a combination of Monte Carlo and data. The efficiencies for the IFW4 and $\int \vec{B} \cdot \vec{dl}$ cuts as a function of $\eta - \phi$ were determined from DØGEANT events, and the efficiencies of the remaining cuts were determined from data. The efficiency of each cut, except the IFW4 and $\int \vec{B} \cdot \vec{dl}$ cut, was determined using $Z \rightarrow \mu\mu$ events. The overall efficiency for muons with

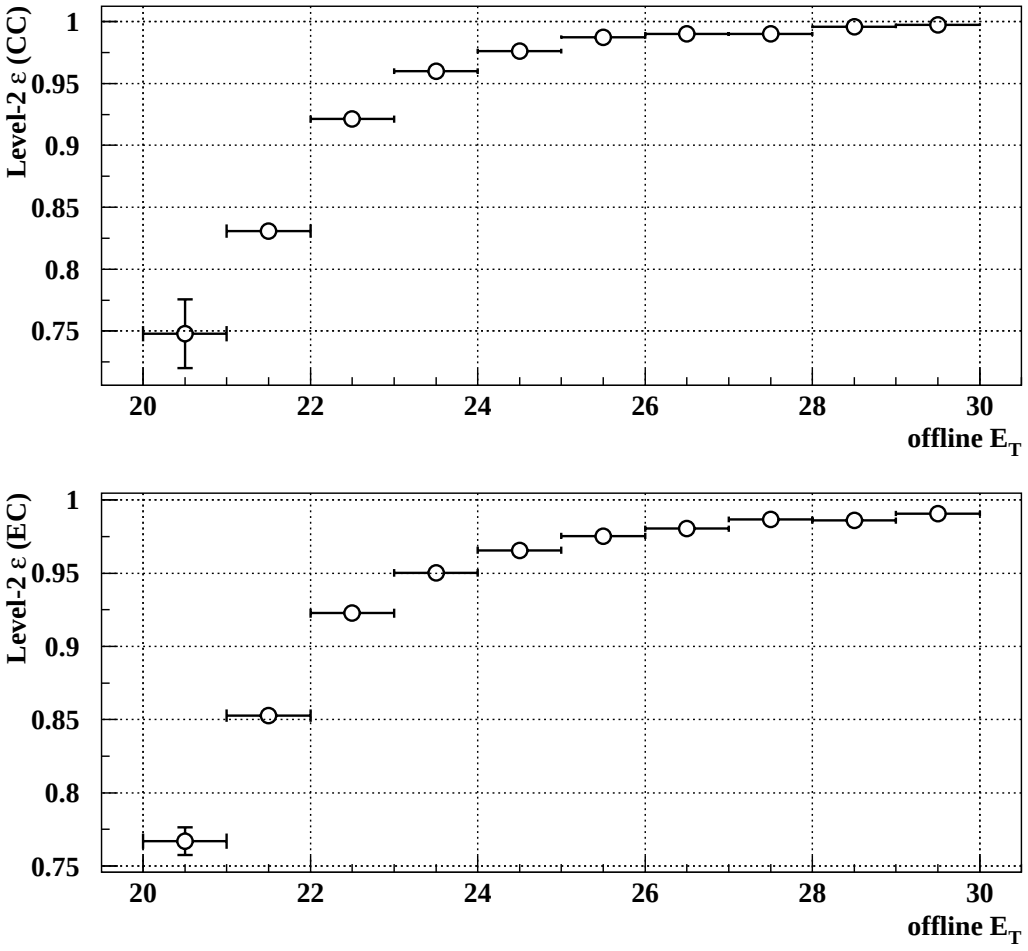

Figure 5.1: Trigger turn-on curve for Level 2 $E_T > 20$ GeV requirement as a function of offline electron E_T cut for EC and CC electrons. Error bars are statistical only.

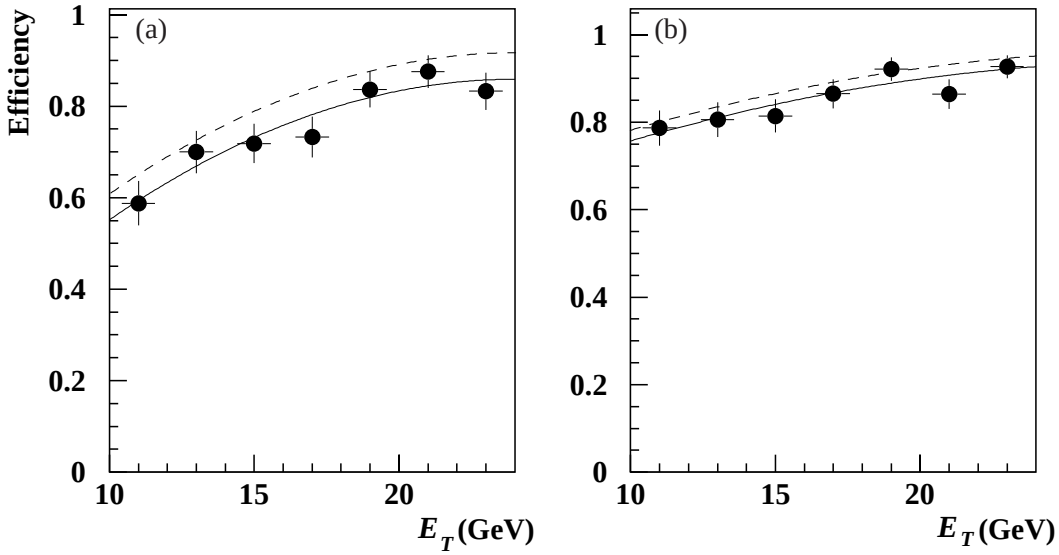

Figure 5.2: Efficiency of the isolation and shower shape requirements vs. photon E_T for (a) CC EM clusters and (b) EC EM clusters. The measured values (points and fitted solid line) from Monte Carlo photons are shifted upwards (dashed curves) so that the plateau values match those obtained from data.

$p_T > 15$ GeV was determined to be 0.70 ± 0.03. The efficiencies of the individual cuts are shown in Table 5.2

Cut	Efficiency
hadronic fraction	0.96 ± 0.01
impact parameter	0.99 ± 0.01
t_0^{float}	0.98 ± 0.01
isolation	0.75 ± 0.03
combined (per muon)	0.70 ± 0.03

Table 5.2: Muon identification efficiencies (per muon) determined from data.

Chapter 6

Signal Event Simulation

The number of events predicted is determined by multiplying the theoretical cross section by the integrated luminosity. However, to determine the number of events visible in the detector it is necessary to simulate the response of the detector and the offline reconstruction and event selection. A detection efficiency is determined from this simulation. The number of events seen is then the number of predicted events multiplied by the detection efficiency.

6.1 Monte Carlo Event Generator

The leading order Monte Carlo event generator of Zeppenfeld, *et al.* [9] was used to calculate the WZ production cross section as a function of the WWZ couplings and to obtain distributions of various kinematic variables. The cross section

calculated by this program includes multiplication by a "K-factor" equal to 1.335 to take into account the effects of higher order QCD corrections. The program was modified to output the 4-vectors of the final state particles for input to the detector simulation described below.

The Zeppenfeld Monte Carlo event generator does not take into account the effects of initial state radiation (ISR), which give rise to a significant transverse momentum of the WZ system. Therefore, Standard model WZ events were generated using PYTHIA [8] to determine the transverse momentum distribution of the WZ system. The effects of ISR are included in this event generator and the resulting p_T distribution of the WZ system is plotted in Figure 6.2. The cross section times branching ratio as calculated by PYTHIA is

$$\sigma(p\bar{p} \to WZ + X) \times B(W \to l\nu) \times B(Z \to l^+l^-) = 7.9\,\text{fb}.$$

This agrees with the cross section calculated by the Zeppenfeld Monte Carlo, 10.3 fb, once the "K-factor" is taken into account.

6.2 Detector Simulation

A large number of events need to be run through a detector simulator in order to calculate detection efficiencies for non Standard Model values of the WWZ couplings. Since a full detector simulation such as GEANT [79] takes a large amount of CPU time, a fast detector simulator, called DIPS [83], was developed by the DØ

diboson physics group which parameterizes the detector response and can be used to quickly calculate the detector efficiency.

The fast detector simulator takes the following effects into account:

- electrons and photons energies are smeared according to the observed resolution of the electromagnetic calorimeter

$$\left(\frac{\sigma_E}{E}\right)^2 = C^2 + \frac{S^2}{E} + \frac{N^2}{E^2}$$

  where E is the energy of the electron, C is the calibration error term , S is the sampling fluctuation term, and N is the noise term. The sampling term is taken from data and the noise and calibration terms were tuned to match those obtained from $Z \to ee$ events which were simulated with DØGEANT and overlaid with minimum bias collider data [76].

- muon momentum is smeared according to the resolution function

$$(\frac{\sigma_{1/p}}{(1/p)})^2 = (a(p - p_0)/p)^2 + (bp)^2$$

  where a, b, and p_0 are determined from data [84].

- the primary vertex z position is smeared using a Gaussian distribution with mean 0 and width 29 cm, and the 4-vectors are projected from that location;

- the missing energy distribution from minimum bias events is added to the existing missing energy to simulate the effect of underlying events on the missing energy measurement (see Figure 6.1);

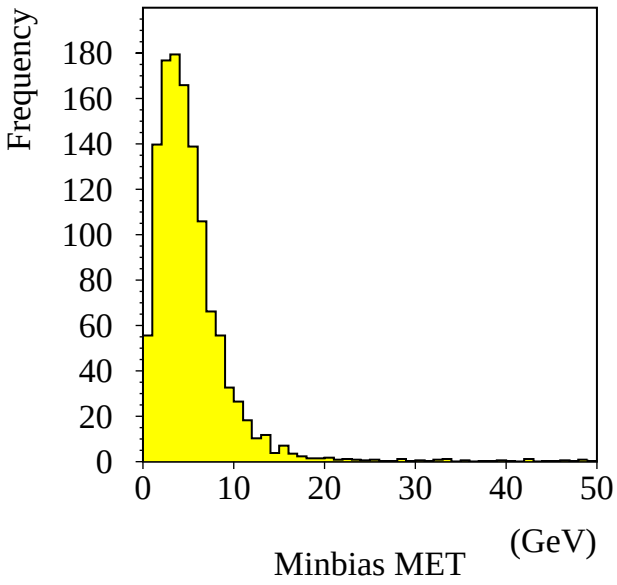

Figure 6.1: Distribution of the $\not\!\!E_T$ from minimum bias events.

- the WZ system is simulated using the p_T distribution for Standard Model PYTHIA events as shown in Figure 6.2.

- electrons are required to fall within regions of the detector where the detection efficiency is well understood, i.e. the CC and EC regions;

- the efficiency for muons is modeled using an $\eta - \phi$ efficiency map which accounts for the numerous cracks and holes in the muon system as shown in Figure 6.3.

- events must pass trigger and particle identification criteria – the efficiencies

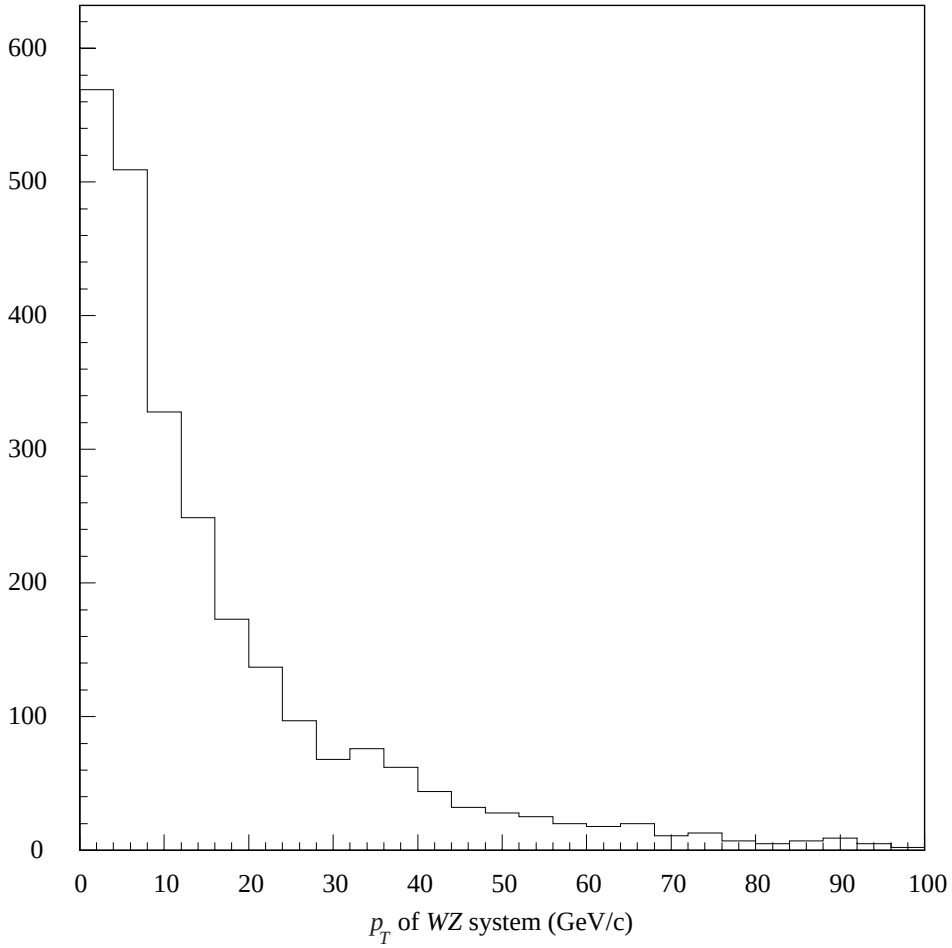

Figure 6.2: Distribution of the WZ system recoil p_T obtained from Standard Model PYTHIA $WZ \to l\nu l^+ l^-$ events.

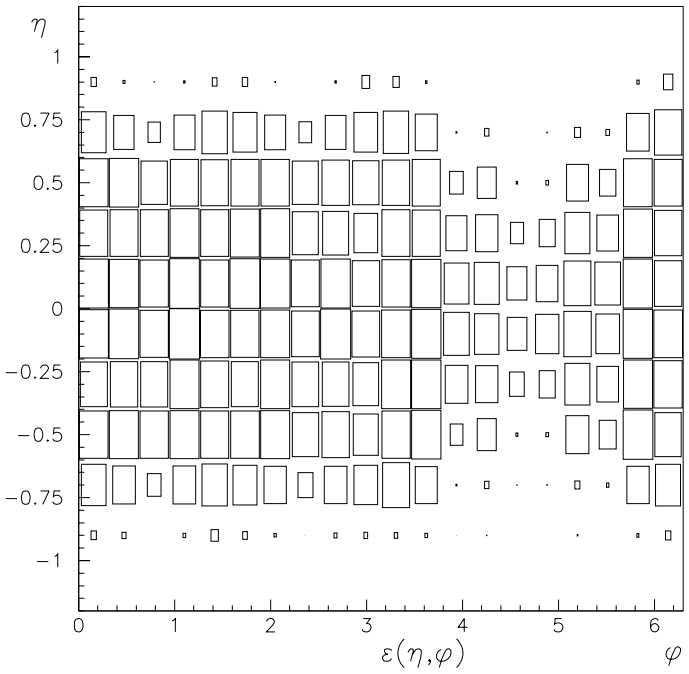

Figure 6.3: Efficiency of muon identification cuts as a function of η and ϕ. The size of the boxes represents efficiency in each region.

calculated from data (see Chapter 5) are applied;

As a cross check to the fast detector simulation, Standard Model $WZ \to l\nu ee$ events were processed using the full detector simulation, DØGEANT. The same 4-vectors were run through the fast detector simulator. The kinematic distributions from each detector simulation were compared and found to be in good agreement. The trigger and offline selection cuts applied were the same as the full event selection cuts, except that $\not\!\!E_T$, transverse mass and invariant mass cuts were not applied, as

shown in Figure 6.4. Figure 6.5 shows the mass and $\not\!\!E_T$ distribution of $WZ \to e\nu ee$ signal events. Also shown are the mass and $\not\!\!E_T$ cuts applied in selecting $e\nu ee$ events.

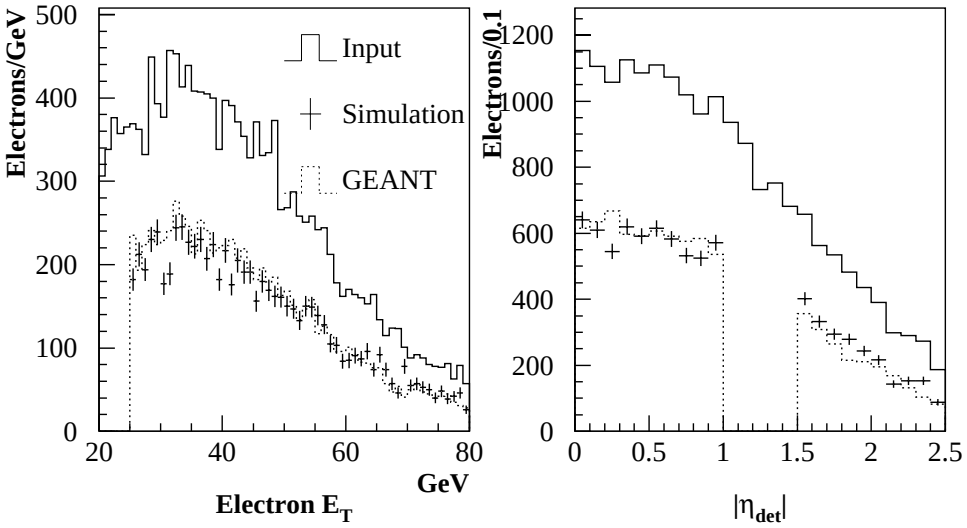

Figure 6.4: Comparison of electron E_T and ϕ distributions from DØGEANT and fast detector simulator after kinematic, trigger and fiducial cuts have been applied. Also shown is the input electron distributions from PYTHIA.

6.3 Detection Efficiencies and Standard Model Signal Estimates

A sample of Standard Model $WZ \to e\nu ee$ events were generated and run through the fast detector simulation. The detection efficiency was determined by

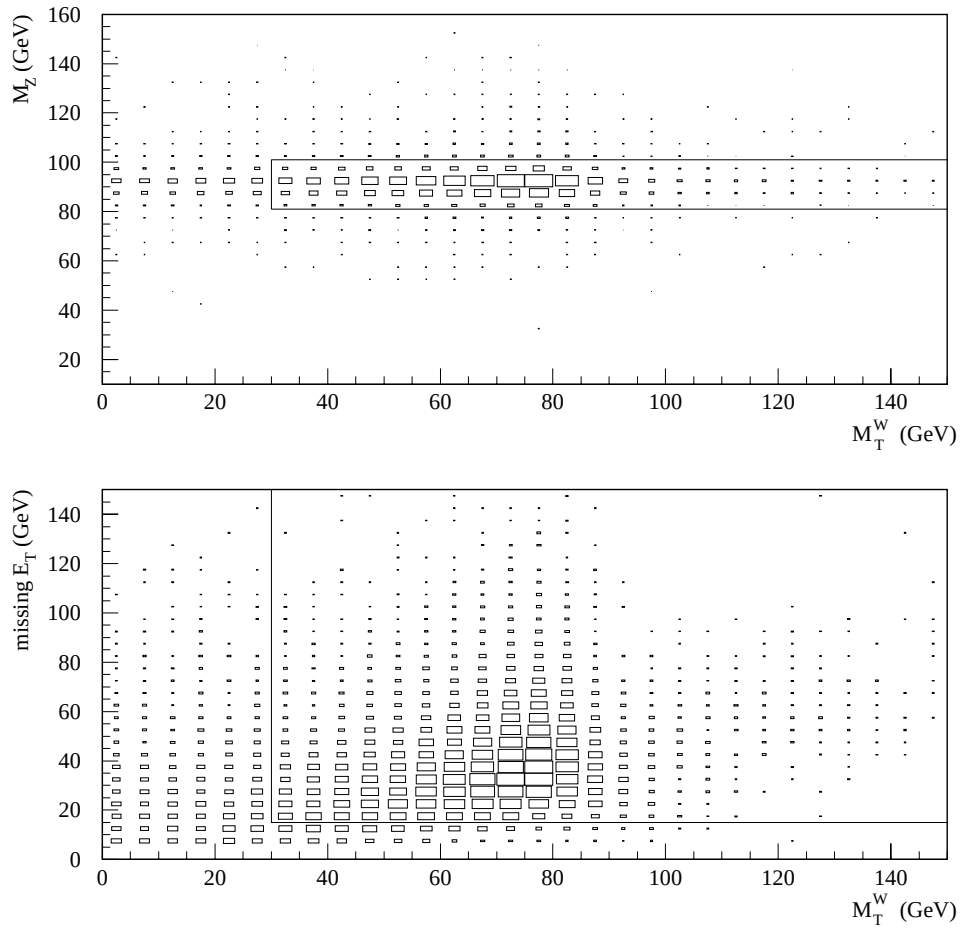

Figure 6.5: Distributions from Zeppenfeld-DIPS Monte Carlo for Standard Model $WZ \to e\nu ee$ signal events after all cuts except mass and $\not\!\!E_T$ have been applied. The lines show where the mass and $\not\!\!E_T$ cuts are applied to data.

taking the ratio of the number of events surviving all cuts over the number of events input. The detection efficiency was found to be $\epsilon = (16.9 \pm 0.2)\%$.

The predicted number of events, N_{SM}, for WZ production in the $e\nu ee$ channel

is given by

$$N_{SM} = \epsilon \cdot \sigma_{SM} \cdot \mathcal{L}$$

where $\epsilon = (16.9 \pm 0.2)\%$ is the overall detection efficiency, $\sigma_{SM} = 0.0094 \pm 0.0005$ pb is the Standard Model cross section from the Zeppenfeld Monte Carlo, and $\int \mathcal{L} dt = 92.3 \pm 5.0$ pb^{-1} is the integrated luminosity. This gives $N_{SM} = 0.146 \pm 0.002\,(\text{stat}) \pm 0.012\,(\text{syst})$.

The statistical error is the error on the overall detection efficiency which is limited by Monte Carlo statistics. The systematic error includes the uncertainty on integrated luminosity, particle identification efficiency, trigger efficiency, and the uncertainty in the Monte Carlo cross section due to choice of parton distribution function (PDF) and momentum transfer (Q^2) scale. The uncertainty on the Monte Carlo cross section was found by varying the PDF and Q^2 scale and taking the average of the differences from the cross section calculated using the MRSD$-'$ PDF. These errors are summarized in Table 6.1 and added in quadrature to give an overall systematic uncertainty of 8.5% in the $e\nu ee$ channel.

In the $WZ \rightarrow \mu\nu ee$ channel, the efficiency for detecting SM events was determined to be $(11.5 \pm 0.15)\%$. Using the same integrated luminosity and cross section as the $e\nu ee$ channel, the Standard Model expectation for the $\mu\nu ee$ channel is 0.099 ± 0.001 (stat) ± 0.009 (syst) events.

Source	% Error
integrated luminosity	5.4%
ID efficiency	0.7% (per electron) 4.4% (per muon)
trigger efficiency	2%
PDF and Q^2 scale choice	5%
Branching fraction	3.7%
Total:	8.5% ($e\nu ee$) 9.6% ($\mu\nu ee$)

Table 6.1: Systematic errors on SM signal estimates.

Chapter 7

Backgrounds

7.1 Backgrounds for the $WZ \to e\nu ee$ Channel

The physics backgrounds for this channel are negligible because of the high E_T cuts and the high $\not\!\!E_T$ cut. The backgrounds for this analysis come from a jet faking the signature of an electron. It is possible for a jet to form a π^0 or η which then decays into $\gamma\gamma$. If the π^0 has sufficient E_T the two photons will produce a electromagnetic shower which mimics that of an electron. If a low E_T charged hadron from the remainder of the jet or from the underlying event leaves hits in the drift chamber, the resulting hits + cluster might pass the electron identification cuts. Another background comes from a photon converting to an e^+e^- pair, which would be detected as one electromagnetic shower.

The largest background is expected to be from ee + jet events which acquire

their missing energy from the underlying event and the mismeasurement of the jet energy. A Monte Carlo simulation of these events would not take this effect into account, and therefore a data-based technique is used to estimate these backgrounds.

Two methods used to determine the background are described below. In the first method, the number of ee + jet events which pass all event selection cuts except that a jet is required instead of the third electron is counted and this number is multiplied by the probability of a jet faking an electron. In the second method, the number of events which pass all event cuts except that one electron fails the shower shape or isolation cut is counted. This number is then multiplied by the probability that a bad quality electron fakes a good quality electron. These events already contain three electromagnetic clusters and are more likely to fake the event signature than ee + jet events. This method is used as a cross check to the first but has poorer statistics because of the smaller number of events.

7.1.1 Background Estimate – Method 1

The ee + jet background is calculated from the same sample as the signal. Events must pass the EM2_EIS2_HI filter, have two electrons (tight or loose), one or more jets, and $\not\!\!E_T \geq 15$. Events are classified according to the following categories:

1. TLJ – one tight electron and one loose electron both with $E_T \geq 25$ and a jet with $E_T \geq 10$.

2. TJL^* – one tight electron with $E_T \geq 25$, one loose electron with $E_T \geq 10$ and a jet with $E_T \geq 25$

3. JLL^* – one loose electron and $E_T \geq 25$, one loose electron with $E_T \geq 10$ and a jet with $E_T \geq 25$. Because a tight electron can be counted as a loose electron only events where the first loose electron has no matching track are accepted to avoid double counting events in category 2.

In an event where a jet fakes one of the high E_T electrons and the second electron has $E_T < 30$ GeV the event might not pass the EM2_EIS2_HI trigger. The event was counted if it passes one of the single electron monitor triggers. Since the single electron triggers were prescaled with respect to the EM2_EIS2_HI trigger, a normalization of 9.7 ± 0.5 was applied to the number of events under these triggers. This normalization was based on the number of $Z \rightarrow ee$ events which fire both triggers.

The kinematic distributions of these ee + jet events before the mass and $\not\!\!E_T$ cuts are shown in Fig. 7.1 for events passing the EM2_EIS2_HI trigger.

The number of fake background events is found by summing the E_T dependent probability for all events which pass all event cuts, i.e.

$$N_{bkg} = \sum_{i=1}^{N_{evt}} w_i (\sum_{j=1}^{N_{jets}} P_j(E_T))$$

where N_{bkg} is the number of background events, N_{evt} is the number of ee + jet events passing all event cuts, w_i is the appropriate scaling factor for the trigger passed, N_{jet}

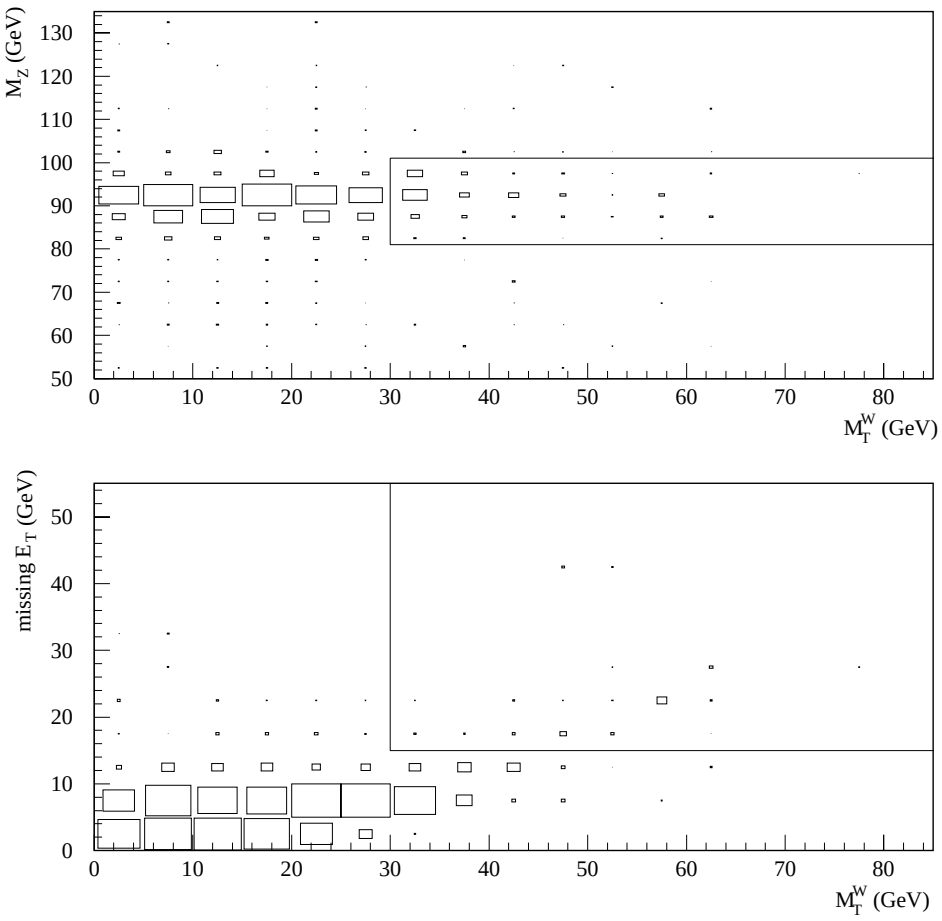

Figure 7.1: Jet background distributions from ee + jet events which fire the EM2 trigger before the mass and $\not\!\!E_T$ cuts have been applied. The lines show the effect of the mass and $\not\!\!E_T$ cuts.

is the number of jets in each event and $P_j(E_T)$ is the E_T dependent probability that jet i fakes a tight or loose electron. Each jet in an event is considered.

The fake probabilities, shown in Table 7.1, were determined by counting the number of electrons passing identification cuts found in a multijet sample, and taking the ratio of the number of electron to the number of jets [85]. The probability is a linear function of E_T.

Object Type	CC		EC	
	$a_0 \times 10^{-3}$	$a_1 \times 10^{-5}$	$a_0 \times 10^{-3}$	$a_1 \times 10^{-5}$
e_t	-0.173 ± 0.20	1.43 ± 0.51	0.528 ± 0.86	5.09 ± 2.3
e_l	0.0754 ± 0.29	2.06 ± 0.70	1.32 ± 1.0	6.31 ± 0.27

Table 7.1: Jet misidentification probabilities for tight and loose electrons. The probability is a linear function of E_T, $a_0 + a_1 E_T$. A systematic uncertainty of 25% is assigned to each fake probability. Uncertainties given in this table are statistical only. Table taken from [85].

The total ee + jet background is estimated to be $N_{bkg} = 0.38 \pm 0.07(\text{stat}) \pm 0.11(\text{syst})$ events. The number of background events in each category is shown in Table 7.2. The statistical error is due to the small size of the sample. The systematic error is dominated by a 25% uncertainty in the fake probabilities due to subtraction of direct photon events from the sample of multijet events used to calculate $P_j(E_T)$ [85].

category	CC	EC	Total
1. TLJ	0.056 ± 0.008	0.067 ± 0.015	0.123 ± 0.017
2. TJL^*	0.009 ± 0.009	0.000 ± 0.000	0.009 ± 0.009
3. JLL^*	0.097 ± 0.019	0.148 ± 0.060	0.245 ± 0.063
Total	0.162 ± 0.022	0.215 ± 0.062	0.377 ± 0.066

Table 7.2: Breakdown of ee + jet backgrounds by category (see text) and regions. Errors shown are statistical only.

7.1.2 Background Estimate – Method 2

In the second method, the background is also calculated from the same sample as the data. Two data sets are selected: one in which events pass all the signal cuts except the $\not\!\!E_T$ and mass cuts ("good sample"); the second in which events are selected in the same way except one or more electrons fail the isolation or shower shape calorimeter identification cuts ("bad sample"). The resulting bad sample is enriched with EM jets, which are more likely to fake an electron than some random jet. A normalization is determined by taking the ratio of the good events to bad events that fail the $\not\!\!E_T$ cut, $\frac{N_{\rm good}}{N_{\rm bad}}(\not\!\!E_T < 15)$. Multiplying the number of bad events which pass the $\not\!\!E_T$ cut $N_{\rm bad}(\not\!\!E_T > 15)$ by this normalization gives the number of background events, *i.e.*

$$N_{bkg} = \frac{N_{\rm good}}{N_{\rm bad}}(\not\!\!E_T < 15) \cdot N_{\rm bad}(\not\!\!E_T > 15)$$

The numbers obtained in this calculation are summarized in Table 7.3. The statistical error on the normalization ratio is the Poisson error due to the small number of good events failing the $\not\!\!E_T$ cut. The systematic error is found by varying the $\not\!\!E_T$ cut by ± 5 GeV and taking half the difference of the highest and lowest ratio. The statistical error on the number of background events is the Poisson error on the number of bad events passing added in quadrature with the Poisson error on the normalization. The systematic error is the systematic error on the normalization ratio. The kinematic distributions of these events before the mass and $\not\!\!E_T$ cuts are shown in Figure 7.2.

# bad events passing cuts	$4.00^{+3.16}_{-1.92}$
good/bad failing $\not\!\!E_T$cut	$0.105^{+0.062}_{-0.042}(\text{stat}) \pm 0.005(\text{syst})$
# background events	$0.42^{+0.41}_{-0.26}(\text{stat}) \pm 0.02(\text{syst})$

Table 7.3: Numbers used in fake electron method background calculation.

The final background estimate using this method is $N_{bkg} = 0.42^{+0.41}_{-0.26}$. This is consistent with the first method, but the uncertainty is larger, due to the low number of events from the bad sample passing the $\not\!\!E_T$ cut. The second method is

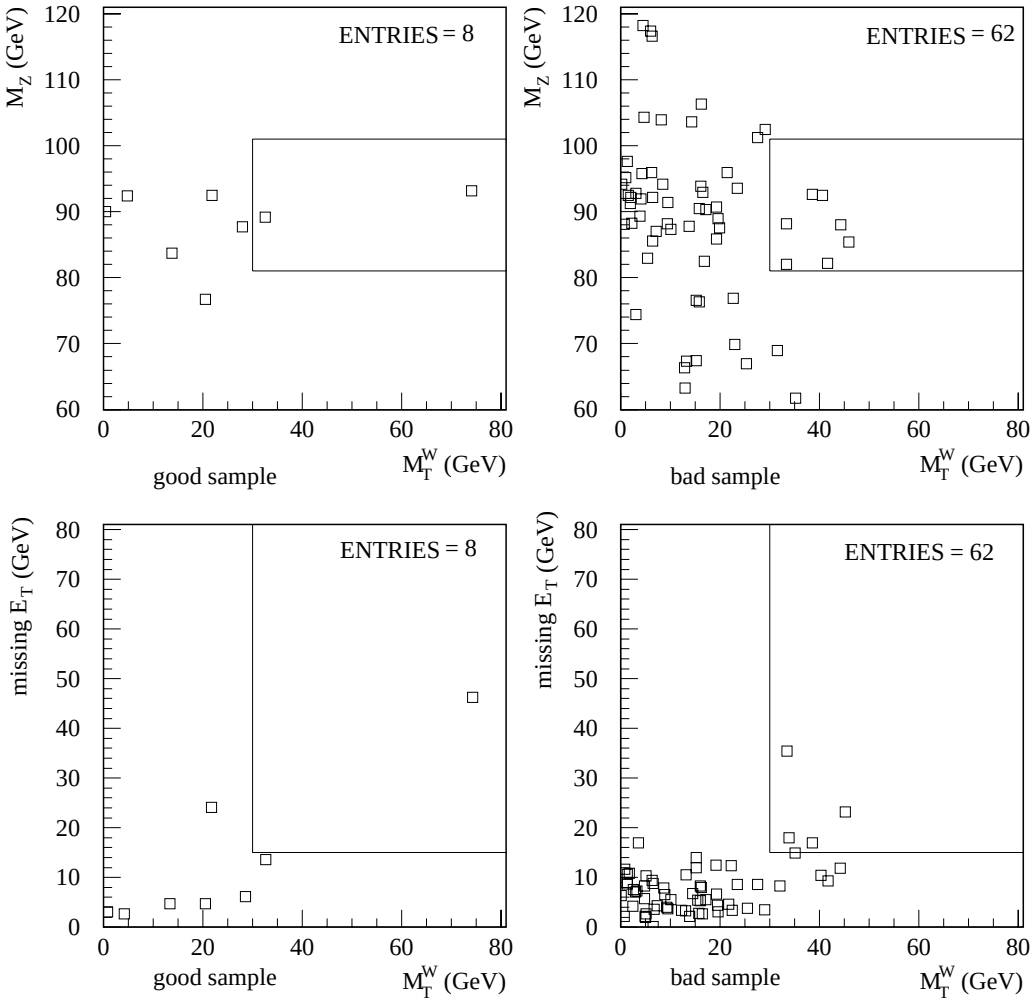

Figure 7.2: Fake background distributions for M_Z, M_T^W, corrected $\not\!\!E_T$, and M_T^Z showing the effects of the mass and $\not\!\!E_T$ cuts.

presented as a cross check to the first. For purposes of background subtraction, the first method is preferred because of the smaller uncertainty.

7.2 Backgrounds for the $WZ \to \mu\nu ee$ channel

As in the $e\nu ee$ channel the backgrounds for this channel come from processes in which a jet fakes the signature of an isolated muon or electron. The backgrounds include $ee + jet$ where the jet produces an isolated muon and $e\mu + jet$ where the jet fakes an electron. In both cases missing energy can result from the mismeasurement of the jet or muon, and therefore a data-based technique must be used to estimate the backgrounds.

7.2.1 ee + jet Background

Before proceeding it is necessary to calculate the probability of a jet producing an isolated muon. This probability was calculated from a sample of multijet events by counting the number of events containing an isolated muon and dividing by the total number of events in the sample. For a muon with $p_T > 15$ GeV this probability was found to be 1.5×10^{-5} [81]. In addition, the probability of a jet faking a muon from a heavy quark (b/c) jet was found by requiring a muon (isolated on non-isolated) in the opposite hemisphere from the isolated muon. This gave a heavy quark enhanced fake rate of 2.5×10^{-4}. A systematic uncertainty of

10% percent is assigned to both probabilities because of the small number of events found with an isolated muon.

To calculate the ee + jet background, events with two electrons and a central jet were selected from the $Z \rightarrow ee$ sample. Each event was required to pass all cuts except that the jet was only required to pass the muon fiducial and kinematic cuts. The number of events (88) is then multiplied by the probability of the jet producing an isolated muon. The number of events expected from this background is ≤ 0.002. A small fraction of the $ee + jet$ events contain real heavy quark (b/c) jets. Assuming that all of the jets in the fake sample are heavy quark jets and using the heavy quark enhanced fake rate, we obtain an upper limit of $N_{\rm bkg} = 0.022$ for this background. However, to set a conservative limit, we take the smaller estimate and neglect this background.

7.2.2 $e\mu$ + jet Background

The second background ($e\mu$ + jet) was calculated from the electroweak group's 93-95 $W \rightarrow e\nu$ data sample. Events in this sample required one EM object above 10 GeV and $\not\!\!E_T > 15$ GeV. A background data sample was selected by requiring events with an isolated muon, one or more jets and a tight or loose electron. All event selection cuts were applied with the exception of the trigger, which was replaced by the EM1_EIS_TRKCC trigger. This trigger required one EM object and missing energy at Level 2. A total of 60 events were selected.

The number of fake events is then found by multiplying by the E_T-dependent probability for a jet to fake an electron, accounting correctly for events which contain more than one jet:

$$N_{\rm bkg} = w_{\rm trig} \sum_{j=1}^{N_{\rm evt}} \left(\sum_{i=1}^{N_{\rm jet}} P_i(E_T) \right)$$

where $N_{\rm bkg}$ is the estimated number of background events, $N_{\rm evt}$ is the number of events in the background data sample, $N_{\rm jet}$ is the number of jets in the event, $P_i(E_T)$ is the E_T-dependent probability for jet i to fake an electron, and $w_{\rm trig}$ is a factor to account for triggers (see below). Using this method, each jet in the event is considered. The E_T-dependent probability of the jet faking a tight or loose electron is the same as in the $WZ \to e\nu ee$ channel. The factor $w_{\rm trig}$ is the total integrated luminosity of the 93-95 and 95-96 data sets divided by the integrated luminosity of the 93-95 data set. This factor was necessary due to the lack of the EM1_EIS_TRKCC trigger in the 95-96 data set. Therefore, only the 93-95 data set was used to estimate the background and a simple scaling of the background in 95-96 data set was assumed.

The total number of background events expected from $e\mu + jet$ is $0.118 \pm 0.018(\text{stat}) \pm 0.035(\text{syst})$. The systematic error is due to the 30% error on the probability that a jet fakes an electron as mentioned previously.

The total number of background events from both sources of background is $0.118 \pm 0.018(\text{stat}) \pm 0.035(\text{syst})$.

Chapter 8

Results

8.1 Upper Limit on the WZ Cross Section

To set an upper limit on the cross section a Bayesian approach is used, including convolution of the Poisson probability of observing a given number of events with Gaussian probabilities for the expected signal and backgrounds. The method is described in Reference [87], and briefly outlined below.

The expected number of events μ is given by

$$\mu = \beta + \sigma \sum_i \epsilon_i \mathcal{L}_i Br_i \tag{8.1}$$

where

β	=	expected number of background events in all channels
σ	=	cross section
ϵ_i	=	efficiency for channel i (i=1,2 for $e\nu ee$, $\mu\nu ee$)
$\mathcal{L}$	=	integrated luminosity for channel i
Br_i	=	branching ratio for channel i

The factors multiplying the cross section are combined into one parameter α

$$\alpha = \sum_i \epsilon_i L_i B r_i \tag{8.2}$$

so the expected number of events is given by

$$\mu = \beta + \alpha\sigma \tag{8.3}$$

When calculating the error on α (σ_α) only the error on the integrated luminosity is assumed to be correlated between channels. This is the most conservative approach because other correlated errors exist between channels, including particle identification efficiency errors and trigger efficiency errors as will be discussed in the next section.

The normalized probability that the "true" number of events is μ, given the observed number of events N is

$$P(\mu|N) = \frac{\frac{\mu^N e^{-\mu}}{N!}}{\sum_{k=0}^{N} \frac{\beta^k e^{-\beta}}{k!}} \tag{8.4}$$

where the physical region is given by $\sigma > 0$, so that the normalization integral includes only the region $\mu > \beta$.

The uncertainties in α and β are assumed to be uncorrelated, so that the joint probability is the product of the individual probabilities. The probability distribution for α is assumed to be described by a Gaussian distribution about its

nominal value α_0

$$P(\alpha) = \frac{e^{-\frac{(\alpha-\alpha_0)}{2\sigma_\alpha^2}}}{\int_0^\infty e^{-\frac{(\alpha-\alpha_0)}{2\sigma_\alpha^2}} d\alpha} \tag{8.5}$$

A similar probability distribution is assumed for β.

After integrating over α and β we obtain the probability distribution for σ

$$P(\sigma) = \int_0^\infty d\alpha \int_0^\infty d\beta \int_\beta^\infty P(\mu|N)P(\alpha)P(\beta)\delta\left(\sigma - \frac{(\mu-\beta)}{\alpha}\right) d\mu \tag{8.6}$$

where $P(\alpha)$ and $P(\beta)$ are the probability densities for α and β.

Since each probability density is normalized separately, $P(\sigma)$ is also normalized to unity. A confidence limit is obtained by finding the cross section where the probability of the cross section being smaller is given by the confidence level CL

$$\int_0^{\sigma_{CL}} P(\sigma)d\sigma = CL \tag{8.7}$$

Using this method, the 95% confidence level limit on the cross section $\sigma(p\bar{p} \rightarrow WZ + X)$ was calculated to be 82.8 pb for the $e\nu ee$ channel. The 95% confidence level limit on the WZ production cross section from the $\mu\nu ee$ channel was found to be 82.9 pb. Combining the $e\nu ee$ channel and the $\mu\nu ee$ channel, a combined 95% confidence level limit of 48.3 pb was obtained. The background, efficiency, branching ratio and integrated luminosity values used to set these limits are summarized in Table 8.1. These limits are to be compared with a Standard Model cross section for WZ production of 2.6 pb.

	$e\nu ee$	$\mu\nu ee$
$\mathcal{L}$	92.3 ± 5.0 pb^{-1}	
ϵ	0.169 ± 0.014	0.115 ± 0.014
Br	0.0035	
N_{obs}	1	0
N_{bkg}	0.38 ± 0.14	0.12 ± 0.04
N_{SM}	0.146 ± 0.012	0.099 ± 0.009

Table 8.1: Numbers used in calculating upper limit on WZ production cross section. $\mathcal{L}$ is the integrated luminosity, ϵ is the overall detection efficiency, Br is the branching ratio, N_{obs} is the number of events observed, N_{bkg} is the number of background events, and N_{SM} is the predicted number of Standard Model events.

8.2 Coupling Parameter Limits

Because of the small number of observed events Poisson statistics are used in setting limits on the anomalous couplings. The method is essentially equivalent to that used in setting the cross section limit.

The Poisson probability of observing N events for a given mean value μ is

$$\frac{e^{-\mu}\mu^N}{N!} \tag{8.8}$$

The predicted mean number of events is given by

$$\mu = \mu_s + \mu_b. \tag{8.9}$$

$\mu_s = \mathcal{L}\ \epsilon\ \sigma$ is the expected number of signal events found by multiplying together the integrated luminosity $\mathcal{L}$, the detection efficiency ϵ and the cross section σ. The expected number of background events is μ_b. However, μ_s and μ_b are not known precisely. Construction of the appropriate probability is facilitated by the introduction

of a set of normalization parameters $\{x_i\}$. The probability density describing each of the $\{x_i\}$ is assumed to be described by a normalized Gaussian $g_i(x_i, \sigma_i)$ centered at unity:

$$g_i(x_i, \sigma_i) = \frac{e^{-\frac{(x_i-1)^2}{2\sigma_i^2}}}{\int_0^\infty e^{-\frac{(x_i-1)^2}{2\sigma_i^2}} dx_i} \tag{8.10}$$

where the unphysical region $x_i < 0$ has been excluded. The mean number of expected events is

$$\mu_x = x_s \; \mathcal{L}\epsilon\sigma + x_b \; \mu_b \tag{8.11}$$

where x_s represents the signal prediction normalization and x_b is the common background normalization. (By construction, the central value of all $\{x_i\}$ is one.) Thus, the probability for the ensemble of candidate events is given by

$$P = \int g_s \; g_b \; \frac{e^{-\mu_x} \mu_x^N}{N!} \; dx_s \; dx_b \tag{8.12}$$

where N is the number of candidates, and μ_x is given by equation 8.11.

When combining results from more than one channel, it is important to account for correlations in the uncertainties between the channels. For the case of the $e\nu ee$ and $\mu\nu ee$ channels, there are both common and channel-specific normalization uncertainties for both background and signal predictions. The mean number of $e\nu ee$ events becomes

$$\mu_{eee} = x_{s,c} \; x_{s,eee} \; \mathcal{L}\epsilon\sigma(WZ \to e\nu ee) + x_{b,c} \; x_{b,eee} \; \mu_{b,eee} \tag{8.13}$$

where $x_{s,c}$ represents the common signal prediction normalization, $x_{s,eee}$ is the

channel-specific signal prediction normalization, $x_{b,c}$ is the common background normalization, and $x_{b,eee}$ is the channel-specific background normalization. The mean number of $\mu\nu ee$ events becomes

$$\mu_{\mu ee} = x_{s,c}\ x_{s,\mu ee}\ \mathcal{L}\epsilon\sigma(WZ \to \mu\nu ee) + x_{b,c}\ x_{b,\mu ee}\ \mu_{b,\mu ee} \tag{8.14}$$

where the notation is similar to that used in Equation 8.13. The probability function for both channels becomes

$$\begin{aligned} P \;=\; & \int g_{s,c}\ g_{b,c}\ g_{s,eee}\ g_{b,eee}\ g_{s,\mu ee}\ g_{b,\mu ee} \\ & \times \left(\frac{e^{-\mu_{eee}}\mu_{eee}^{N}}{N!}\right)\ \left(\frac{e^{-\mu_{\mu ee}}\mu_{\mu ee}^{M}}{M!}\right) \\ & \times dx_{s,c}\ dx_{b,c}\ dx_{s,eee}\ dx_{b,eee}\ dx_{s,\mu ee}\ dx_{b,\mu ee} \end{aligned} \tag{8.15}$$

where N is the number of observed $e\nu ee$ events, M is the number of observed $\mu\nu ee$ events and μ_{eee} and $\mu_{\mu ee}$ are given by Equations 8.13 and 8.14 respectively.

The sources of common predicted signal normalization uncertainty are the di-electron selection efficiency error (0.98%), luminosity error (5.4%), theoretical cross section error (6.2%) and trigger efficiency error (2%). Added in quadrature they give $\sigma_{c,s} = 8.5\%$. The individual signal uncertainties come from identifying the third lepton, 4.4% for the muon and 0.7% for the electron.

Both the $e\nu ee$ and $\mu\nu ee$ background estimates are based on the jet misidentification probabilities for electrons, which has a 30% normalization uncertainty.

Therefore $\sigma_{c,b} = 0.30$. The individual background uncertainties come from the statistical error on the background. This uncertainty was 18% for the $e\nu ee$ channel and 15% for the $\mu\nu ee$ channel.

uncertainty	value
$\sigma_{s,c}$	0.085
$\sigma_{b,c}$	0.30
$\sigma_{s,eee}$	0.007
$\sigma_{b,eee}$	0.18
$\sigma_{s,\mu ee}$	0.044
$\sigma_{b,\mu ee}$	0.15

Table 8.2: Summary of uncertainties for combined probability function.

Equations 8.10–8.15 provide a means of calculating the probability of observing N events for given values of the WWZ coupling parameters. In order to sufficiently determine the probability in Equation 8.15, knowledge of μ_s is required for many values of Δg_1^Z and λ_Z. The computational burden is reduced by constructing a 3×3 grid of μ_s values which are obtained from the fast detector simulation for $\Delta g_1^Z = \{0, \pm x_0\}$ and $\lambda_Z = \{0, \pm y_0\}$, where x_0 and y_0 are chosen to be outside the limits being set. Biquadratic interpolation [66] is then used to evaluate μ_s for given values of Δg_1^Z and λ_Z. The accuracy of this technique was verified by comparing interpolated values with those obtained directly from the simulation at various points in the Δg_1^Z-λ_Z plane.

Once the probability at each point in the $(\Delta g_1^Z, \lambda_Z)$–plane is known limits can be set. The limits are found by taking the log of the probability ($L = -\ln P$) and finding the contour where

$$L = L_{max} - \delta.$$

To set a 95% confidence level (CL) limit in one dimension, the contour is evaluated at $\delta = 1.92$. To set a 95% CL limit in two dimensions, the contour is evaluated at $\delta = 3.00$.

The value of the form factor scale Λ_{FF} is chosen such that the coupling limit is less than the unitarity limit. The 1-dimensional 95% CL coupling limits and unitarity limits as a function of Λ_{FF} for each of the three coupling parameters are shown in Figure 8.1. The unitarity limits are given by Equations 1.7–1.9 in Section 1.4.2.

As noted is Section 1.4.2 this analysis is most sensitive to the parameters λ_Z and Δg_1^Z. Setting $\Lambda_{FF} = 1$ TeV, the 1-dimensional 95 % CL limits from the $e\nu ee$ channel are

$$|\Delta g_1^Z| < 2.40 \text{ for } \lambda_Z = 0 \ ; \ |\lambda_Z| < 1.98 \text{ for } \Delta g_1^Z = 0.$$

The limits from the $\mu\nu ee$ channel are

$$|\Delta g_1^Z| < 2.51 \text{ for } \lambda_Z = 0 \ ; \ |\lambda_Z| < 2.07 \text{ for } \Delta g_1^Z = 0.$$

The limits using both channels are

$$|\Delta g_1^Z| < 1.63 \text{ for } \lambda_Z = 0 \ ; | \ \lambda_Z| < 1.42 \text{ for } \Delta g_1^Z = 0.$$

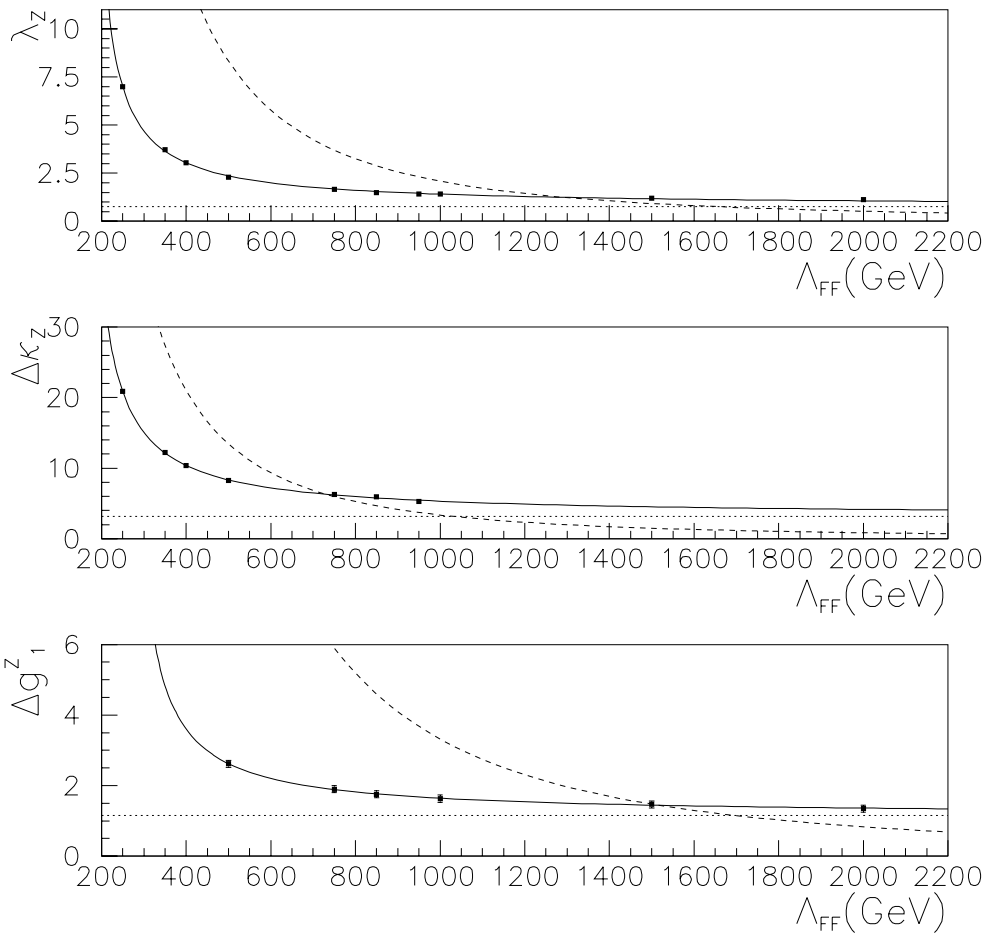

Figure 8.1: 1-dimensional 95% CL (solid) and unitarity limits (dashed) vs. Λ_{FF} for the WWZ coupling parameters λ_Z, $\Delta\kappa_Z$ and Δg_1^Z.

The 2-dimensional 95% CL contour limits for $\Lambda_{FF} = 1$ TeV are shown in Figure 8.2 for the $e\nu ee$ and $\mu\nu ee$ data combined. The unitarity limit contour is given by running a program provided by the authors of [9] which gives a set of

points outside of which unitarity is violated.

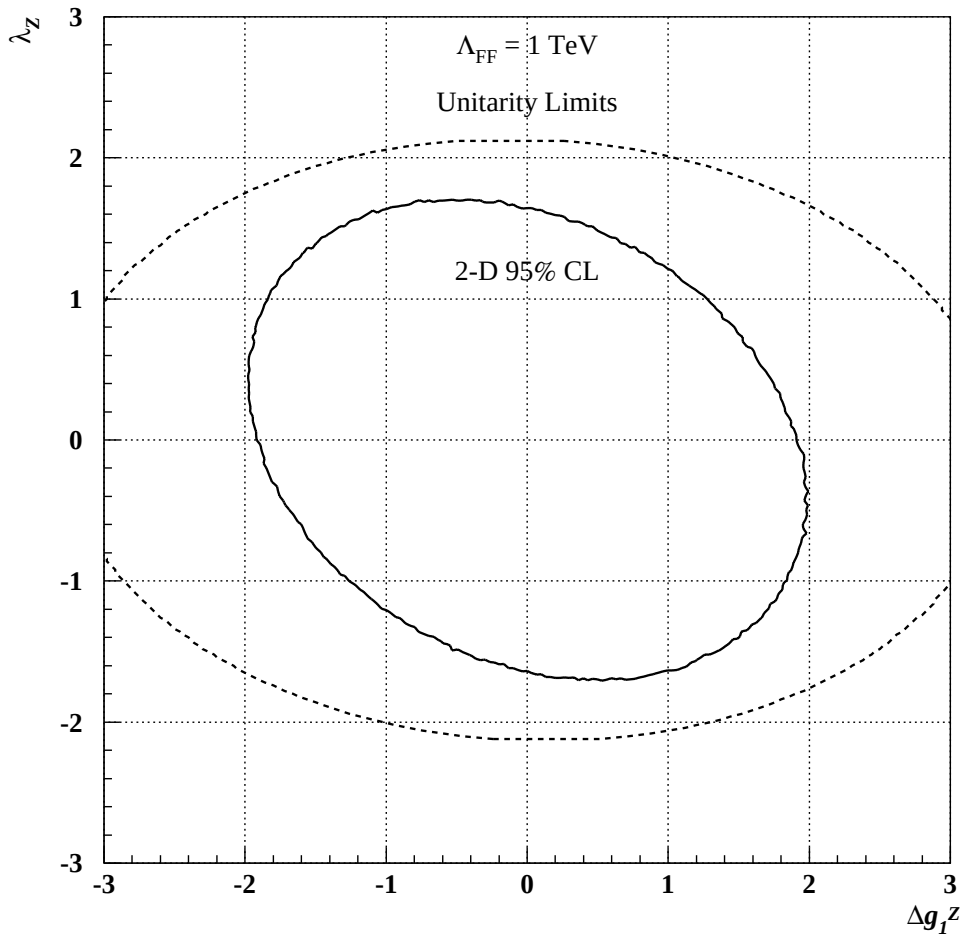

Figure 8.2: Correlated limits on Δg_1^Z and λ_Z for $\Lambda_{FF} = 1$ TeV obtained from a fit to the cross section using the 93-96 data for the $\mu\nu ee$ and $e\nu ee$ channel combined. The solid line is the 2-dimensional 95% CL limits and the dashed line is the unitarity limit.

Chapter 9

Conclusions

9.1 Summary

A search for WZ production in the $e\nu ee$ and $\mu\nu ee$ channel was performed using 92.3 ± 5.0 pb^{-1} of data recorded by the DØ detector in $p\bar{p}$ collisions at $\sqrt{s}$ = 1.8 TeV during the 1993-1996 data taking runs. One event is observed with an expected Standard Model signal of $0.245 \pm 0.002\,(\text{stat}) \pm 0.015\,(\text{syst})$ events and an expected background of $0.498 \pm 0.072\,(\text{stat}) \pm 0.125\,(\text{syst})$ events. This does not represent a significant excess of WZ events. The 95% upper confidence limit on the WZ production cross section is found to be 48.3 pb. A fit to the expected number of events as function of the coupling parameters is performed and limits are set. Assuming only one parameter varies at a time the 95% CL limits are $|\Delta g_1^Z| < 1.63$ and $|\lambda_Z| < 1.42$ for a form factor scale of $\Lambda_{FF} = 1$ TeV. Although the limits are

looser than those previously measured, they are independent of the $WW\gamma$ vertex coupling. Previous results have relied on making assumptions about the relation between the $WW\gamma$ and WWZ couplings.

9.2 Future Prospects

With an expected 2 fb^{-1} of data to be delivered in the next Tevatron collider run and an upgraded DØ detector, it will be possible to observe a significant WZ production signal in the $l\nu ll$ final state. This will enable the direct measurement of the cross section instead of placing upper limits and will result in tighter limits on the WWZ coupling parameters.

Bibliography

[1] S. Abachi, *et al.* (DØ Collaboration), "Observation of the Top Quark", *Phys. Rev. Lett.* **74**, 2632 (1995).

[2] F. Abe, *et al.* (CDF Collaboration), "Observation of the Top Quark in $p\bar{p}$ Collisions", *Phys. Rev. Lett.* **74**, 2626 (1995).

[3] S. Weinberg, *Phys. Rev. Lett.* **19**, 1264 (1967).

[4] A. Salam in *Elementary Particle Theory*, ed. N. Svarthom, et al. Stockholm (1968);

M.E. Peskin , D.V. Schroeder *An Introduction to Quantum Field Theory.* Addison-Wesley (1995);

S. Weinberg *The Quantum Theory of Fields.* Cambrisge, UK: Cambridge Univ. Press (1995).

[5] F. Halzen and A. Martin, *Quarks and Leptons*, John Wiley & Sons, Inc. (1994).

[6] UA1 Collaboration, "Experimental Observation of Isolated Large Transverse Energy Electrons with Associated Missing Energy at $\sqrt{s} = 540$ GeV." *Phys. Lett.* **B122**, 103 (1983);

UA2 Collaboration, "Observation of Single Isolated Electron with High Transverse Momentum in Events with Missing Transverse Energy at the CERN $p\bar{p}$ Collider." *Phys. Lett.* **B122**, 476 (1983).

[7] UA1 Collaboration, "Experimental Observation of Lepton Pairs of Invariant Mass around 95 GeV/c^2." *Phys. Lett.* **B126**, 398 (1983);

UA2 Collaboration, "Evidence for $Z^0 \to e^+e^-$ at the CERN $p\bar{p}$ Collider." *Phys. Lett.* **B129**, 130 (1983).

[8] T. Sjostrand, "PYTHIA 5.7 and JETSET 7.4: Physics and Manual" *Comput. Phys. Commun* **82**, 74, (1994).

[9] K. Hagiwara, J. Woodside, and D. Zeppenfeld, *Phys. Rev.* **D41**, 2113 (1990).

[10] A. Martin, W. Stirling, and R. Roberts, "New Information on Parton Distributionns." *Phys. Rev.* **D47**, 867 (1993);

"Parton Distributions Updated." *Phys. Lett.* **B306**, 145 (1993).

[11] V. Barger and R. Philips, *Collider Physics.* Frontiers In Physics Lecture Note Series, Addison-Wesley (1987).

[12] J. Papavassiliou, K. Philippides, *Phys.Rev.* **D48**, 4255 (1993).

[13] J. Koidaira, *et al.* in *INS Workshop Phys.* e^+e^-, $e^-\gamma$ *and* $\gamma\gamma$ *Collis. at Linear Accel.*. Tokyo, Japan, Dec. 20–22, 1994, ed. Z. Hioki, T. Ishii, R. Najima. Tokyo Univ., Inst. Nucl. Study (1995).

[14] D. Chang , W.-Y. Keung, *Nucl. Phys.* **B355**, 295 (1991).

[15] I.B. Khriplovich , M.E. Pospelov, *Nucl. Phys.* **B420**, 505 (1994).

[16] G. Couture, *et al.*, *Phys. Rev.* **D36**, 859 (1987).

[17] X.-G. He, B.H.J. McKellar, *Phys. Rev.* **D42**, 3221 (1990);
Phys. Rev. **D50** 4719 (1994).

[18] G. Couture, J.N. Ng, *Z. Phys* **C35**, 65 (1987).

[19] E.N. Argyres, *et al.*, *Phys. Rev.* **B383**, 63 (1996).

[20] T. Kadoyoshi, N. Oshimo, *Phys. Rev.* **D55**, 1481 (1997).

[21] T. Appelquist, G.-H. Wu, *Phys. Rev.* **D48**, 3235 (1993);
Phys. Rev. **D51**, 240.

[22] C.P. Burgess, A. Pilaftsis, *Phys. Rev.* **B333**, 427.

[23] J. Ellison and J. Wudka, *"Study of Trilinear Gauge Boson Couplings at the Tevatron Collider"*, to be published in *Ann. Rev. Nucl. Part. Sci.*, UCR/DØ/9801, hep-ph/9804322 (1998).

[24] K. Hagiwara, R.D. Peccei, D. Zeppenfeld amd K. Hikasa, *Nucl. Phys.* **B282**, 253 (1987).

[25] K. Hagiwara, S. Ishihara, R. Szalapski and D. Zeppenfeld, *Phys. Rev.* **D48**, 2182 (1993); *Phys. Lett.* **B283**, 353 (1993).

[26] U. Baur and D. Zeppenfeld, *Phys. Lett.* **B201**, 383 (1988).

[27] H. Aihara *et al.*, Preprint Fermilab-Pub-95/031 (1995).

[28] J. Alitti *et al.* (UA2 Collaboration), *Phys. Lett.* **B277**, 195 (1992).

[29] F. Abe *et al.* (CDF Collaboration), *Phys. Rev. Lett.* **74**, 1936 (1995); *Phys. Rev. Lett.* **75**, 1017 (1995).

[30] S. Abachi *et al.* (DØ Collaboration), *Phys. Rev. Lett.* **78**, 3634 (1997).

[31] F. Abe *et al.* (CDF Collaboration), *Phys. Rev. Lett.* **74**, 1936 (1995).

[32] B. Abbot *et al.* (DØ Collaboration), *Phys. Rev. Lett.* **79**, 1441 (1997).

[33] F. Abe *et al.* (CDF Collaboration), *Phys. Rev. Lett.* **78**, 4537 (1997).

[34] B. Abbot *et al.* (DØ Collaboration), to be published in *Phys. Rev.* **D**, Rapid Communications (1998), FERMILAB PUB 98-076-E, hep-ex/9803004

[35] J. Ellison, "Measurement of the W Boson Mass and Trilinear Gauge Boson Couplings at the Tevatron" to be published in *Proceedings of the XXXIIId*

Rencontres de Moriond, Electroweak Interactions and Unified Theories, Les Arcs, Savoie, France, March 14-21 1998.

[36] J-M. Jousset, "A combination of Preliminary Measurements of Triple Gauge Boson Coupling Parameters by the LEP and DØ Experiments" to be published in *Proceedings of the XXXIIId Rencontres de Moriond, Electroweak Interactions and Unified Theories, Les Arcs, Savoie, France, March 14-21 1998.*

[37] L. M. Lederman, Scientific American **264**(3) 48 (Mar. 1991);
H. T. Edwards, Ann. Rev. Nucl. Part. Sci. **35**, 605 (1985;).
F. T. Cole *et al.*, "Design Report Tevatron 1 Project," FNAL Internal Note (1984;), unpublished.
F. T. Cole *et al.*, "A Report of the Design of the Fermi National Laboratory Superconducting Accelerator," FNAL Internal Note (1979.), unpublished.

[38] W. J. Thompson, "Introduction to Colliding Beams at Fermilab," DØ Internal Note 2367 (1994), unpublished.

[39] D. Möhl *et al.*, Phys. Rep. **C58**, 73 (1980).

[40] S. Abachi *et al.*, Nucl. Instr. Meth. **A338**, 185 (1994).

[41] S. Snyder, "The DØ Detector," DØ Internal Note 2500 (1995), unpublished.

[42] F. Sauli, `Principles of Operation of Multiwire Proportional and Drift Chambers` in T. Ferbel, editor, *Experimental Techniques in High Energy Physics*. Addison-Wesley (1987).

[43] R. C. Fernow, *Introduction to Experimental Particle Physics*. Cambridge University Press (1986).

[44] K. Kleinknecht, *Detectors for Particle Radiation*. Cambridge University Press (1987).

[45] A. R. Clark *et al.*, Nucl. Instr. Meth. **A261**, 420 (1987).

[46] A. R. Clark *et al.*, Nucl. Instr. Meth. **A279**, 243 (1989).

[47] A. R. Clark *et al.*, Nucl. Instr. Meth. **A315**, 193 (1992).

[48] J. F. Detœuf *et al.*, Nucl. Instr. Meth. **A265**, 157 (1988).

[49] J. F. Detœuf *et al.*, Nucl. Instr. Meth. **A279**, 310 (1989).

[50] D. Buchholz *et al.*, Nucl. Instr. Meth. **A257**, 556 (1987).

[51] T. Behnke, *The Central Drift Chamber for the DØ Detector: Design, Construction, and Test*. Ph.D. thesis, State University of New York at Stony Broook, Stony Brook, New York, 1989 (unpublished).

[52] D. Pizzuto, *DØ Central Tracking Performance Studies.* Ph.D. thesis, State University of New York at Stony Broook, Stony Brook, New York, 1991 (unpublished).

[53] S. Rajagopalan, *The dE/dx Capabilities of the DØ Tracking System.* Ph.D. thesis, Northwestern University, Evanston, Illinois, 1992 (unpublished).

[54] J. W. Bantly, *The DØ Forward Drift Chamber Performance and Physics Capability in the 1990 FNAL Testbeam Run.* Ph.D. thesis, Northwestern University, Evanston, Illinois, 1992 (unpublished).

[55] C. Fabjan, `Calorimetry in High-Energy Physics` in T. Ferbel, editor, *Experimental Techniques in High Energy Physics.* Addison-Wesley (1987).

[56] U. Amaldi, `Fluctuations in Calorimetry Measurements` in T. Ferbel, editor, *Experimental Techniques in High Energy Physics.* Addison-Wesley (1987).

[57] C. Brown, *et al.*, Nucl. Instr. Meth. **A279**, (1989).

[58] J. Bantly, *et al.*, "Improvement to the DØ Luminosity Constant." DØ Internal Note 2544 (1995.), unpublished.

[59] J. Butler, "Main Ring Deadtime," DØ Internal Note 1682 (1993), unpublished.

[60] M. Abolins, *et al.*, "The Fast Trigger for the DØ Experiment." *Nuclear Instruments and Methods* **A289**, 543, (1990).

[61] J. Bantly, *et al.*, "The DØ Level 1.5 Calorimeter Trigger." DØ Internal Note 2147 (1994), unpublished.

[62] Fatyga, M. "Tuning Electron Id Parameters for the Level 2 Trigger Using Test-beam Data." DØ Internal Note 1768 (1994), unpublished.

[63] G. Manning, "DØ Software Documentation." DØ Internal Document July 10,1995.
(URL: `http://www-d0.fnal.gov/software/offline_document.ps`)

[64] N. Graf, DØ Internal Note (in preparation).

[65] T. Yasuda, "A Study of CDC z Measurement Using Collider Muon Tracks," DØ Internal Note 2782 (1995), unpublished.

[66] S. Glenn, *A Search for Self Interactions of Neutral Electroweak Gauge Bosons.* Ph.D. thesis, University of California at Davis, Davis, California, 1996 (unpublished).

[67] S. Youssef, "A Family of Cluster Algorithms," DØ Internal Note 375 (1986), unpublished.

[68] S. Youssef, "Clustering with Local Equivalence Relations," DØ Internal Note 541 (1987), unpublished.

[69] N. Graf, "Simulation of the Level 1 CC Edge Effect," DØ Internal Note 1339 (1992), unpublished.

[70] N. Graf, "Improvements to the Calorimeter Electron Position Algorithm," DØ Internal Note 1352 (1992), unpublished.

[71] A. Goldschmidt and S. Glenn, "Corrections to Biases in Cluster-Track Matching," DØ Internal Note 2419 (1995), unpublished.

[72] R. Raja *et al.*, "Reconstruction and Analysis: Trcaking Packages, Calorimeter Packages," DØ Internal Note 1006 (1990), unpublished.

[73] R. Raja, "H-matrix Analysis for top $\rightarrow$ lepton + jets," DØ Internal Note 1192 (1992), unpublished.

[74] M. Narain, `Electron Identification in the DØ Detector`, in *Proceedings of the American Physical Society Division of Particles and Fields Conference*, Fermilab, Batavia, Illinois (1992).

[75] R. Kehoe, *Search for the Top Quark in Dielectron Final States at sqrts = 1.8 TeV and Measurement of the Response of the DØ U/LAr Calorimeter to Jets.* Ph.D. thesis, University of Notre Dame, Notre Dame, Indiana, 1997 (Unpublished).

[76] S. Glenn, *A Search for Self Interactions of Neutral Electroweak Gauge Bosons.* Ph.D. thesis, University of California at Davis, Davis, California, 1996 (Unpublished).

[77] T. Yasuda, *et al.*, "Muon Chamber Alignment" DØ Internal Note 2279 (1994.), unpublished.

[78] D. Casey, T. Joffe-Minor and J. Tarazi, "QCD/WZ Ntuple", DØ Internal Note 3124 (191996), unpublished.

[79] F. Carminati,et. al., *GEANT Users Guide*, CERN Library Program Entry W5013 (1993).

[80] D. Norman, "Improved Low E_T Electron Identification using Lower Dimensional H-Matrices and Fisher Variables." DØ Internal Note 2453 (1995), unpublished.

[81] P. Bloom. *Investigation of the Trilinear Vector Boson Couplings Through W Boson Pair Production in the Dilepton Decay Channels* Ph.D. thesis, University of California at Davis, Davis, California, 1998 (Unpublished).

[82] B. Abbot *et. al.* (DØ Collaboration), to be published in *Phys. Rev.* **D**, Rapid Communications (1998), FERMILAB PUB 98-076-E, hep-ex/9803004

[83] S. Glenn, "A Parametric Detector Simulation for Dibosons." DØ Internal Note 2846 (1996), unpublished.

[84] D. Wood, *et. al.* , DØ Internal Note 2140 (19.), unpublished.

[85] S. Glenn. "A Study of Electron and Photon Fakes", DØ Internal Note 2937 (1996), unpublished.

[86] O. Helene, Nucl. Instr. and Methods **212** (1983) 319; Nucl. Instr. and Methods **228** (1984) 120.

[87] R. Partridge, DØ Internal Note 1806 (1993.), unpublished.

Appendix A

Candidate Event Properties

The properties of the $e\nu ee$ candidate event are listed below. Table A.1 lists the properties of the electron candidates. Table A.2 lists the kinematic properties of the event.

	e_1	e_2	e_3
E_T (GeV)	54.5	50.9	37.7
η	0.11	-0.62	1.37
η_{det}	0.38	-0.38	1.51
ϕ	5.94	3.04	4.14
E_{EM}/E	1.000	0.997	0.990
χ^2	12.6	23.4	62.4
I	0.017	0.021	0.043
S_{track}	0.2	NA	1.2
z_v (cm)	25.6	NA	25.2
NH_{xy}	31	27	117

Table A.1: Properties of electrons in $e\nu ee$ candidate event (Run 89912, Event 23020). η_{det} is the η measured with respect to $z = 0$, E_{EM}/E is the electromagnetic fraction, χ^2 is the shower shape covariance parameter, I is the cluster isolation, S_{track} is the track match significance, z_v is the vertex z position found using cluster-track projection, and NH_{xy} is the number of hits on the drift chamber wire.

Kinematic Infomation	
$M_{e_1,e_2} = 111.8$ GeV	$M_{e_1,e_2,e_3} = 171.7$ GeV
$M_{e_1,e_3} = 93.6$ GeV	$M_{e_2,e_3} = 112.4$ GeV
$\not\!\!E_T = 46.2$ GeV	$\phi(\not\!\!E_T) = 1.29$
$M_T(e_i, \not\!\!E_T) = 73.0, 74.7, 82.6$ GeV	for e_1, e_2, e_3 respectively
$p_T(1,3) = 58.8$ GeV	$\phi(1,3) = -1.02$
$p_T(2, \not\!\!E_T) = 63.0$ GeV	$\phi(2, \not\!\!E_T) = 2.22$
Vertex Information	
Electron Vertex: z = 25.5 cm	
DØRECO Vertices: z = -23.0 cm, 25.0 cm	

Table A.2: Kinematic and vertex information for $e\nu ee$ candidate event. M_{e_i,e_j} is the invariant mass of electron i and electron j. M_{e_1,e_2,e_3} is the three body mass of electron 1, electron 2 and electron 3. M_T is the transverse mass and p_T is the transverse momentum.